Computational Study on Small Pt Clusters: Structure of Pt_n^- Clusters and Elementary Steps in Nanocatalysis

zur Erlangung des akademischen Grades eines

DOKTORS DER NATURWISSENSCHAFTEN

(Dr. rer. nat.)

von der KIT-Fakultät für Chemie und Biowissenschaften

des Karlsruher Instituts für Technologie (KIT)

genehmigte

DISSERTATION

von

Asfaw Geremew Yohannes, M.Sc.

aus

Gondar, Ethiopia

1. Referent: PD. Dr. Karin Fink

2. Referent: Prof. Dr. Willem Klopper

Tag der Mündlichen Prüfung: 06. Dezember 2019

Contents

Chapter 1

Introduction

Catalysis significantly impacts our society being an integral part of the fundamental aspects required for life, namely energy, food and water. About 85% of the products of chemical industries are made with the help of catalytic processes. Approximately 35% of the world's gross domestic product is influenced by catalysis [1]. Heterogeneous catalysts are crucially important in chemical industries. To mention just two among the prominent catalytic processes: zeolites are used as catalysts for crude oil cracking to produce fossil fuel energies, which accounts for 80% of global primary energy consumption, [2] and iron based catalysts enable to produce ammonia at industrial quantities by extracting nitrogen from the air, the so-called Haber–Bosch process [3]. Therefore, a knowledge-driven design of catalysts for specific reactions is of great interest. This requires understanding on all time and length scales and this is still a great challenge. Detailed understanding of the mechanisms of some catalytic processes has been achieved, for example, in the case of the Haber–Bosch process [4]. For many processes, the exact structure–functionality relation with in-depth atomic level details is still not fully understood.

Transition metals, such as Pt and Pd are widely known for their catalytic properties. One of the major applications of Pt and Pd catalysts is in automotive catalytic converters in which oxidation of carbon monoxide (CO) to carbon dioxide (CO_2) is carried out [2]. The CO oxidation reaction can be catalyzed by single metal atoms [5, 6], by small metal nanoclusters [7, 8] and by single-crystal surfaces [9]. The structure–reactivity relationship for metal catalysts has been conventionally and qualitatively interpreted in terms of electronic and geometric properties, which are caused by the size effect, morphology, chemical composition, and a high surface-to-volume ratio [10]. The metal nanoclusters are intermediates between the molecular-like and solid state of matter. The nanostructured catalysts are featured by the highly reduced size (only a few nanometers) and hence, high surface-to-volume ratio, which makes them more efficient than single crystal surfaces due to the larger number of active sites allowing a significant reduction of catalyst loading. The size of nanoclusters can range from a few atoms to hundreds of atoms. In this thesis, the terms sub-nanocluster and nanoparticle will be used to refer to small nanoclusters (atom numbers < 20) and large clusters (atom numbers > 20), respectively.

In the case of reactions on sub-nanoclusters, one needs to probe each size of cluster con-

figuration individually to understand the structure-activity relationship [11, 12]. However, to study sub-nanocluster properties, one needs to have a thermodynamic stable geometrical configuration of a cluster and the exact geometry of a specific size of transition metal clusters is usually unknown. There is no direct experimental method to observe atomic arrangements of a nanocluster and, on the other hand, the results of electronic structure calculations are strongly method dependent. In alternative, combining trapped ion electron diffraction (TIED) measurement techniques with theoretical global optimization methods to determine the most stable structure is applied [13]. The further approach for structural determination is comparison of calculated and measured IR spectra [14]. In this context, part one of this thesis deals with structural determination of small platinum clusters using a combination of a density functional theory (DFT) based global optimization technique and TIED measurements performed by Dennis Bumüller in the group of Detlef Schooss. The surface of medium size clusters comprises small fractions of crystal planes with high coordinated adsorption sites, such as (111) and (100) terraces, and low coordinated sites, such as edges, corners and defects [15]. This structural complexity leads to enhanced reactivity [16].

In theoretical studies of catalysis, the activity of a catalyst is often predicted from simple descriptors using scaling relationships, for example adsorption energies. Scaling relations can be powerful to reduce the calculation of the complex elementary reactions steps to describe the catalytic performance. For example, in methane steam reforming the adsorption energies of C and O are used in a scaling relation to determine the adsorption energies of other intermediates, giving the reaction energies of all of the elementary steps [17]. Then using the Brønsted-Evans-Polanyi (BEP) [16, 18] relation, it is possible to determine the transition state energies from the reaction energies to estimate the activity of a reaction. If the activation energies and adsorption energies are known, the performance of a catalyst can be determined by applying a microkinetic model. Similarly, Montemore et al. [19] have used the adsorption energies of C and O as descriptor for scaling relations in the reactions of methane to predict the adsorption energies of the other intermediates (OH, CHx, CO and H). Thus, electronic structure calculation of adsorption energies on different active model catalysts with variety of surface geometries and adsorption sites can be very important for atomic level understanding of surface properties.

Part two of this thesis comprises a study of adsorption properties of CO and oxygen on Pd and Pt nanoparticles with the prime objective of understanding the interaction of adsorbates with the catalyst surface that can provide atomic-level insight into the CO oxidation or other reactions that includes O and/or CO intermediates. The atomic scale understanding may ultimately help to control the reaction and to design better catalysts. Having a large database of adsorption energies with the corresponding structural data can be very useful to accelerate the development of new catalysts. Such database can contribute to big data driven material science that provides novel, extraordinary and wide-range opportunities for achieving unprecedented scientific understanding and insight. These opportunities require new research concepts and ways of understanding and interpretation of the data [20]. Data-driven material science can be explored using a set of powerful tools from data mining, machine learning, and mathemat-

ical optimization to systematically reveal materials processing-structure-property-performance (PSPP) relations. These PSPP relations can facilitate the predictive discovery and design of novel materials and optimized manufacturing processes [21]. Therefore, storing and sharing simulation data in repositories can have great importance in progressing data-driven material exploration. The data generated in this work has been stored in a repository created at HPC computers of Steinbuch Centre for Computing (SCC) with the aim that it can be used for future purposes.

This thesis is structured as follows: In chapter 2, a short introduction to small Pt clusters and the related literature is given. Chapter 3 presents background about the methods applied for the structure determination of small anionic Pt clusters. This includes description about the global optimization method and the used experimental information. The details of used DFT computation are also given in this chapter. In chapter 4, some benchmark calculations are presented. Chapter 5 includes the results and discussion for the calculations on Pt_6^- to Pt_{13}^-. In Chapter 6, a short review of CO and O adsorption properties in the context of catalysis is given. Chapter 7 presents the description of the methods used for the calculation including technical details and the descriptors applied for analysis. Moreover, the Pt and Pd model catalysts used for the calculations are introduced. The database design descriptions are also included in this chapter. In chapter 8, the results are presented and described in detail, which includes adsorption and vibrational property calculations at various sizes, shapes and at different sites of the nanoparticles. The coverage effect on adsorption energy of oxygen are also analyzed. Finally, in chapter 9 the findings of the thesis are summarized.

Part I

Chapter 2

Introduction to small Pt clusters

Metal clusters are intermediates between molecules and the bulk solid state and they often show peculiar physico-chemical properties [22]. These size-dependent properties can be due to the large surface-to-volume ratio, quantum-size effects, geometrical structures and lower atomic coordination. Because of the large number of electrons, bulk systems form bands of energy, whereas in atoms/molecules the energy levels are discrete. The energy levels of clusters are between bulk continuum bands and discrete energy levels. When the size of the clusters increases, the bulk properties emerge gradually, which enables to tailor the material properties. Depending on the property and the material being investigated, the size at which the properties of clusters will approach the size of the bulk phase can be different. The information about the point where the transition towards the crystalline state starts to occur can be tuned by assessing the preferred packing as a function of cluster size. Transition metal clusters are very important in technological applications, for example, in catalysis, magnetic and optical devices [23].

For small transition metal clusters, the geometries and properties can change on addition of single atoms. The change in properties becomes less abrupt when the cluster size is getting large and this variation gradually approaches the bulk phase property. This size-property change of metallic clusters offers a special attraction to many materials studies. There has been considerable scientific research progress to study the properties of clusters for the aim of making catalytic devices, high density storage materials, optical devices and some other applications. For instance, Vajda et al. reported that the catalytic activity of Pt clusters (size 8 to 10) is 40-100 times more active than vanadia based catalysts for oxidative dehydrogenation of propane [24]. Small gold clusters are reactive in the combustion of CO and saturated hydrocarbons, while the bulk phase is inactive [25]. Rhodium metal is non-magnetic in the bulk state, but becomes magnetic for clusters [26]. While size is one essential consideration, the materials properties depend also on the geometry of thermodynamic stable structure. For example, depending on geometry of the isomers, a single cluster size can have different reaction rates [27, 28]. Furthermore, for small transition metal clusters, there are notable cases in which adding or removing one electron on a given cluster can influence the energetic and geometric properties [29–31]. For example, in the range up to 21 Pt atoms the reaction efficiency with methane was higher for positively charged clusters than for negatively charged ones and the

neutral ones perform in between [29]. Thus, the chemical reactivity of metallic clusters can be easily tuned by varying their size, geometry, charge, and chemical composition. Therefore, geometry/structure determination necessitates to gain detailed understanding on properties of clusters.

Platinum is one of the important catalysts for a wide variety of reactions. For example, in automobiles as a catalytic converter, in the oxygen reduction reaction (ORR) [32, 33], and in the hydrogen evolution reaction (HER) [34] platinum is very vital. Recently, small platinum clusters with less than 30 atoms gain significant attention because of their high activity towards various reactions [24, 35–38]. Despite, as there are numerous theoretical studies for neutral small platinum clusters, the results are often inconsistent with each other and have been inconclusive to assign the equilibrium structures [39–42]. For example, Kumar et al. [40] proposed planar structures up to Pt_9, while Demiroglu et al. [43] claim that 3D motifs start from Pt_7. However for charged Pt clusters, to my best knowledge only Chaves et al. [44] have studied and compared the different charge states for the thermodynamically lowest energy structures using DFT. In their work, they have found different structures for most sizes because of charge differences. However, cluster size 6 and 10 were exceptionally found to exist as the same structure regardless of the charge state. It was also reported the same geometry for the neutral and anion Pt_9. In the same study, the 2D–3D transitions are found to occurs at n = 3–4 for Pt_n^+, n = 6–7 for Pt_n^0 and n = 9–10 for Pt_n^-.

Ni and Pd metals that belong to the Pt group have been studied and showed different structural growth compared to Pt. The neutral Ni and Pd clusters occur as 3D structures already at size n = 4. Ni clusters have shown a growth pattern based on tetrahedral and octahedral motifs, forming perfect or capped triangular and square bipyramids, whereas more compact tetrahedral-like structures have been obtained for Pd [45]. For Pd small size (n ≤ 7) clusters, it has been reported that the neutral and corresponding charged palladium clusters have similar geometric configurations and follow the same structural evolution [46, 47]. Moreover, fcc-like growth behavior is found for medium size neutral and charged Pd_n (n = 16-20) clusters [46]. On the other hand, neutral Au is known to exhibit planar motifs up to size n = 11 or 13. For example, Chaves et al. [45] have reported that neutral Au is planar up to 13 atoms, while Johansson et al. [48] claims that the transition from 2D to 3D occurs between 11 and 12 atoms. For the anion and cation Au clusters, transition from 2D to 3D occurs at 12 and 8 atoms size, respectively. It is argued that the relativistic effects, i.e., the 6s contraction and the indirect destabilization of the 5d orbital is the reason for the preference of the planar structures for Au [45].

For small metallic clusters, it is nontrivial to assign the thermodynamic equilibrium ground state structures. It is typical for transition metals to get several isomer structures within the DFT error range (below 0.2 eV), which makes it hard to determine the true ground state isomer. One can see this problem when employing different density functionals in which the relative energy ordering of close energy isomers changes from one functional to the other. For example, Li et al. [49] have shown that the change of the DFT functional can change the order of the isomers while the ordering remains unchanged for small clusters up to 6 atoms when spin-

orbit coupling was considered. On the other hand, experimental measurements alone are not always sufficient in the case of structural determination of small metallic cluster. However, the combination of theory and experiment can assist the structural assignment. This synergistic approach has been applied in several studies and was successful for Au and Ru metal clusters [13, 31]. In the present work, the structures of the anionic platinum cluster in size range 6 to 13 have been studied by means of a DFT based genetic algorithm (GA-DFT) global search method and the structures were compared to the results of trapped ion electron diffraction measurements performed in the group of Detlef Schooss at the Institute of Nanotechnology of KIT to assign the structural motif.

Chapter 3

Theoretical and Experimental Details

3.1 Global Optimization

In chemistry global optimization methods are used to evaluate potential energies of numerous configurations at the potential energy surface. The equilibrium configuration that possesses the lowest possible energy on the potential energy surface (PES) is called global minimum (GM) structure. The GM structure ideally corresponds to a material/substance as it occurs in nature. The theoretical and experimental investigations of any property of interest, therefore, must start from the global minimum structure. Hence, locating the GM geometry is vital and a fundamental step to study further on properties and reactivity of a certain material. The aim is to be able to correlate rationally the geometrical arrangement of atoms with the desired properties and ultimately to guide the design of the material of interest. A structure consisting of N atoms requires a 3N-dimensional vector to describe the atomic positions and the PES of the structure is the potential energy of these N atoms as a function of their position. The PES has a complicated landscape due to the fact that the number of local minima grows exponentially with the number of atoms [50]. Hence, exploring the PES multi-dimensional space to find the global minimum structure is nontrivial and a very computational demanding task except for very small systems. Moreover, GM determination starting from the prior knowledge of bonding motifs of a similar system, i.e., a biased approach can lead to wrong predictions.

To locate the GM effectively without bias on the PES, various algorithms have been proposed and applied in numerous reported works [51–55]. One can broadly categorize these algorithms into thermodynamically motivated and nature (evolutionary) inspired ones. The thermodynamic principle based algorithms can be molecular dynamics [56] and Monte Carlo types [57] which include simulated annealing, basin hopping, and multi-canonical methods. Despite their frequent usage, these methods are always accompanied by undesired infinitely long trajectory and no guarantee that the GM is reached, especially if the starting structure is unfavorable [58].

The other crucial factor that influences the efficiency of global optimizations is the method employed to calculate the energy and force of the sampled structures in the PES landscape. Since global optimization usually searches several configurations at the PES, the calculation of

energies of all possible isomers can be too expensive. Basically, the energy and force evaluation step dominates the overall computational demand in global optimization. In this regard, semi-empirical methods are relatively cheap and have been widely applied for different systems. However, many semi-empirical potentials can lead to erroneous results when applied to transition metal clusters. On the other hand, accurate methods, like multiple reference type calculations are too demanding to employ for PES evaluation, as the computational scaling with the number of electrons is usually high. For this reason, DFT is a compromising method in terms of accuracy and computational cost. In general, because of the large number of energy evaluations the cluster sizes are practically limited to 20-30 atoms commonly for transition metals.

3.1.1 Genetic Algorithm

In the present study, an evolutionary inspired method normally a genetic algorithm (GA) has been applied to search the GM isomer. The GA method mimics the evolutionary biology operations such as inheritance, mutation, selection, and crossover [58, 59]. It follows similar mechanism as that of a species changes through time to become better adaptable to the environment and to be fitted for survival. In metallic cluster, the position of each atom in three dimensional space taken as a genome and genetic information exchanged from two individual clusters by "cut-and-splice" operation to pass for the next generation, which is the same as that of the recombination process in reproduction biology [60]. The DFT coupled genetic algorithm (GA-DFT) implemented in Turbomole package by Sierka [61] has been employed in this work to scan the potential energy surface of the metallic clusters. It is based on the Deaven and Ho [60] seminal work. The flow chart of the employed global optimization program is presented in Figure 3.1. The details of the specific steps in the global optimization are also described below.

Initial population

The first step in a GA is usually the generation of initial structures. The initial structures can be provided by the user or automatically generated, or optionally by combining both. Usually a number of initial population structures are generated by distributing atoms in space in a reasonable distance (no disjoint atoms). To generate those automatically, the user has to specify the chemical composition, the number of initial structures intended to be obtained and atomic radii multipliers. The distance between the atoms of the generated structures needs to be in a reasonable bond range. In other words, no atom should be too far away (unbound) or too close (overlapping). For this purpose, nearest neighbors distance evaluation are carried out. Given that R_i is the atomic radius of the considered atom, R_j denotes an atomic radius of the jth neighbour and r_{ij} is the distance between these two atoms, then the atom is flagged as bound if the inequality:

$$r_{ij} < a(R_i + R_j) \tag{3.1}$$
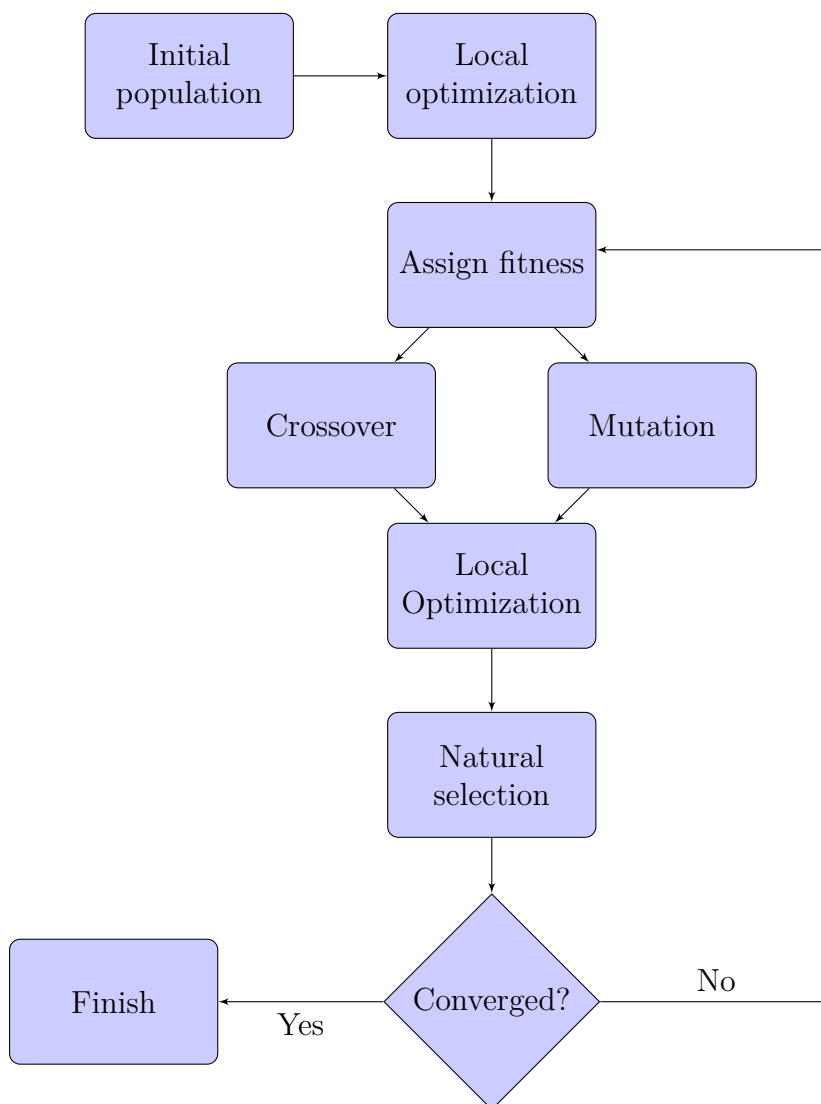
Figure 3.1: Flow chart of the global optimization procedure.

where a is the upper atomic radii multiplier (default $a = 1.2$) and it is adjustable parameter. To explain the equation in words, if the distance to any other atom is smaller than the scaled sum of the atomic radii, the atom is regarded as connected. On the other hand, the atom is flagged as overlapping if the inequality:

$$r_{ij} < b(R_i + R_j) \quad \text{holds.} \tag{3.2}$$

That is, if the distance to any other atom is smaller than the scaled sum of the atomic radii, the atom is not allowed at this position. Here, b is the lower atomic radii with default value of 0.7 and can be adjusted by the user.

Local optimization

Once the initial structures are generated, subsequently they are taken for relaxation to the nearest local minima by minimizing the structures potential energy as a function of their coordinates

using the Turbomole internal local optimization methods. Then, the optimized structures pass to the fitness evaluation step.

Fitness evaluation

A population of local optimized structures is subject to fitness evaluation based on their dynamically scaled relative energy, ε_i.

$$\varepsilon_i = \frac{E_i - E_{min}}{E_{max} - E_{min}}, \tag{3.3}$$

where E_i is the total energy of the given member of the population and E_{min} and E_{max} correspond to the lowest and highest total energies in the population.

Crossover

One of the important operations in the genetic algorithm is crossover, in which evolution from one generation to the next takes place. Two clusters are selected from the population to be parents for mating. This is carried out by employing roulette wheel selection with selection probability proportional to the value of the fitness function. The crossover operation implemented in Turbomole is similar to the one used by Deaven and Ho [60]. The probability p_i of selecting an individual i is proportional to its fitness:

$$p_i = \frac{f_i}{\sum_i f_i} \tag{3.4}$$

and $f_i = e^{-a\varepsilon_i}$, where ε_i is given in eq. 3.3 and a is a constant. Two fitted parent structures are first selected and randomly rotated around their geometrical centers. Then, both clusters are sliced by a random plane and complementary fragments of the parents are combined together to produce a child structure (Figure 3.2).
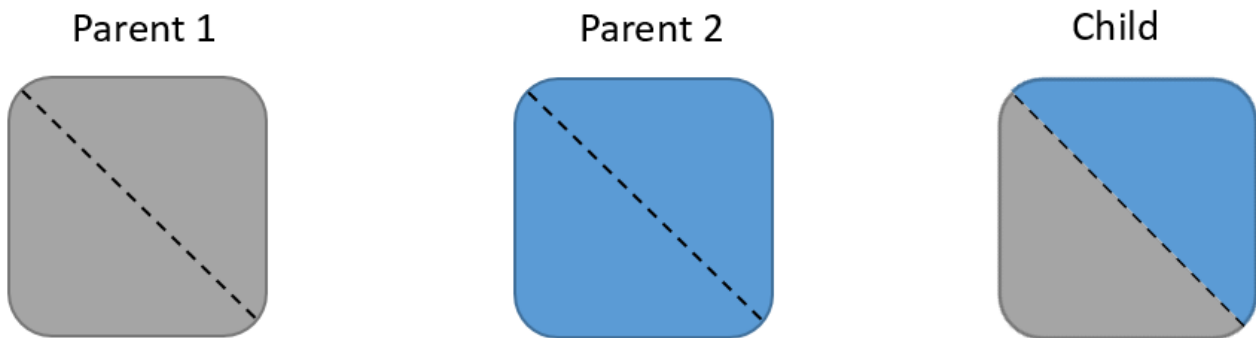

Figure 3.2: Illustration of the crossover operation. The cutting plane is marked by the black dashed line.

Mutation

To avoid premature convergence of the GA and to ensure structural diversity in the population, mutation operations are introduced. A mutation operation is performed by random changes in the structure of randomly chosen parents, for example by twisting, changing positions of selected atoms by randomly generated value, some of the atoms translated by some distance in random direction or by switching the types of two atoms in the case of mixed composition. Mutated structures are locally minimized and added to the population. The mutation rate is usually kept below 1% of all structures in all generations.

Natural selection

For the purpose of maintaining diversity during the GA runs, similarity recognition algorithms are used. The similarity of two structures is determined comparing eigenvalues of their inertia tensors, the radial distribution of atoms, the average atomic distances, the variance of atomic distances and the asymmetry, or skewness of the distribution of distances. After sorting the population into groups, the structures are ordered in a list that includes the most stable structure from each group, then the second most stable, and so on. The next generation of parent structures is created by choosing the M best structures from the list.

3.2 Trapped Ion Electron Diffraction (TIED)

For the experimental measurement, a mass selective method of structure determination technique, namely trapped ion electron diffraction (TIED) have been employed. Since the scattering patterns depend on the spatial arrangement of the scattering atoms, commonly diffraction measurements are applied for structural determination. In this work, the TIED measurements were conducted by Dennis Bümuller in Detlef Schooss group. Here, only a short summary of the working principles of TIED is presented and for further details it is referred to reference [62, 63]. The main components of the TIED instrument are illustrated in Figure 3.3. First, the metal sample is placed into a magnetron sputtering source and cluster anions are generated. Then, the cluster ions are stored in a quadruple ion trap after passing through the bender. A single cluster size is selected based on the mass to charge ratio using a time-of-flight MS. An electron beam strikes the ion cloud with kinetic energy of 40 keV and at an electron beam current of 1 - 2 μA. The diffracted electrons from the clusters are detected by a phosphor screen assembly, which is connected to a CCD camera (placed external to the UHV chamber). Reference pictures were accumulated by repeating the measurement without cluster ions in the trap. Around 200 - 1500 pictures were taken in one measurement that corresponds to a total measurement time of 14 - 100 hours at a trap temperature of $\sim$ 95 K. The averages of references and summed cluster signals were subtracted from each other. Figure 3.4 shows an example of the CCD camera recorded average diffraction pattern of Pt_{13}^-. From the subtracted picture, the total diffraction intensity I_{tot}^{exp} as a function of the electron momentum transfer (s) were
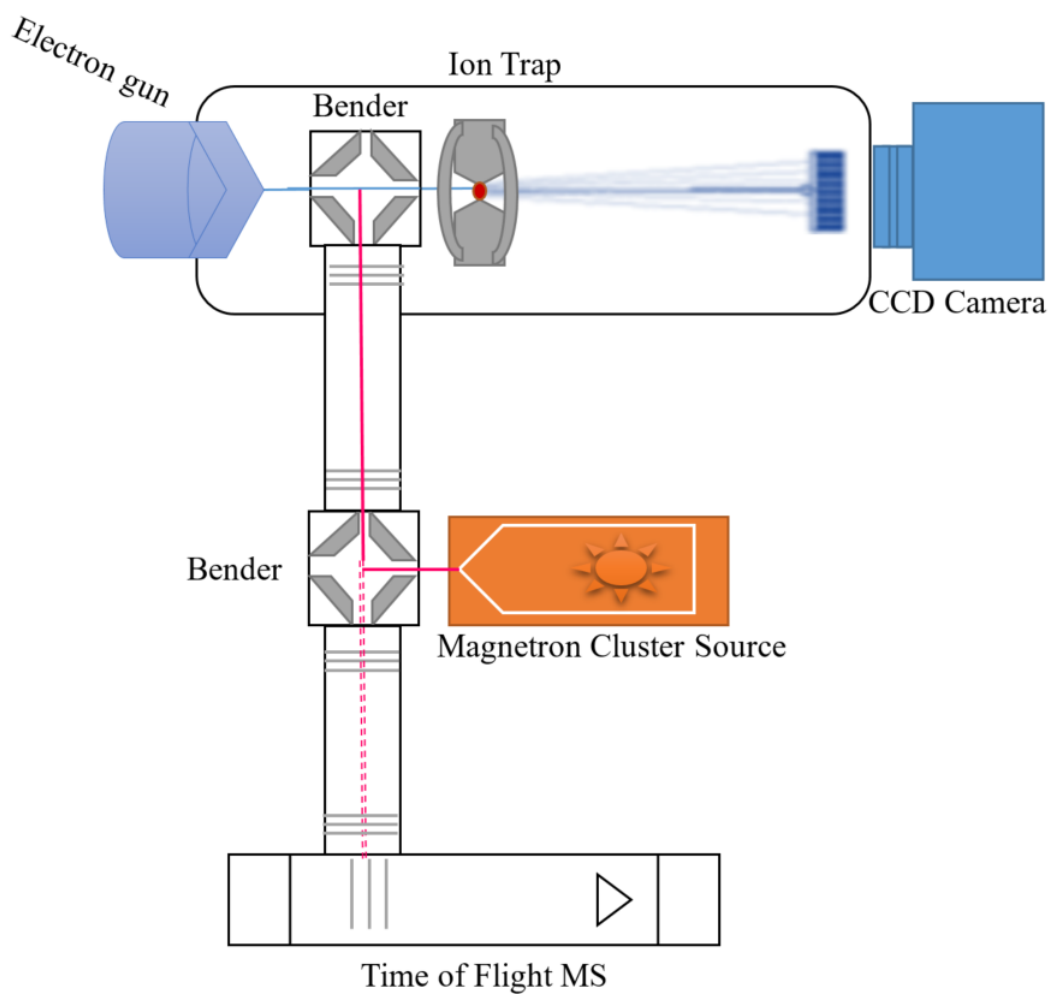
Figure 3.3: The trapped ion electron diffraction instrument setup with the main components. It has three main parts; the magnetron sputter cluster source, the time-of-flight mass spectrometer and the UHV chamber housing the diffraction beamline [62].
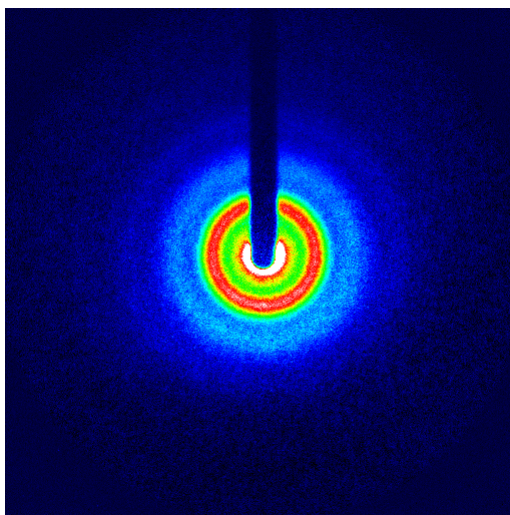

Figure 3.4: Averaged diffraction patterns of Pt_{13}^- recorded using CCD camera (shared from Dennis Bümuller).

obtained.

$$s = 2.\frac{2\pi}{\lambda}\sin(\frac{\theta}{2}) \tag{3.5}$$

where θ is the scattering angle and λ is the electron wavelength. The experimental molecular scattering intensity sM^{exp} can be defined by

$$sM^{exp}(s) = s\left(\frac{I_{tot}^{exp}}{I_{at}I_{back}} - 1\right) \tag{3.6}$$

where I_{at} is the atomic scattering contribution and I_{back} is an additional unspecific flat background.

For the homo-nuclear cluster system, the theoretical modified molecular scattering function sM^{theo} can be obtained from the calculated structures by

$$sM^{theo}(s') = \frac{S_c}{N}exp\left(-\frac{L^2}{2}s'^2\right)\sum_i\sum_{i\neq j,j=1}\frac{\sin(r_{ij}s')}{r_{ij}} \tag{3.7}$$

where $s' = k_s s$, N is the number of atoms in the cluster, S_c and k_s are scaling factors, and r_{ij} is the distance between two atoms in the cluster. L^2 is the harmonic mean squared vibrational amplitude averaged over all distances in the cluster and accounts for thermal vibrations. The comparison of the experimental and theoretical data is done using χ^2 fit.

$$\chi^2 = \sum_i w_i(sM_i^{theo} - sM_i^{expt}) \tag{3.8}$$

The agreement between the experimental scattering function and simulated scattering function of the model structure is quantified by a weighted profile factor

$$R_w = \sqrt{\frac{\sum_i w_i\left(sM_i^{theo} - sM_i^{expt}\right)^2}{\sum_i w_i\left(sM_i^{expt}\right)^2}} \tag{3.9}$$

where the weighting factors w_i are calculated from the (error propagated) standard deviation of the experimental data

$$w_i = \frac{1}{\sigma_i^2(s)} \tag{3.10}$$

Comparison of different R_w values (obtained for different trial structures) are only meaningful within a single experimental data set. The R_w value is normalized and can take values between 0 and 1 or 0 and 100 %. In general, the smaller the R_w, the better the agreement between theory and experiment. There is no strict criterion of R_w to discard the structure but usually the acceptable R_w value is below 5%. Furthermore, it can happen that several structures contribute to the diffraction intensity. In this case, it can be addressed by taking a mixture of two structures, in which the second model structure with a different structural motive is involved in the fit.

3.3   Computational Details

All calculations were conducted with the Turbomole package [64] using DFT. The global minimum scanning on the PES was performed using the hybrid *ab initio* genetic algorithm (HAGA) as depicted schematically via the flow chart in Figure 3.1. For the GA calculation, a population size of 30 structures with 10 children has been employed. The calculations are carried out until no new minimum structures were found and typically the putative global minimum structures had been obtained in less than 35 generations. In the employed GA, each structure in the population and every child in each generation requires a local structure optimization using DFT and it is computational quite demanding especially for the current open shell systems of Pt_n^-. For that reason, a split valence polarization (def2-SVP) basis set [65] and the BP86 functional [66] were employed to reduce the computational effort. Low energy structures obtained in this way have been subsequently re-optimized at PBE [67], TPSS [68] and TPSSH [68, 69] level in combination with the def2-TZVP basis set [65, 70]. At least ten structures of each size have been subject to re-optimization. All calculations in this work have been carried out without symmetry restrictions. However, the symmetries of the optimized structures are determined using the Turbomole *desy* command with a tolerance of up to 1.

All DFT calculations have been conducted in the spin polarized formalism using the RI-J (resolution of the identity for the coulomb term J) [71, 72] approach and core electrons were described via effective core potential (ECP), which account for scalar relativistic effects. Electrons filling up 1s - 4f atomic orbitals were treated by ECP while 5s, 5p, 5d and 6s electrons were left in the valence shell [73]. During the re-optimization, an SCF convergence threshold of 10^{-7} Hartree and grid size 3 were used. Encountering convergence problems were quite common in the current work. In all cases when convergence has not been reached within 3000 SCF iterations, the damping and orbital shift have been changed to a starting and ending value of around 10 and 0.5, respectively. As Pt clusters can exist in different spin states, Fermi smearing has been applied to allow fractional occupation with an initial temperature T = 600 K, which was progressively lowered during the SCF iterations up to T = 50 K. In this way, by starting the calculation from high spin states with smearing, usually integer occupations of the appropriate spin state were achieved. To confirm that the final structures are real local minima i.e. the Hessian matrix has only non-negative eigenvalues, second derivatives calculations were conducted for the relaxed structure.

Correction calculations such as spin-orbit coupling (SOC) effect, random phase approximation (RPA) and dispersion corrections were conducted on top of the TPSS optimized structures. All the corrections applied were single point energy calculations. The spin-orbit coupling effect on the relative energies of the isomer structures were assessed based on the relativistic two-component (2c) calculations [74]. The SOC calculations were carried out with a dhf-TZVP-2c basis set which is a special type of extended basis set devised for SOC [75, 76]. Single point random phase approximation (RPA) calculations were also performed to evaluate correlation effects [77] with the RI-J formalism and auxiliary basis (jbas and cbas). Furthermore, the effects of dispersion correction were evaluated for selected systems. The third generation dispersion

(DFT-D3) correction with Becke-Johnson damping is used [78]. The dispersion corrected energy [79] is defined as

$$E_{DFT-D3} = E_{DFT} + E_{disp}, \tag{3.11}$$

where E_{DFT} is the usual DFT computed energy and E_{disp} is a dispersion correction energy. The E_{disp} depends only on the molecular geometry and does not depend on the electronic structure of the system.

The thermal corrections to the DFT energy are included via the thermodynamic Gibbs free energy at the experimental conditions (95 K and 1 mbar). The change in the total Gibbs free energy is defined as

$$\Delta G_{total} = \Delta E_{DFT} + \Delta G_{thermo}, \tag{3.12}$$

where ΔE_{DFT} is the change in energy from DFT and ΔG_{thermo} is calculated as

$$\Delta G_{thermo} = \Delta H - T\Delta S \tag{3.13}$$

For the Gibbs free energy calculation, the rotational symmetry factor is considered.

For energetic and geometrical analysis of the final structures, the following definitions are used throughout the present work. As a measure of stability, the cohesive energy per atom for singly charged clusters defined as

$$E_{coh} = \frac{(N-1)E_1 + E_1^- - E_N^-}{N} \tag{3.14}$$

where E_1 and E_1^- are the energies of single Pt atom and an ion respectively, and E_N^- is the energy of a singly charged N-atomic Pt cluster. The relative stability of a particular cluster, Pt_n^- with respect to its neighboring sizes, Pt_{n-1}^- and Pt_{n+1}^- commonly called second order difference (SOD) given by

$$\Delta E^2(Pt_n^-) = E_{tot}(Pt_{n-1}^-) + E_{tot}(Pt_{n+1}^-) - 2E_{tot}(Pt_n^-) \tag{3.15}$$

For a quantitative measure of similarity between two superimposed clusters of atomic coordinates, the root mean square deviation (RMSD) [80] technique is used as implemented in ASE [81]. This RMSD uses the rotational and transnational operations to superimpose and find the best similarity between any two structures. The order of atoms indexing is also considered. Given two structures A and B containing equal numbers of atoms, the RMSD is calculated as:

$$RMSD(A,B) = \sqrt{\frac{\sum_{i=1}^{N}\left(\left(A_{ix} - B_{ix}\right)^2 + \left(A_{iy} - B_{iy}\right)^2 + \left(A_{iz} - B_{iz}\right)^2\right)}{N}} \tag{3.16}$$

where A_{ix} is the cartesian position of atom i in structure A and B_{ix} is the cartesian position of atom i in structure B in the x coordinate.

Chapter 4

Benchmark Calculations

Before going to the results sections of the work, the reliability of the calculation methods are assessed by some benchmark calculations. First, the influence of the density functionals and basis sets are investigated for the small Pt clusters, which are presented in Part I. In part I all calculations are performed using Turbomole. In part II, the plane wave cutoff energy and lattice constant parameters are calibrated and presented for Pt and Pd using Vasp code.

4.1 Part I

4.1.1 Pt dimer

Benchmark calculations have been performed for the neutral and negatively charged Pt_2 dimer and compared with the available experimental spectroscopic data [82] and quantum chemical calculations [83]. The bond length (r), the dissociation energy (D_e) and vibrational frequencies (ω) were calculated at BP86, PBE, TPSS and TPSSH levels with the def2-TZVP basis set. The spin-orbit coupling effect was also assessed for these density functionals with a dhf-TZVP-2c basis set. The results are summarized in Table 4.1. The dissociation energy for the Pt dimer is defined as: $D_e = E(Pt_2^-) - E(Pt^-) - E(Pt)$ for anion dimer and $D_e = E(Pt_2) - 2E(Pt)$ for neutral dimer.

The ground state of the neutral dimer was found in the triplet state for all of the density functionals applied. The previous work at ab initio CASPT2 level, reported that the ground state is triplet, which basically corroborates this work [84]. The equilibrium bond length is in very good agreement with the experimental data for all the four density functionals, in which the worst difference was below 1%. The vibrational frequency agreement with the experiment is moderately good for the four density functionals with the highest difference of about 8% in the case of TPSSH. The dissociation energy is somewhat overestimated in all cases except at TPSSH. The maximum deviation of D_e to experiment is found to be 13%, which is at PBE level. However, when SOC is included in the calculation the deviation to experiment is lowered for all cases, thereby the maximum deviation is less than 8%. Another reported theoretical work that is close to the experimental data obtained by employing CCSD(T) with r = 235 pm, D_e = 3.38 eV and ω = 228 cm^{-1} [83]. Taken as a whole, the bond length is increased up on

17

SOC inclusion, and consequently the value of D_e and ω becomes decreased.

Table 4.1: The calculated values of bond length (r) in pm, dissociation energy (D_e) in eV and vibrational frequency (ω) in cm^{-1} for Pt_2 and Pt_2^- dimer together with the corresponding measured data. The spin-orbit (SOC) calculations are performed using dhf-TZVP-2c basis set, while the others are using def2-TZVP basis set.

Method	Pt_2			Pt_2^-		
	r	D_e	ω	r	D_e	ω
BP86	235.3	3.43	226	241.5	3.47	198
BP86/SOC	238.8	3.31	211	243	3.30	191
PBE	234.6	3.55	231	241.3	3.54	198
PBE/SOC	237.8	3.38	217	242.8	3.37	191
TPSS	235.2	3.38	227	240.3	3.47	204
TPSS/SOC	236.5	3.27	220	239.9	3.37	170
TPSSH	234.2	3.04	234	239.9	3.96	207
TPSSH/SOC	236.4	2.98	196	239.8	3.11	206
CCSD(T)[83]	235.0	3.38	228	—	—	—
Exp.	234.0[85]	3.14±0.02[86]	215±15[82]		2.91±0.03[82]	178±20[82]

The ground state of the Pt_2^- anion is a doublet state with all functionals. The bond length is determined to be slightly elongated compared to the neutral dimer because of the one extra electron which gives rise to weakening of the bond strength. The vibrational frequency is also decreased compared to the neutral dimer, as a consequence of weakening of the bond. The calculated values of $\omega = 170$ - 207 cm^{-1} are fairly close to the experimental value $\omega = 178\pm20$ cm^{-1} (Table 4.1). However, unexpectedly the D_e value is larger than the neutral dimer at least at TPSS and TPSSH level, see Table 4.1. Moreover, the calculated $D_e = 3.54$ eV (PBE) substantially differ from experimental D_e value of 2.91 ± 0.03 eV [82]. Analogues to the case of the neutral dimer, the inclusion of SOC significantly improves the D_e result. At BP86 level by including SOC, it was found that D_e value of Pt_2 is greater than Pt_2^-, which was the opposite before SOC is applied (Table 4.1). Another theoretical study at PW91 level [87] has found r = 244 pm, $D_e = 3.79$ eV and $\omega = 208$ cm^{-1}, which is favorably in line with the present work. From this, one can understand, essentially that DFT functionals overestimate the bond dissociation energy. In general, apart from this slight discrepancy on the dissociation energy, the applied DFT functionals in particular TPSS have shown very good agreement with the experimental data and other theoretical reports.

4.1.2   Basis set effect

To assess the effect of basis sets on the energetic and structural properties, Pt_6^- and Pt_{11}^- isomers are chosen. These structures are presented in Figures 5.1 and 5.10. It should be noted that the relative energy is the main interest rather than the absolute energy. In Table 4.2, the effect of basis sets on the relative energy is illustrated. From the result we can see two important

information. First, changing the basis sets does not affect the relative energy ordering. Second, very close relative energy results are obtained for def2-TZVP and def2-QZVP, while de2-SVP is slightly deviated.

Table 4.2: The relative energy $E_{relative}$ (eV) with basis set variation for Pt_6^- and Pt_{11}^- clusters of different isomers at TPSS level. The numbering given to different isomers are according to Figures 5.1 and 5.10.

	def2-SVP	def2-TZVP	def2-QZVP
Cluster	$E_{relative}$	$E_{relative}$	$E_{relative}$
Pt_6^- (1)	0.00	0.00	0.00
Pt_6^- (2)	0.04	0.11	0.15
Pt_6^- (3)	0.23	0.30	0.31
Pt_{11}^- (1)	0.00	0.00	0.00
Pt_{11}^- (2)	0.001	0.067	0.07
Pt_{11}^- (3)	0.24	0.32	0.24
Pt_{11}^- (4)	0.52	0.54	0.49

The other important point is how does the basis set change affect the structure. To measure the structural change with basis sets, RMSD calculation is performed. The calculated RMSD results for the various isomers of Pt_6^- and Pt_{11}^- clusters are shown in Table 4.3. The RMSD is calculated with reference to the def2-QZVP optimized structures for each isomers. As can be seen, for all cases very slight structural deviation is observed up on basis sets change. Moreover, the deviation observed between def2-QZVP and def2-TZVP is smaller than the deviation between def2-QZVP and def2-SVP.

Table 4.3: The effect of basis set variation on the geometry of Pt_6^- and Pt_{11}^- clusters of different isomers at TPSS level. The structural difference is given in RMSD (Å) and it is calculated with reference to def2-QZVP optimized structure. The numbering given to different isomers are according to Figures 5.1 and 5.10.

Basis set	Pt_6^- (1) RMSD	Pt_6^- (2) RMSD	Pt_6^- (3) RMSD	Pt_{11}^- (1) RMSD	Pt_{11}^- (2) RMSD	Pt_{11}^- (3) RMSD	Pt_{11}^- (4) RMSD
def2-QZVP	0.000	0.000	0.000	0.000	0.000	0.000	0.000
def2-TZVP	0.011	0.015	0.015	0.016	0.013	0.016	0.015
def2-SVP	0.053	0.029	0.026	0.036	0.031	0.038	0.033

4.1.3 Density functionals effect

To assess the effect of density functionals on the energetic and structural properties of the systems under this study, generalized gradient approximation GGA (PBE), meta-GGA (TPSS) and hybrid (TPSSH) functionals are chosen. Cluster sizes Pt_6^-, Pt_7^- and Pt_{11}^- are selected

randomly for comparison and presented in Table 4.4. As it can be seen, the calculated relative energy differences across the three functionals are substantial compared to the basis set effect observed above. Furthermore, even the relative energy ordering is changed at Pt_7^- because of the density functionals change. The other structural parameter provided in Table 4.4 is the scattering function agreement (R_w) between TIED measured and DFT simulated structures. The R_w differences for the same isomer across the density functionals indicate the structural deviations. For the best theory and experiment agreed structures (lowest R_w), i.e., Pt_6^- (1), Pt_7^- (5) and Pt_{11}^- (3) isomers, TPSS have given relatively better R_w value.

Table 4.4: Relative energies (in eV) for Pt_6^-, Pt_7^- and Pt_{11}^- clusters at TPSS , PBE and TPSSH level. The measured and simulated structures scattering function agreement (R_w) is also given. The numbering given to different isomers are according to Figures 5.1, 5.3 and 5.10.

| | TPSS | | PBE | | TPSSH | |
Structure	$E_{relative}$ (eV)	$R_w(\%)$	$E_{relative}$ (eV)	$R_w(\%)$	$E_{relative}$ (eV)	$R_w(\%)$
Pt_6^- (1)	0.00	1.68	0	1.75	0	1.79
Pt_6^- (2)	0.11	7.84	0.14	7.94	0.22	7.72
Pt_6^- (3)	0.30	10.37	0.26	10.38	0.53	10.31
Pt_7^- (1)	0.00	8.19	0.00	8.35	0.00	8.01
Pt_7^- (2)	0.21	6.47	0.11	6.45	0.38	6.27
Pt_7^- (3)	0.22	17.8	0.01	17.8	0.45	17.75
Pt_7^- (4)	0.35	4.21	0.34	3.23	0.27	3.43
Pt_7^- (5)	0.90	2.61	0.96	2.64	0.61	3.26
Pt_{11}^- (1)	0.00	19.51	0.00	19.88	0.00	20.39
Pt_{11}^- (2)	0.07	12.89	0.02	13.16	0.05	13.00
Pt_{11}^- (3)	0.32	2.88	0.43	10.63	0.34	2.99
Pt_{11}^- (4)	0.54	9.13	0.51	9.31	0.41	5.67

To sum up, the basis set difference effect on the structural and energetic properties is fairly small especially between the basis sets def2-TZVP and def2-QZVP. Consequently, the results presented in this work are obtained by employing def2-TZVP basis set unless otherwise specified. Regarding density functionals, it is not conclusive to choose one of the functional based on the relative energy results. However, in most cases TPSS shows better structural agreement (R_w) with the TIED measured data. The cohesive energy calculation in section 5.1.1 (Figure 5.16) has also confirmed that TPSS structures show better stability. For these reasons and because of its overall good performance, further detailed calculations in this work have been carried out with the TPSS functional unless explicitly stated and the structures presented here are from TPSS optimization.

4.2 Part II

In this section, some factors that could affect calculations of adsorption properties on nanoparticles based on Vasp code are presented. For the cutoff energy and lattice constant calculations a (12 x 12 x 12) k-point mesh based on the Monkhorst-Pack scheme [88] were used to sample the Brillouin zones.

Energy dependence on cutoff energy

The Kinetic cutoff energy is one of the parameters that influence the accuracy and computational cost of the plane wave based calculations. Usually higher cutoff energy provides better accuracy, but requires large computational cost. Due to computational limitations, calibration of convergence of cutoff energy to some value that could meet the requirements is valuable. Here, single point energy calculations were performed to the bulk Pt and Pd to check the convergence of cutoff energy using PBE. As can be seen from Figure 4.1, the cutoff energy converges with in 0.2 meV for Pd at 400 eV and Pt at 450 eV. Therefore, a cutoff energy of 450 eV were chosen.
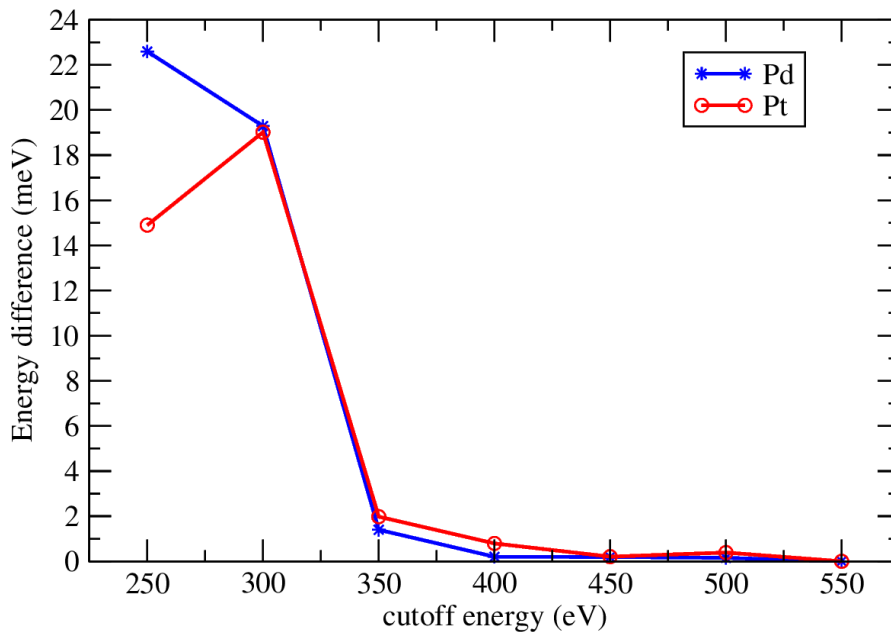

Figure 4.1: Convergence of total energy with respect to cutoff energy for bulk Platinum.

Equilibrium lattice constant

The equilibrium lattice constant of Pt and Pd fcc bulk structure is calibrated with total energy and used to construct model structures. A cutoff energy of 450 eV is used. As shown in Figure 4.2, the equilibrium lattice constant (in Å) is calculated to be 3.97 for Pt and 3.94 for Pd. The experimental lattice constants for Pd is 3.89 and for Pt is 3.92 [89]. The discrepancy between the calculated equilibrium lattice constants and the experimental results is less than 1.5 % for both Pt and Pd.
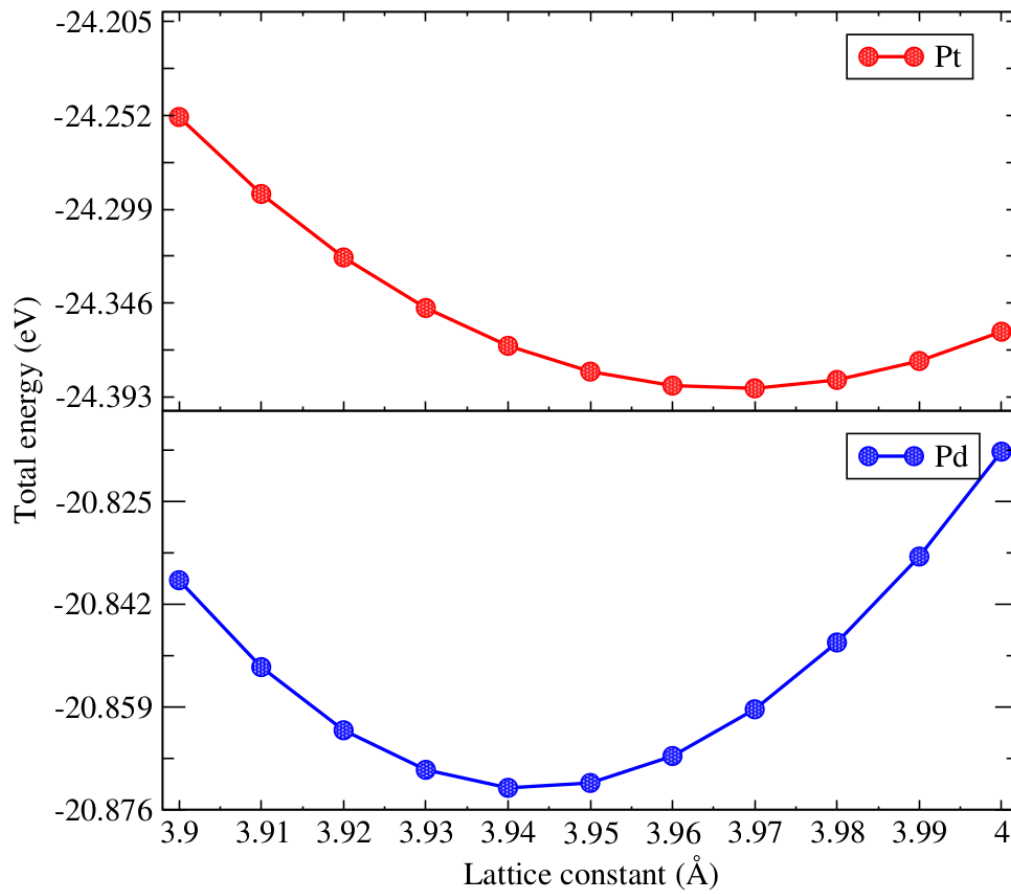

Figure 4.2: Total energy at different lattice constants using PBE functional. The calculated equilibrium lattice constant for Pt is 3.97 and for Pd is 3.94.

Results and Discussion

5.1 Structures of the Pt_n^- Clusters

In this chapter, anionic platinum cluster structures in size range 6 - 13 have been studied and presented. In the present work, a DFT based genetic algorithm (GA-DFT) global optimization method has been used to search the global minimum structures. All low energy structures obtained from GA-DFT calculations have been compared by Bumüller and Schooss (INT, KIT) with the mass selected cluster ions TIED scattering measurement. All figures showing the comparison of experimental and calculated scattering functions have been provided by Bumüller and Schooss. Based on the quality of agreement the most probable structures for each size are assigned. For each cluster size considered, I have presented here the DFT calculated lowest-energy structures and structures that shows better agreement with the measured data which are in some cases relatively high in energy. It has to be noted that in many cases within 0.1 eV relative energy difference several structures have been obtained. For those selected low-energy configurations at different sizes, geometry optimization were carried out at three DFT functionals that is GGA (PBE), meta-GGA (TPSS) and hybrid (TPSSH). As the energy differences between the isomers are usually small, it can happen that the energetic ordering changes when the density functional varied. However, virtually it was found that TPSS shows better agreement with the experimental measurements and this was mentioned in the previous works as well [13, 90]. Table 5.1 presents the summary of energetic ordering of isomer structures of various cluster sizes. The thermodynamic Gibbs free energy (ΔG) is also calculated for each of the structures at experimental condition (T = 95 K and p = 1mbar). The symmetry number and the spin multiplicities are taken into account for ΔG calculation. The pressure and the symmetry number effects on ΔG are in the order of meV. As a result, the relative energy ordering of the isomer structures is not changed.

Pt_6^- Cluster

For Pt_6^-, the low-energy structures at TPSS level are shown in Figure 5.1 and Table 5.1. Within 0.29 eV relative energy difference three isomer structures have been obtained. The putative global minimum (GM) structure (1) has a planar triangular geometry with D_{3h} symmetry
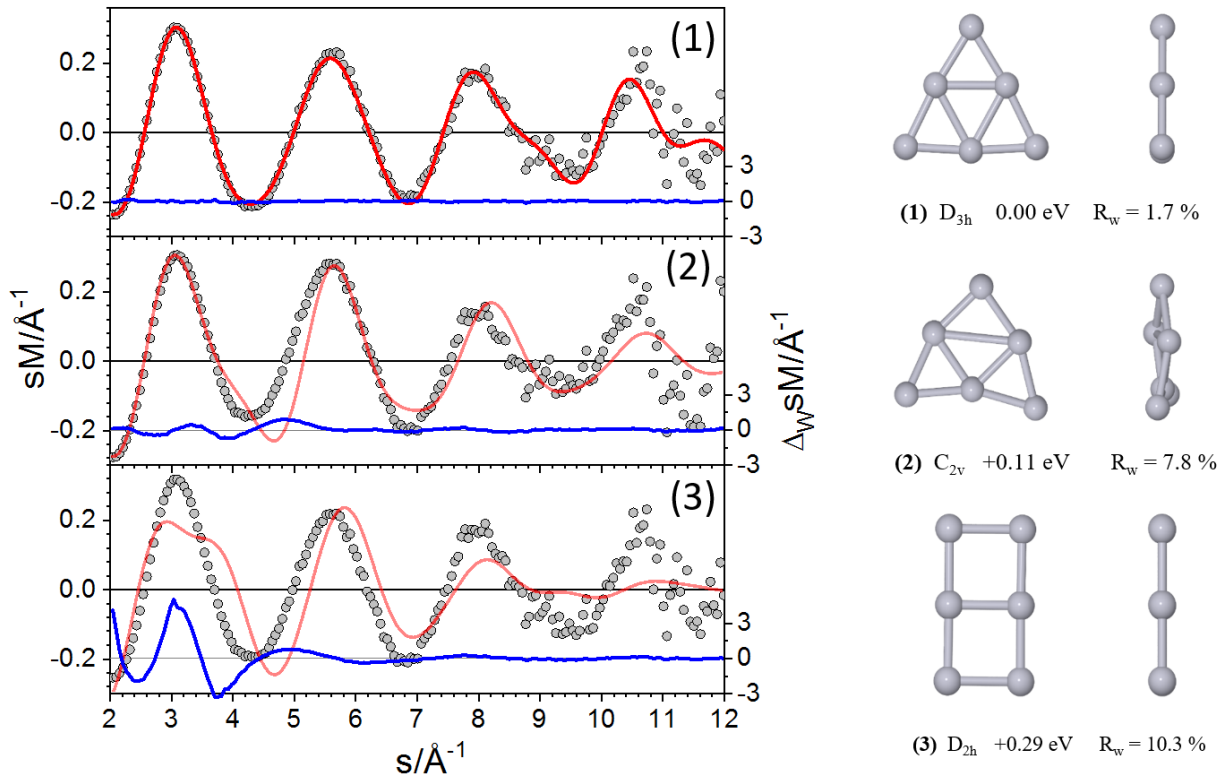
Figure 5.1: Three lowest-energy structures of Pt_6^- (right panel) together with their PG, relative energy and R_w. The plot (left panel) is comparison of experimental (gray open circles) and theoretical (red line) modified molecular scattering function (Eq. 3.6 and Eq. 3.7) for isomers (1) - (3). The blue line shows the weighted deviation between experiment and theory (Eq. 3.8). The three structures were compared with a single experimental data set and the corresponding plot is labeled with isomer number.

that contains four interior equilateral triangles inside of the exterior triangle and has 254 pm average bond length. The putative GM structure has been found to have $R_w = 1.7\%$, which is a remarkable agreement with the measured scattering function. The next isomer (2), a distorted triangular with C_{2v} symmetry is 0.11 eV (0.22 eV with SOC) higher in energy and has 7.8 % R_w. The third isomer (3) is a planar ladder-like structure with D_{2h} point group (PG). It has +0.29 eV (+0.44 with SOC) energy to the GM and the R_w value, i.e. the experimental agreement is 10.3 %. The spin multiplicity state for all the three isomers were found to be doublet. The evidence from this study suggests that the inclusion of SOC has significant influence the relative energy difference, but the ordering remains the same. Moreover, neither the dispersion correction nor RPA affected the energetic ordering, see Table 5.1. A similar influence of SOC on relative energies of late transition metal clusters especially on Pt and Au has been reported [91, 92]. The latter two structures (2) and (3) can be simply ruled out because of their relative high energy and high R_w. Interestingly structure (1) found to be the lowest-energy structure at PBE and TPSSH level as well and fits well to the TIED measurement molecular scattering with low profile factor ($R_w = 1.7\%$). Hence, all the results confirm that the putative GM structure of Pt_6^- should be the planar triangular structure (1).

Table 5.1: Relative energies (in eV) for Pt clusters of different size at pure TPSS and TPSS/dispersion, TPSS/RPA and TPSS/SOC level. The thermodynamic Gibbs free energy (ΔG) and the average bond length (d_{av}) are also presented. ΔG is calculated at T = 95 K and p = 1mbar. The measured and simulated structures scattering function agreement (R_w) is also given. The numbering given to different isomers are according to Figures 5.1, 5.2, 5.4, 5.6, 5.8, 5.10, 5.12 and 5.14.

Cluster	TPSS	TPSS/ Dispersion	TPSS/ RPA	TPSS/ SOC	ΔG (eV)	2S+1	PG	d_{av} (pm)	R_w(%)
Pt_6^- (1)	0.00	0.00	0.00	0.00	0.00	2	D_{3h}	253.7	1.7
Pt_6^- (2)	0.11	0.11	0.07	0.22	0.07	2	C_{2v}	250.0	7.8
Pt_6^- (3)	0.29	0.31	0.37	0.44	0.30	2	D_{2h}	245.2	10.3
Pt_7^- (1)	0.00	0.00	0.05	0.021	0.00	6	C_{2v}	258.8	8.2
Pt_7^- (2)	0.21	0.17	0.00	0.028	0.22	2	D_{3d}	255.2	6.5
Pt_7^- (3)	0.22	0.26	0.25	0.00	0.23	4	C_s	247.8	17.8
Pt_7^- (4)	0.35	0.28	0.31	0.01	0.37	2	C_2	258.8	4.2
Pt_7^- (5)	0.90	0.84	0.84	0.67	0.92	2	C_s	258.3	2.6
Pt_8^- (1)	0.00	0.00	0.00	0.00	0.00	4	C_s	258.9	8.2
Pt_8^- (2)	0.24	0.31	1.21	0.13	0.22	2	C_s	257.9	7.9
Pt_8^- (3)	0.29	0.34	1.04	0.25	0.28	4	C_1	256.8	4.8
Pt_8^- (4)	0.31	0.51	1.28	0.33	0.30	2	C_2	251.2	13.1
Pt_8^- (5)	0.53	0.55	1.29	0.35	0.52	4	C_1	261.5	2.0
Pt_9^- (1)	0.00	0.00	0.00	0.05	0.00	2	C_s	257.5	21.1
Pt_9^- (2)	0.15	0.17	1.21	0.02	0.14	2	C_2	262.9	7.3
Pt_9^- (3)	0.16	0.16	1.97	0.00	0.15	2	C_1	258.2	12.4
Pt_9^- (4)	0.94	1.01	2.89	0.56	0.92	2	C_s	262.2	4.9
Pt_{10}^- (1)	0.00	0.00	1.40	0.00	0.00	8	T_d	266.5	5.9
Pt_{10}^- (2)	0.11	0.12	1.32	0.14	0.13	6	C_s	265.1	3.6
Pt_{10}^- (3)	0.20	0.187	0.96	0.35	0.25	2	C_2	258.3	18.3
Pt_{10}^- (4)	0.21	0.186	0.00	0.28	0.25	2	C_2	260.3	5.7
Pt_{11}^- (1)	0.00	—	—	0.00	0.00	2	C_2	260.8	19.5
Pt_{11}^- (2)	0.07	—	—	0.14	0.07	2	C_1	258.2	12.3
Pt_{11}^- (3)	0.32	—	—	0.16	0.32	2	C_s	264.9	2.9
Pt_{11}^- (4)	0.54	—	—	0.36	0.53	2	C_1	262.1	9.1
Pt_{12}^- (1)	0.00	—	—	0.00	0.00	2	C_1	259.5	26.0
Pt_{12}^- (2)	0.14	—	—	0.03	0.11	2	C_s	261.8	15.5
Pt_{12}^- (3)	0.35	—	—	0.25	0.33	2	C_1	260.8	6.8
Pt_{12}^- (4)	0.63	—	—	0.18	0.59	8	C_{2v}	266.8	3.0
Pt_{13}^- (1)	0.00	—	—	0.00	0.00	2	C_s	260.3	25.6
Pt_{13}^- (2)	0.36	—	—	0.32	0.36	2	C_1	261.2	11.2
Pt_{13}^- (3)	0.46	—	—	0.141	0.45	2	C_1	264.1	5.4
Pt_{13}^- (4)	0.61	—	—	0.145	0.58	2	C_{3v}	267.8	4.1

Pt$_7^-$ Cluster

In the case of Pt$_7^-$, four low-energy isomers and one isomer with a small profile factor but relatively high energy, i.e. a total of five isomers are presented, see Figure 5.2 (for the geometry) and Figure 5.3 (for scattering fit with TIED). The most stable structure of Pt$_7^-$ is a bi-capped edge triangle (1) with C_{2v} point group and sextet electron spin state. This structure can be obtained from the lowest-energy structure of Pt$_6^-$ (1) by just adding one Pt atom at one of the edges. It is worth to mention that a similar motif in C_s symmetry has been proposed as global minimum for the neutral Pt$_7$ using a DFT based genetic algorithm global optimization method [43]. The next low energy (+0.21 eV) structure (2) is warped hexagonal with D_{3d} symmetry and a doublet spin state. The third lowest energy geometry is a planar side-capped ladder like (3) just 0.22 eV above the global minimum and found in the quartet spin state. The fourth structure, 0.35 eV above the global minimum is side capped triangle (4) and would seem to be the growth of the putative global minimum of Pt$_6^-$ by adding a Pt atom at one of the sides. Its spin state and point group are found to be doublet and C_2, respectively. This geometry shows agreement with TIED measurement with profile factor ($R_w = 4.2$ %). The other structure (5), that shows even better agreement to the measurement with $R_w = 2.6$ % is found to be 0.90 eV above the global minimum. This structure has a lower symmetry with C_s PG and its spin multiplicity is doublet.
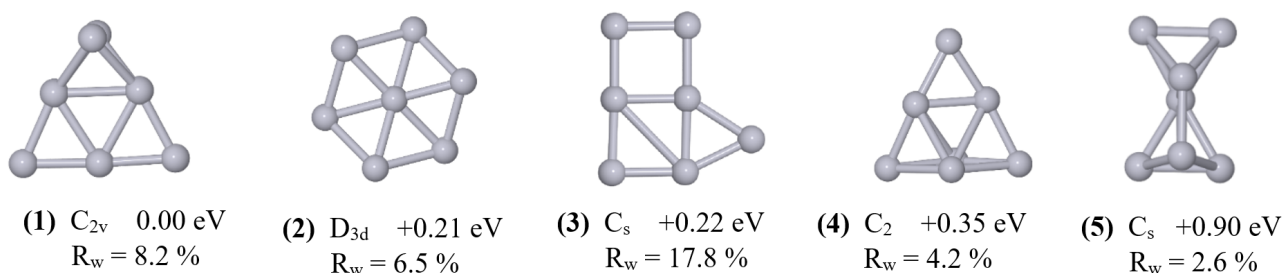

(1) C$_{2v}$ 0.00 eV
R_w = 8.2 %

(2) D$_{3d}$ +0.21 eV
R_w = 6.5 %

(3) C$_s$ +0.22 eV
R_w = 17.8 %

(4) C$_2$ +0.35 eV
R_w = 4.2 %

(5) C$_s$ +0.90 eV
R_w = 2.6 %

Figure 5.2: Lowest energy and best fitted to TIED isomers of Pt$_7^-$ with their corresponding PG symmetry, relative energy and R_w.

The inclusion of SOC calculations on top of TPSS has shown significant influence on the relative energies of the isomers. As can be seen in Table 5.1, the SOC influenced the relative energy substantially and the putative GM becomes structure (3) even though the next isomers are just a few meV above it. The relative energy of the better fitted structure (5) lowered from 0.90 eV to 0.67 eV. The incorporation of dispersion correction on top of TPSS does not affect the relative energy much and the ordering remains the same as the TPSS. Comparison with the TIED measurement has shown that structure (5) has a very good profile factor ($R_w = 2.6$ %), however, it is 0.67 eV (with SOC) higher than the putative GM isomer (3). On the other hand, structure (4) with $R_w = 4.2$ % can be a potential candidate because the relative energy is lowered to 0.01 eV after the inclusion of SOC. Here, there is uncertainty to assign either isomer (4) or isomer (5) as the fact that both have acceptable R_w value but (5) has even slightly better
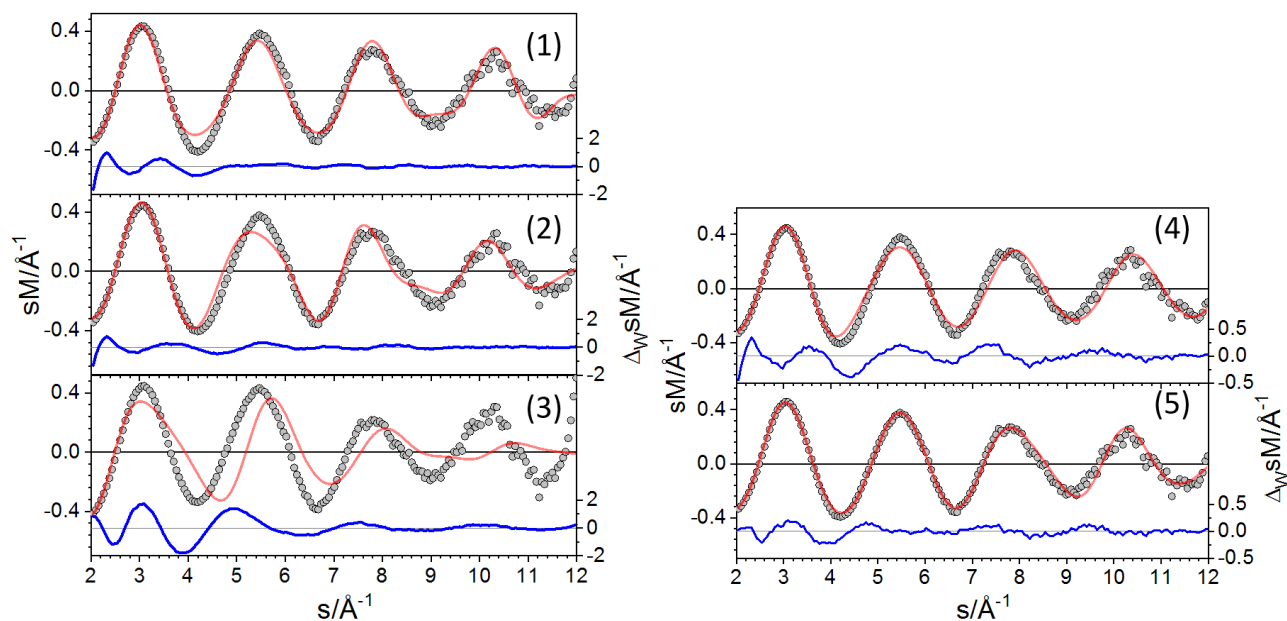
R_w value.

Figure 5.3: Comparison of experimental (gray open circles) and theoretical (red line) modified molecular scattering function of Pt$_7^-$ for isomers (1) - (5). The blue line shows the weighted deviation between experiment and theory.

Pt$_8^-$ Cluster

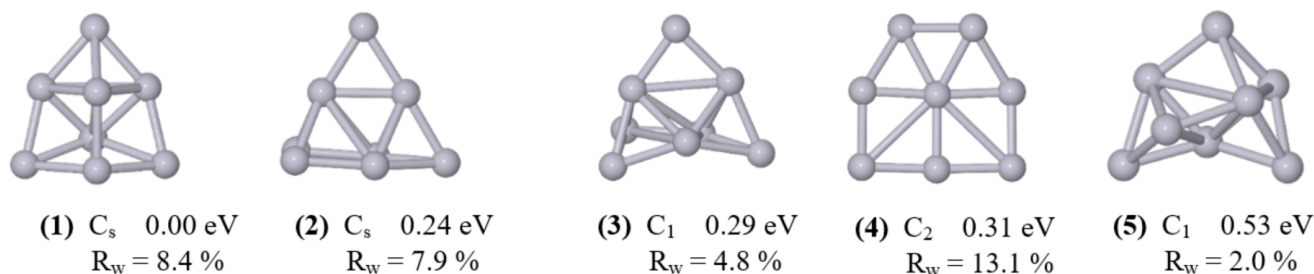| **(1)** C$_s$ 0.00 eV	**(2)** C$_s$ 0.24 eV	**(3)** C$_1$ 0.29 eV	**(4)** C$_2$ 0.31 eV	**(5)** C$_1$ 0.53 eV
R_w = 8.4 %	R_w = 7.9 %	R_w = 4.8 %	R_w = 13.1 %	R_w = 2.0 %

Figure 5.4: Lowest energy and best fitted to TIED isomers of Pt$_8^-$ with their corresponding PG symmetry, relative energy and R_w.

For Pt$_8^-$, a total of five isomers presented; the four lowest in energy and the one that best matches the measured data but is 0.53 eV above the putative GM, see Figure 5.4. The best energy structure (1) has a distorted heptagonal pyramid geometry with C_s symmetry and quartet spin multiplicity. A Similar structural motif has also been calculated as global minimum for neutral Pt$_8$ [40]. The next low-lying structure (2) is found to be +0.24 eV (+ 0.13 eV with SOC) high in energy. It has capped bridged-double triangle geometry with C_s PG and a doublet spin state. Structure (3) lies 0.29 eV (0.25 eV with SOC) above the best energy isomer (1) and found to be in quartet multiplicity. It is the development of isomer (4) of Pt$_7^-$ by adding just one atom at one side.The fourth low-lying isomer (4) has distorted heptagonal geometry with C_2 symmetry and a doublet spin multiplicity. It is the evolution of the third low energy structure (3) of Pt$_7^-$. It has relative energy of 0.31 eV (0.33 eV with SOC) above the GM
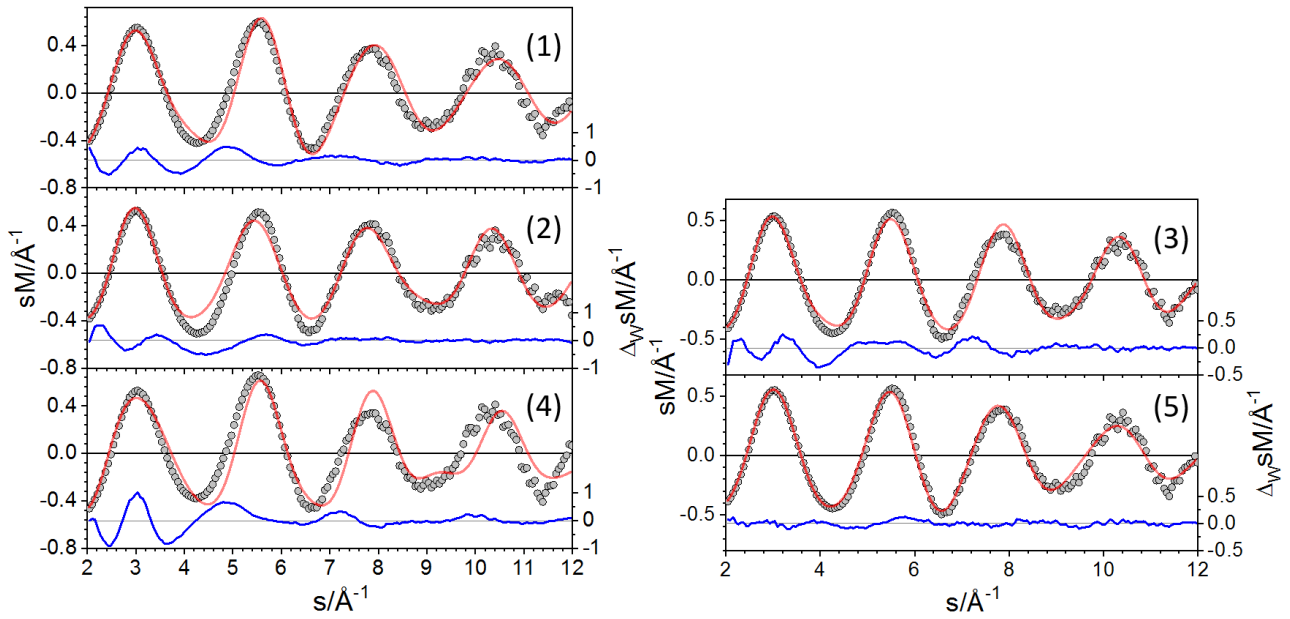
Figure 5.5: Comparison of experimental (gray open circles) and theoretical (red line) modified molecular scattering function of Pt_8^- for isomers (1) - (5). The blue line shows the weighted deviation between experiment and theory.

isomer (1). The last isomer presented is structure (5), which has slightly high energy +0.53 eV (+0.35 eV with SOC) but shows very good agreement to the measured data with $R_w = 2.0$ %. It is found to be a quartet spin state. It appears that this isomer is the evolution of Pt_7^- (5) and both of the isomers fit well to the TIED data. The TIED measured and the theory scattering agreement profile factor, R_w for the structures (1), (2), (3) and (4) are 8.4 %, 7.9 %, 4.8 %, and 13.1 %, respectively (see Figure 5.5). Hence, only structure (5) shows a good agreement with the TIED measurement. As already mentioned above, SOC has again minimizes the relative energy of isomer (5) from +0.53 eV to +0.35 eV, while RPA overestimates the energy difference between the GM and the other isomers, see Table 5.1.

Pt_9^- Cluster

(1) C_s 0.00 eV   **(2)** C_2 +0.15 eV   **(3)** C_1 +0.16 eV   **(4)** C_s +0.94 eV
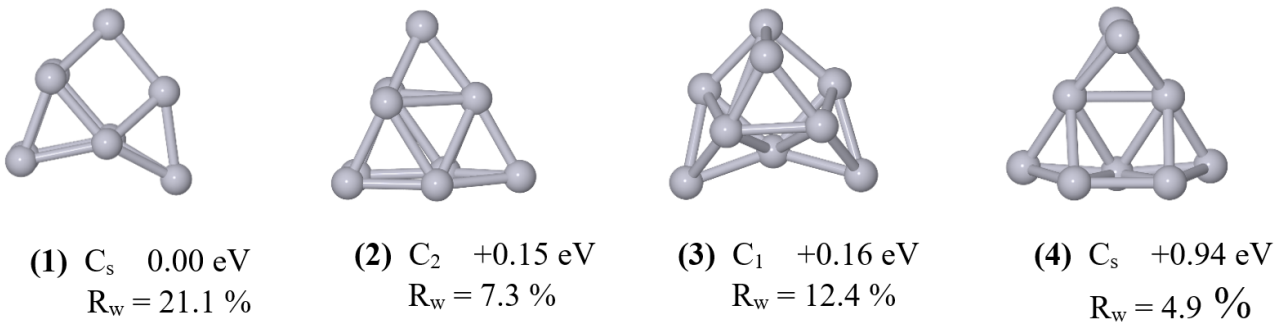$R_w = 21.1$ % $R_w = 7.3$ % $R_w = 12.4$ % $R_w = 4.9$ %

Figure 5.6: Lowest energy and best fitted to TIED isomers of Pt_9^- with their corresponding PG symmetry, relative energy and R_w.

Four isomers of Pt_9^- are illustrated in Figure 5.6. Of those, the first three are energetically most favorable and the last one matched better to the measurement. Without SOC the putative

GM isomer (1) is a dimer-capped pyramidal cage structure which was found in the doublet multiplicity and C_s symmetry. The next structure (2) is hexagonal-base trigonal pyramid (C_2) geometry with energy +0.15 eV (+0.02 eV with SOC). Without SOC structure (3) is the other energetically most favorable one with just 0.16 eV above structure (1), see Table 5.1. SOC
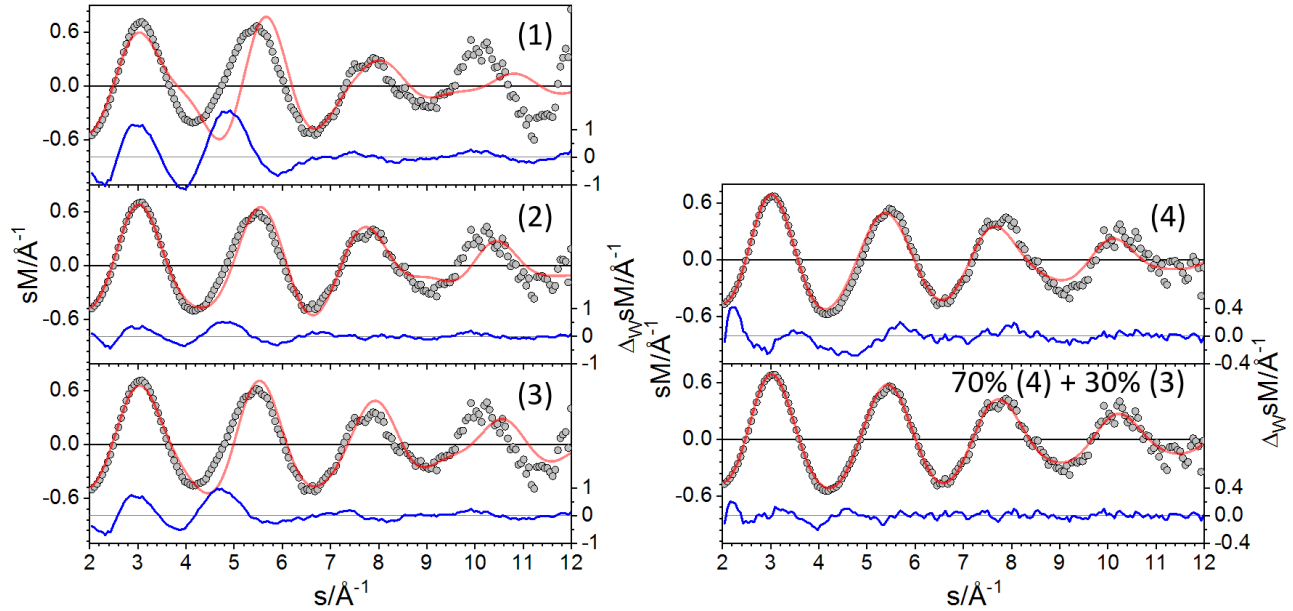

Figure 5.7: Comparison of experimental (gray open circles) and theoretical (red line) modified molecular scattering function of Pt_9^- for isomers (1) - (4) and a mixture of (3) and (4) in 30%/70% ratio. The blue line shows the weighted deviation between experiment and theory.

predicts structure (3) as GM followed by (2), (1) and (4), respectively. None of the isomers shows good agreement to the experimental data. However, structure (4) has $R_w = 4.8$ % which is still in agreement to some extent with the TIED data. If one takes a mixture of 70 % isomer (4) and 30 % isomer (3), the R_w value drops to 2.4 %, Figure 5.7. Consequently, this mixture of structure (4) and (3) is assigned for Pt_9^-. Interestingly, structure (3) seems to be the evolution of isomer (5) of Pt_8^-, which in turn was the evolution of isomer (5) of Pt_7^-.

Pt_{10}^- Cluster

(1) T_d 0.00 eV   **(2)** C_s 0.11 eV   **(3)** C_2 0.20 eV   **(4)** C_2 0.21 eV
     $R_w = 5.9$ % $R_w = 3.6$ % $R_w = 18.3$ % $R_w = 5.7$ %
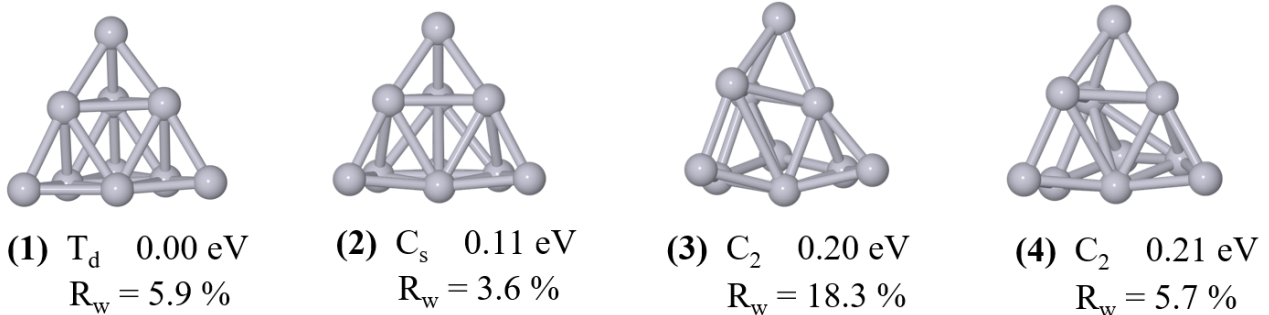
Figure 5.8: Lowest energy and best fitted to TIED isomers of Pt_{10}^- with their corresponding PG symmetry, relative energy and R_w.

Here, four low-lying very close energy structures are presented for Pt$_{10}^-$ (Figure 5.8 and Table 5.1). The putative global minimum structure (1) has fcc cut pyramidal geometry (T_d symmetry) with seven unpaired electrons. This structure has also been reported by Chaves et al. [44] as a global minimum structure and the same structural motif was also obtained for neutral and positively charged Pt$_{10}$. Three further energetically very similar structures (all within 0.22 eV above the GM) are distortions from the ideal symmetry. As shown in Figure 5.9, the best agreement to the TIED experiment is obtained for the distorted tetrahedral geometry (2) with R_w value of 3.6 % in C_s symmetry. In addition, the Gibbs free energy for structure (2) under the experimental condition is the lowest (see Table 5.1). The other structures are determined to have R_w value of larger than 5%. Thus, structure (2) can be assigned as main motif for Pt$_{10}^-$.
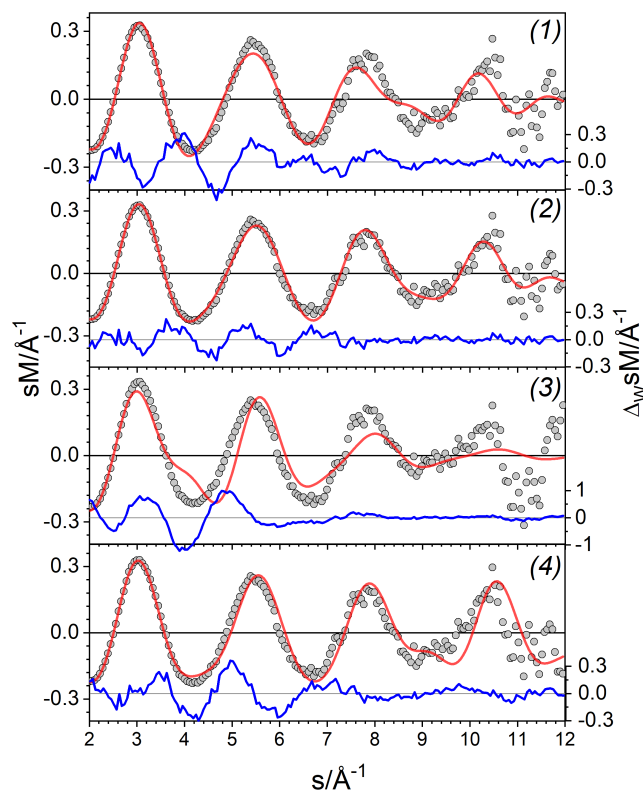

Figure 5.9: Comparison of experimental (gray open circles) and theoretical (red line) modified molecular scattering function of Pt$_{10}^-$ for isomers (1) - (4). The blue line shows the weighted deviation between experiment and theory.

Pt$_{11}^-$ Cluster

In Figure 5.10, the energetically favorable and the best fitted structures of Pt$_{11}^-$ are illustrated. The global minimum structure (1) in C_2 symmetry is a close packed base tetragonl pyramidal. The next low-lying isomer (2) is at energy of +0.07 eV (+0.14 eV with SOC) and has no symmetry. The side-capped fcc cut structure (3) in C_s symmetry was found at +0.32 eV (+0.16 eV with SOC). Essentially, this structure is the only isomer that fits to the TIED data with $R_w = 2.9$ %. It can be obtained from the best structure of Pt$_{10}^-$ by adding another atom
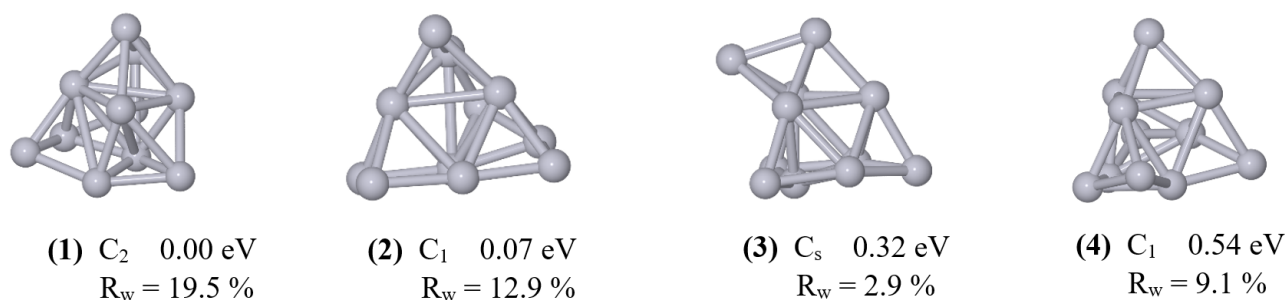
(1) C$_2$ 0.00 eV
R$_w$ = 19.5 %

(2) C$_1$ 0.07 eV
R$_w$ = 12.9 %

(3) C$_s$ 0.32 eV
R$_w$ = 2.9 %

(4) C$_1$ 0.54 eV
R$_w$ = 9.1 %

Figure 5.10: Lowest energy and best fitted to TIED isomers of Pt$_{11}^-$ with their corresponding PG symmetry, relative energy and R$_w$.
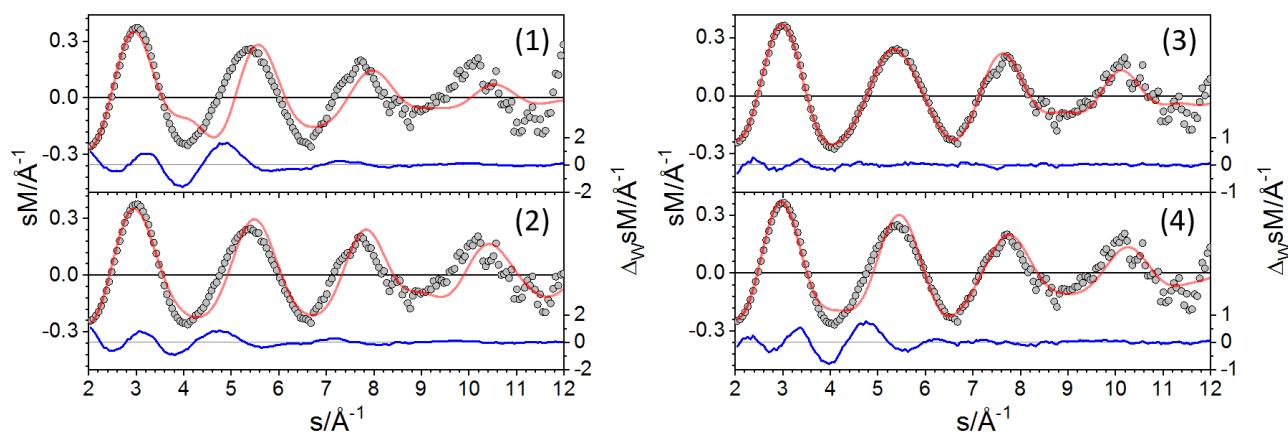

Figure 5.11: Comparison of experimental (gray open circles) and theoretical (red line) modified molecular scattering function of Pt$_{11}^-$ for isomers (1) - (4). The blue line shows the weighted deviation between experiment and theory.

in the center of a Pt triangle next to one edge of the pyramid. The other isomer (4) lies 0.54 eV (0.36 eV with SOC) above the global minimum and has R$_w$ = 9.1 %. All the isomers were found in doublet spin multiplicity. As evidenced by analyzing the profile factor R$_w$ of the theoretical and experimental scattering function (Table 5.1 and Figure 5.11) all isomers except isomer (3) are far from the acceptable agreement and can be ruled out. Thus, isomer (3) is assigned as the main motif for Pt$_{11}^-$.

Pt$_{12}^-$ Cluster

(1) C$_1$ 0.00 eV
R$_w$ = 26.0 %

(2) C$_s$ 0.14 eV
R$_w$ = 15.5 %

(3) C$_1$ 0.34 eV
R$_w$ = 6.8 %
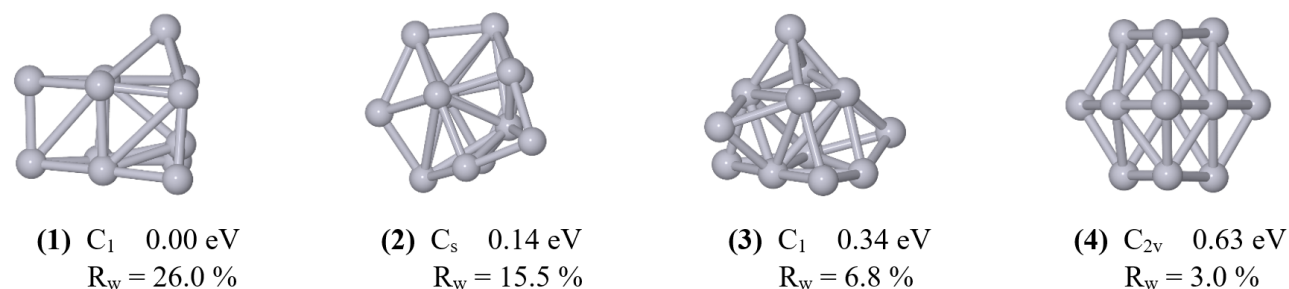
(4) C$_{2v}$ 0.63 eV
R$_w$ = 3.0 %

Figure 5.12: Lowest energy and best fitted to TIED isomers of Pt$_{12}^-$ with their corresponding PG symmetry, relative energy and R$_w$.

The low energy and low R_w structures of Pt$_{12}^-$ are depicted in Figure 5.12. All of these structures are 3D and lie within 0.25 eV relative energy at SOC corrected TPSS level (Table 5.1). Even though structure (1) is energetically favorable, it was verified to have a fitting profile of
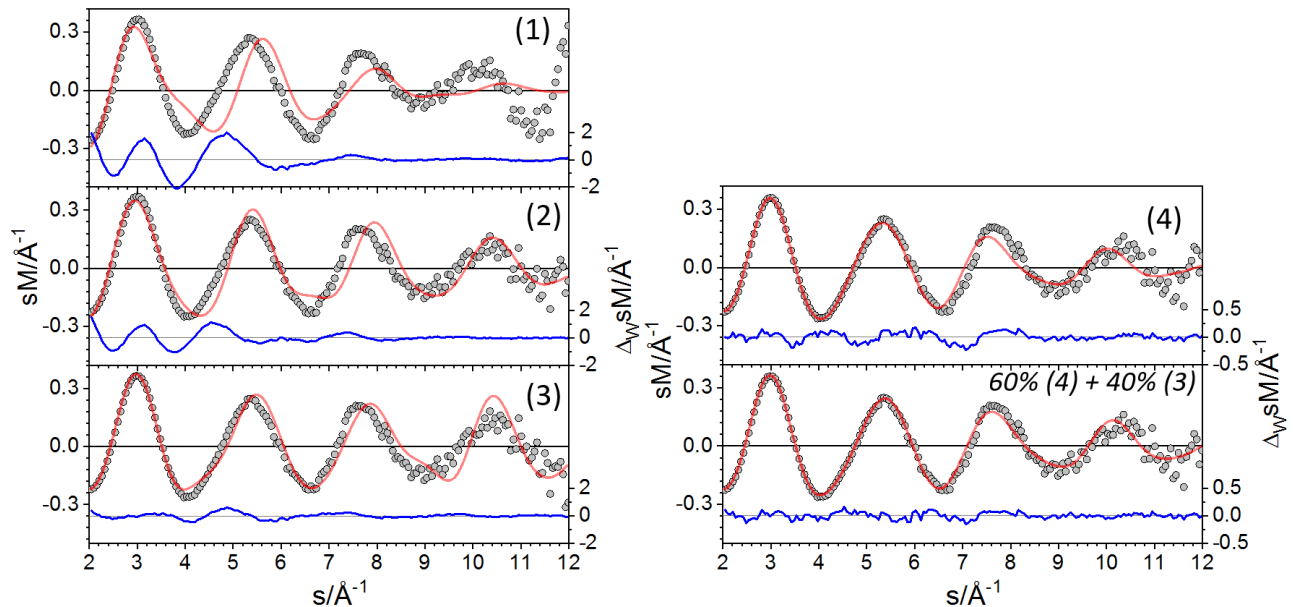

Figure 5.13: Comparison of experimental (gray open circles) and theoretical (red line) modified molecular scattering function of Pt$_{12}^-$ for isomers (1) - (4) and a mixture of (3) and (4) in 40%/60%. The blue line shows the weighted deviation between experiment and theory.

R_w = 26.0 %. Analogously, higher R_w values of isomers (2) and (3) have confirmed that they are not in a good agreement with TIED data. The best agreement between simulated and experimental scattering functions was found for isomer (4), C_{2v} symmetry with R_w = 3.0 % (Figure 5.13). Thus, the probed R_w values has led to the conclusion that hcp cut isomer (4) is a potential candidate for being a main motif, however, SOC corrected TPSS shows that it is 0.18 eV above the isomer (1). On the other hand, a mixture of isomer (3) and isomer (4) in 40%/60% ratio provided R_w value of 2.1%. Consequently, this mixture structure with a dominant part from isomer (4) can be assumed for Pt$_{12}^-$. The spin state of isomers (1), (2) and (3) are doublet, while isomer (4) is in octet multiplicity.

Pt$_{13}^-$ Cluster

For Pt$_{13}^-$, unlike the other sizes studied here the calculated energetically favorable structures have a large difference from the putative GM isomer (Figure 5.14). However, these difference significantly decreased after the SOC correction, see Table 5.1. The first low energy isomer (1) (C_s symmetry) is far from agreement to the TIED measurement with an R_w profile of 25.6 %. The next low-lying capped cage-like isomer (2) is +0.36 eV (+0.32 eV with SOC) above isomer (1). Similarly, isomer (2) has a high profile factor (R_w = 11.2 %). The next two isomers (3) and (4) have energies of +0.46 eV and +0.61 eV at TPSS, which decreases to +0.141 and +0.145 eV after inclusion of SOC. Thus, SOC predicts these two isomers as iso-energetic and one can see that they have similar structural motifs with a slight deviation. More importantly, isomers

(3) and (4) are structurally related to isomer (4) of Pt_{12}^-, that has shown to have the best R_w of all other isomers. These two isomers are in line with the experimental data with R_w value of 5.4 % for isomer (3) and 4.1 % for isomer (4), see Figure 5.15. Therefore, based on the R_w it seems that the compact structure (4), C_{3v} symmetry is the preferred one and can be assigned as main motif for Pt_{13}^-.

(1) C_s 0.00 eV
$R_w = 25.6$ %

(2) C_1 +0.36 eV
$R_w = 11.2$ %

(3) C_1 +0.46 eV
$R_w = 5.4$ %

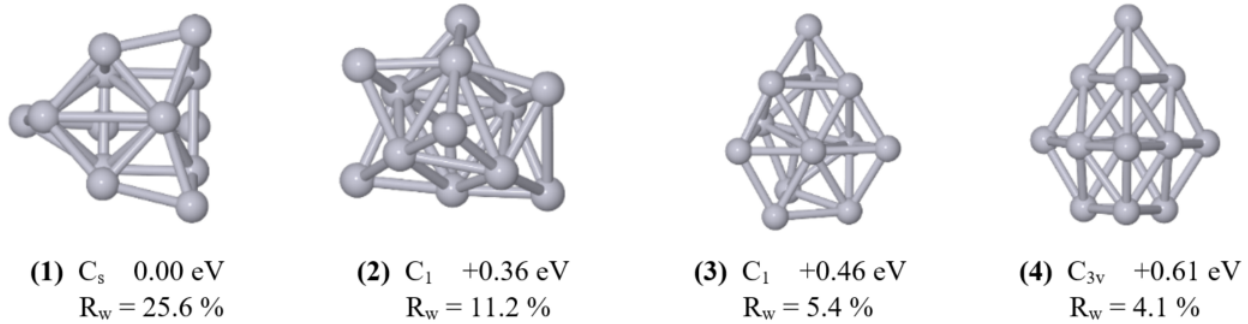**(4)** C_{3v} +0.61 eV
$R_w = 4.1$ %

Figure 5.14: Lowest energy and best fitted to TIED isomers of Pt_{13}^- with their corresponding PG symmetry, relative energy and R_w.
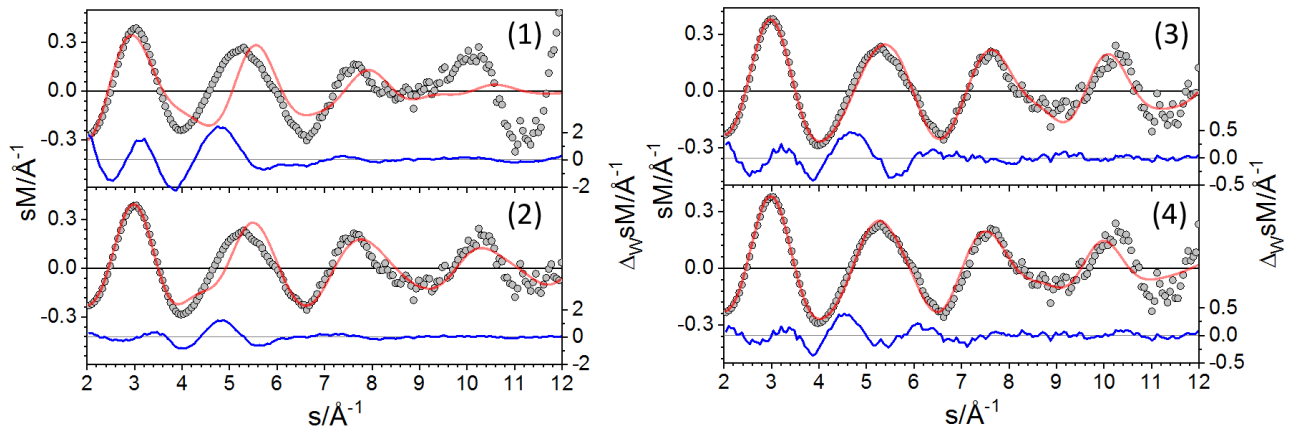

Figure 5.15: Comparison of experimental (gray open circles) and theoretical (red line) modified molecular scattering function of Pt_{13}^- for isomers (1) - (4). The blue line shows the weighted deviation between experiment and theory.

5.1.1 Other energetic properties

Cohesive Energies and second order difference

The relative energy stability of different cluster sizes can be described by the cohesive energy (Eq. 3.14) and second order difference (SOD) (Eq. 3.15). The cohesive energies of the lowest-energy (putative GM) and best fitted clusters have been calculated at PBE, TPSS and TPSSH level and the results are summarized in Figure 5.16. As expected, the cohesive energy increases almost monotonically with size for all functionals and as size of cluster increases it is expected to reach the bulk value of 5.84 eV [93]. In general, TPSS functional shows a bit higher cohesive energy (better stability) and fits better to experimental scattering compared to PBE and TPSSH.
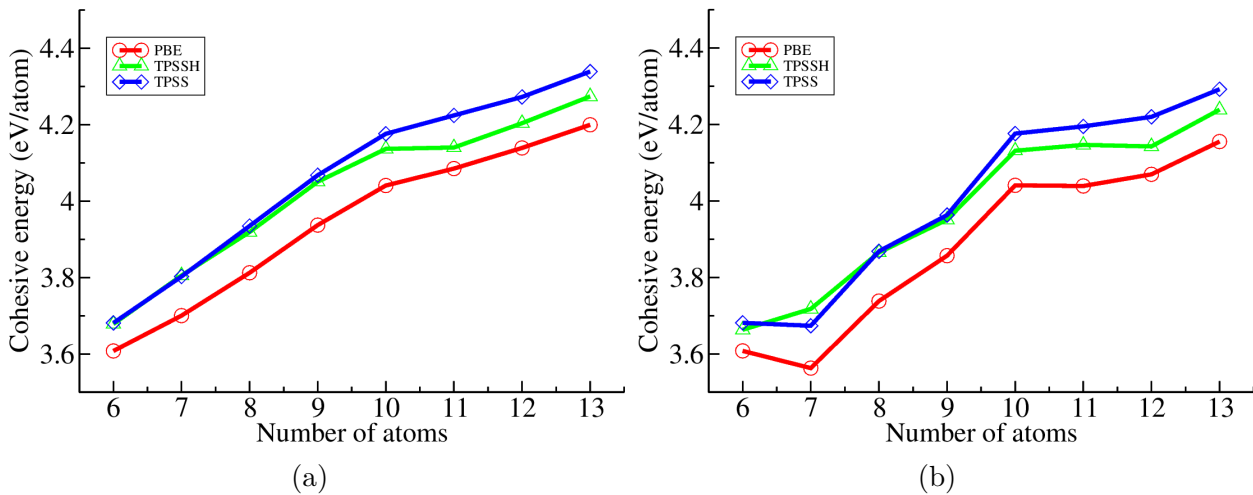
Figure 5.16: Cohesive energy (a) for lowest-energy structure and (b) the best fitted structure with the measurement
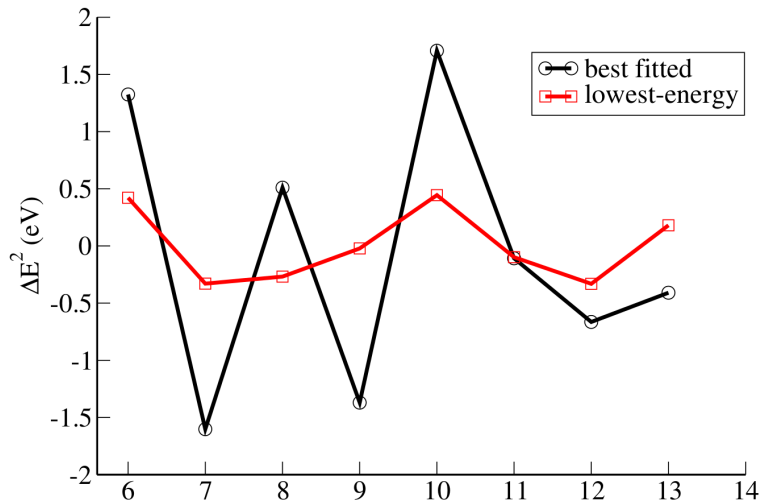

Figure 5.17: The second order difference relative stability (ΔE^2) of Pt$_n^-$ as a function of number of atoms (n) in the clusters.

The second order difference (SOD) has been also calculated at TPSS level and shows better elucidation of the relative energy difference, see Figure 5.17. The best fitted structures (black line) indicates even-odd oscillations up to size n = 11, in which even numbers are more stable. A significant stability peaks observed at size n = 6 and n = 10, but it is even more substantial for the latter. This extra stability also observed slightly from cohesive energy, see Figure 5.16. A similar finding were reported by Chaves et al. [44], in which as clearly pointed out regardless of charge states Pt$_6$ and Pt$_{10}$ shows higher stability and rationalized by correlating to high sd hybridization. Most importantly, unlike other sizes, the putative global minimum structural motif of Pt$_6$ and Pt$_{10}$ remains the same regardless of charge state (+/-/neutral) [44]. As already indicated by previous work [43], we can conclude that Pt$_6^-$ and Pt$_{10}^-$ are magic clusters. Finally, to stress the above, these magic structures are the DFT global minimum and fits remarkably with the TIED measurement data.

5.1.2 Other structural properties

Average bond length

The average bond length of the global minimum and the best fitted structures for each size are calculated at TPSS level and presented in Figure 5.18. Here, the average bond length defined as:

$$d_{av} = \frac{1}{n_b} \sum_{ij} d_{ij} \tag{5.1}$$

where d_{ij} is the distance between the two atoms i and j with a cut off 300 pm which is 8.3 % greater than the bulk value of 277 pm [93]. N_b is the number bonds between atoms that lie below the cutoff. As can be seen, from the plot average bond length lies between 254 pm to
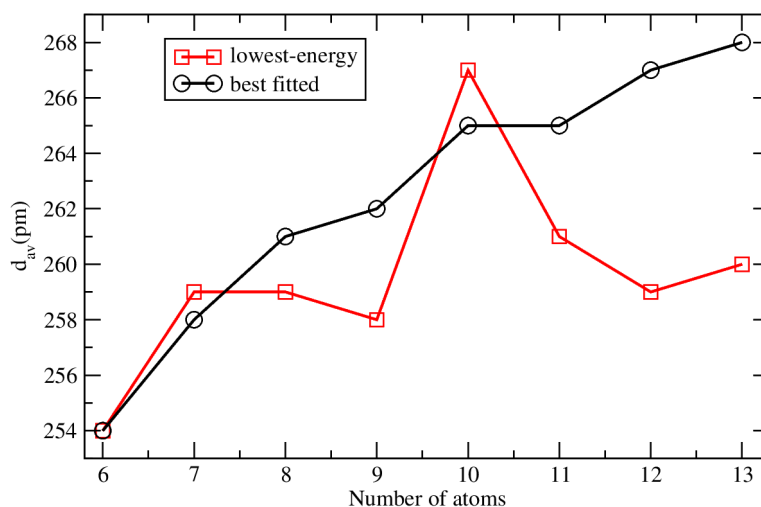

Figure 5.18: Average bond length (d_{av}) of Pt$_n^-$ clusters for TPSS lowest energy structures (red line) and best TIED fitted structures (black line.

268 pm. The planar structure of Pt$_6^-$ shows relatively short average bond length. For the best fitted structures, the average bond length increases monotonically with the size of the clusters, but still far from the bulk value of 277 pm [93]. Nevertheless, the lowest energy structures have not shown systematic changes.

Root mean square deviation (RMSD)

The structural pair-wise RMSD differences between isomer structures of the same cluster size for the structures presented above are summarized in Table 5.2. If two structures are similar geometrically, they should have a small RMSD value. If the two compared structures are the same, then the RMSD value should be zero. Different RMSD value can be determined, depending on the degree of geometrical similarity between two isomer structures. For example, the RMSD difference of structures Pt$_6^-$ (2) and Pt$_6^-$ (3) with respect to the Pt$_6^-$ (1) is 0.32 and 2.42 Å, respectively. The RMSD value implies that structure Pt$_6^-$ (2) is more similar to Pt$_6^-$ (1) than structure Pt$_6^-$ (3). Visually inspecting the spatial structure of the three isomers as shown in Figure 5.1 supports the RMSD based finding. The same explanation holds true for the RMSD value of the other sizes.

Table 5.2: Calculated structural pair-wise root mean square deviation (RMSD) in (Å) between isomer structures of each size. The numbering given to different isomers are according to Figures 5.1, 5.2, 5.4,5.6, 5.8, 5.10, 5.12 and 5.14.

	Pt$_6^-$ (1)	Pt$_6^-$ (2)	Pt$_6^-$ (3)		
Pt$_6^-$ (1)	0.00	0.32	2.24		
Pt$_6^-$ (2)	0.32	0.00	2.12		
Pt$_6^-$ (3)	2.42	2.12	0.00		
	Pt$_7^-$ (1)	Pt$_7^-$ (2)	Pt$_7^-$ (3)	Pt$_7^-$ (4)	Pt$_7^-$ (5)
Pt$_7^-$ (1)	0.00	2.68	2.43	1.69	2.28
Pt$_7^-$ (2)	2.68	0.00	2.37	2.69	2.49
Pt$_7^-$ (3)	2.43	2.37	0.00	2.46	2.43
Pt$_7^-$ (4)	1.69	2.69	2.46	0.00	2.01
Pt$_7^-$ (5)	2.28	2.49	2.43	2.01	0.00
	Pt$_8^-$ (1)	Pt$_8^-$ (2)	Pt$_8^-$ (3)	Pt$_8^-$ (4)	Pt$_8^-$ (5)
Pt$_8^-$ (1)	0.00	2.23	2.44	2.03	2.10
Pt$_8^-$ (2)	2.23	0.00	0.31	2.38	2.22
Pt$_8^-$ (3)	2.44	0.31	0.00	2.61	2.15
Pt$_8^-$ (4)	2.03	2.38	2.61	0.00	2.41
Pt$_8^-$ (5)	2.10	2.22	2.15	2.41	0.00
	Pt$_9^-$ (1)	Pt$_9^-$ (2)	Pt$_9^-$ (3)	Pt$_9^-$ (4)	
Pt$_9^-$ (1)	0.00	1.95	1.90	2.12	
Pt$_9^-$ (2)	1.95	0.00	2.50	1.83	
Pt$_9^-$ (3)	1.90	2.50	0.00	2.34	
Pt$_9^-$ (4)	2.12	1.83	2.34	0.00	
	Pt$_{10}^-$ (1)	Pt$_{10}^-$ (2)	Pt$_{10}^-$ (3)	Pt$_{10}^-$ (4)	
Pt$_{10}^-$ (1)	0.00	2.48	2.56	2.60	
Pt$_{10}^-$ (2)	2.48	0.00	2.91	2.53	
Pt$_{10}^-$ (3)	2.56	2.91	0.00	2.49	
Pt$_{10}^-$ (4)	2.60	2.53	2.49	0.00	
	Pt$_{11}^-$ (1)	Pt$_{11}^-$ (2)	Pt$_{11}^-$ (3)	Pt$_{11}^-$ (4)	
Pt$_{11}^-$ (1)	0.00	3.01	2.63	3.00	
Pt$_{11}^-$ (2)	3.01	0.00	2.64	2.74	
Pt$_{11}^-$ (3)	2.63	2.64	0.00	2.79	
Pt$_{11}^-$ (4)	3.00	2.74	2.79	0.00	
	Pt$_{12}^-$ (1)	Pt$_{12}^-$ (2)	Pt$_{12}^-$ (3)	Pt$_{12}^-$ (4)	
Pt$_{12}^-$ (1)	0.00	3.09	3.05	2.70	
Pt$_{12}^-$ (2)	3.09	0.00	2.47	3.07	
Pt$_{12}^-$ (3)	3.05	2.47	0.00	2.45	
Pt$_{12}^-$ (4)	3.70	3.07	2.45	0.00	
	Pt$_{13}^-$ (1)	Pt$_{13}^-$ (2)	Pt$_{13}^-$ (3)	Pt$_{13}^-$ (4)	
Pt$_{13}^-$ (1)	0.00	2.88	3.26	3.22	
Pt$_{13}^-$ (2)	2.88	0.00	3.00	3.15	
Pt$_{13}^-$ (3)	3.26	3.00	0.00	2.30	
Pt$_{13}^-$ (4)	3.22	3.15	2.30	0.00	

5.1.3 Electronic properties

HOMO-LUMO gap (E_g)

The energy gap between the highest occupied molecular orbital (HOMO) and the lowest unoc-
cupied molecular orbital (LUMO) for the lowest energy isomers and best fitted structures with
the TIED measurement has been calculated for each cluster size. It is known that the transi-
tion from the atomic scale to the bulk metallic behavior is accompanied by the closure of the
HOMO-LUMO gap. It is because the molecular orbitals are formed from the overlap of more
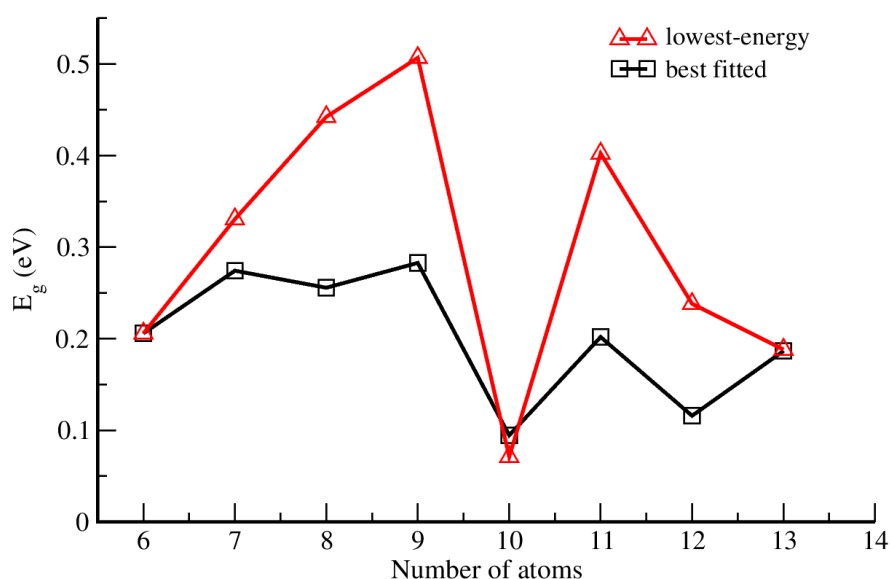and more atomic orbitals, and thus, the energy levels progressively come closer. The higher

Figure 5.19: HOMO-LUMO gap (E_g) of Pt$_n^-$ clusters for TPSS lowest energy structures (red
line) and best TIED fitted structures (black line).

HOMO-LUMO gap has also been associated with high chemical stability and low reactivity.
Figure 5.19, shows the variation of E_g (eV) with cluster size. As can be seen in the plot, in all
cases the E_g are found between 0.07 to 0.5 eV, hence, one can infer that even the small anionic
Pt clusters show metallic behavior. For cluster sizes in which the GM is not the best fitted to
the TIED, the E_g are found to be slightly low, see Figure 5.19 (black line). Moreover, it turns
out to be difficult to make a relationship between E_g and the stability of the structures as size
increases. Again, it is noteworthy to point out that HOMO-LUMO gap of Pt$_6^-$ and Pt$_{10}^-$ are
slightly lower in comparison to their next neighbor size.

Density of states

The density of states can provide detailed information of the electronic structures. The s-, p-,
d-projected partial DOS for the most stable and the best TIED fitting isomers of each size of
Pt$_n^{-1}$ (n = 6-13) clusters are plotted in Figures 5.20. The density of states are obtained using
the Turbomole dosper module with Gaussian broadening. The energy (hartree) emin = -0.5

and emax = 0.14 with width = 0.007 is used. For the purpose of comparison, the bulk Pt partial DOS is also given. Here, only the energy states close to frontier molecular orbitals, i.e., HOMO and LUMO levels are illustrated as they have dominant influence on the reactivity and optical properties. The energy levels for s, p, and d peaks are distinctly separated. As shown from the bulk and Pt$_6^-$ DOS plot, the main contributor for the total DOS is the d-projected DOS. However, the contribution of s- and p-projected DOS is also not negligible in the whole energy states. The hybridization of s, p and d states is significant to the vicinity of Fermi level. The valence bands are basically formed by the overlaps of the 5d and 6s atomic orbitals. Inspecting the plots, similar partial DOS is observed for isomer structures of different sizes, except for hcp-like structures of Pt$_{12}^-$ and Pt$_{13}^-$. Therefore, the DOS plot might not help to differentiate isomer structures.
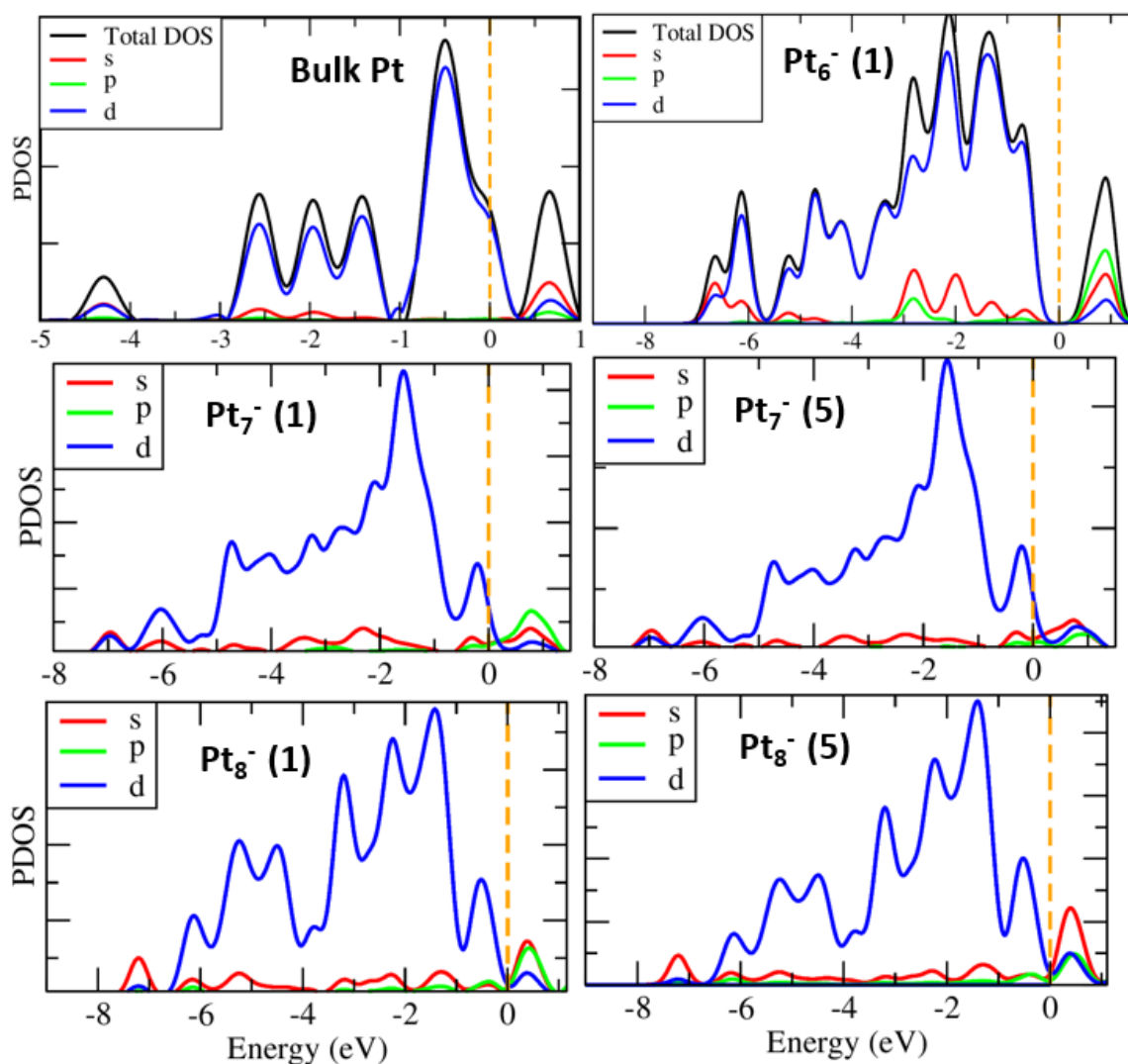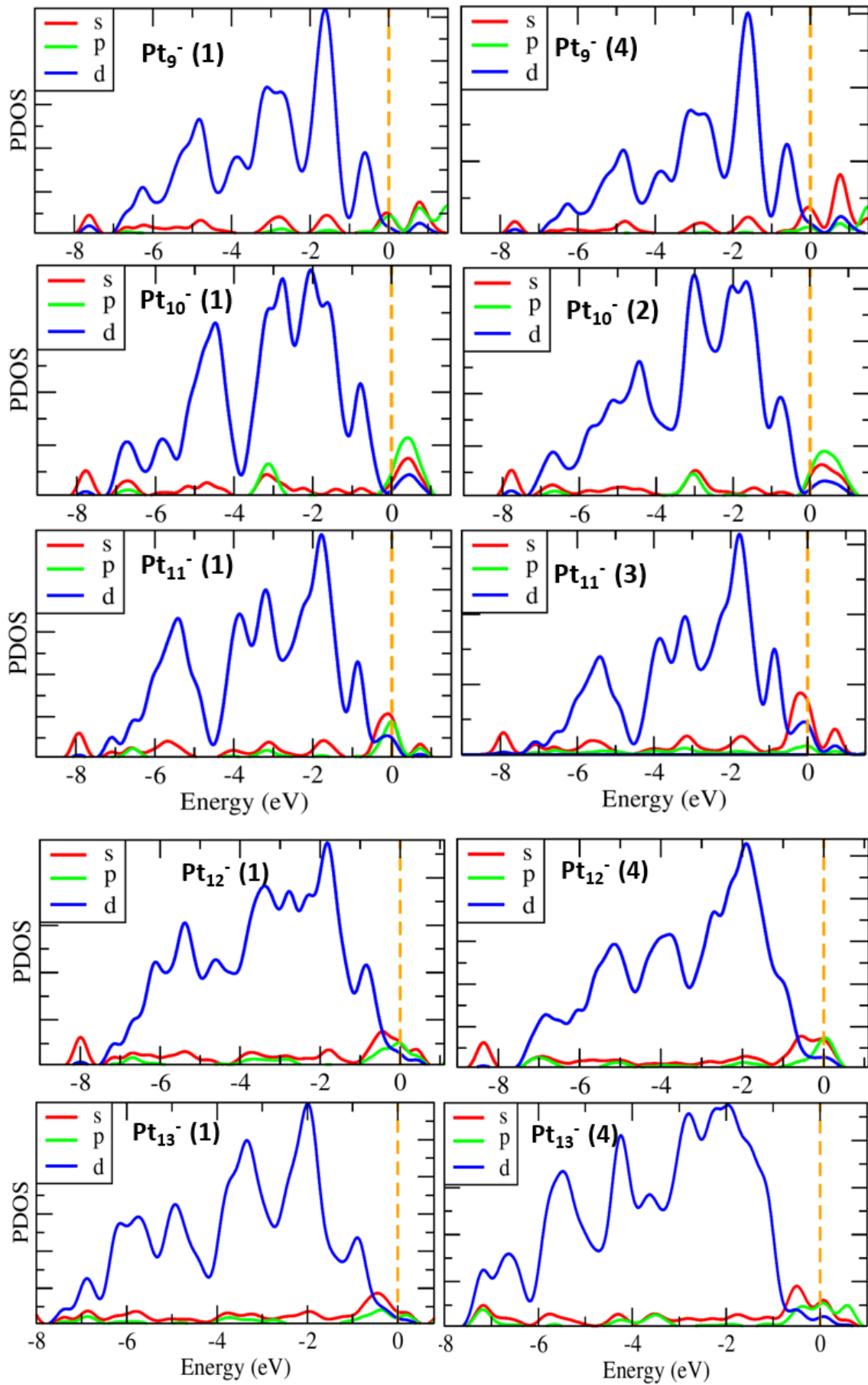
Figure 5.20: The s-, p-, d-projected partial density of states and total density of states for the lowest energy structures and the best TIED fitting structures of Pt$_n^{-1}$ clusters. Note the PDOS (y-axis) scaling can be different for the different structures.

5.1.4 Vibrational Spectra

The structural information of the clusters can also be obtained from the calculated IR spectra, which would directly be compared to the experimental vibrational spectroscopy data. In Figures 5.21 and 5.22, the calculated vibrational spectra of the Pt$_n^{-1}$ (n = 6-13) clusters are presented. As it can be seen, it is clear that the calculated spectra of both the ground state and the close-lying state are different. However, there can be some IR peak degeneracy due to structural similarity. For example, this has happened to the prominent peaks (at 235 cm^{-1}) of Pt$_6^-$ (1) and Pt$_6^-$ (2) isomer structures since they have structural resemblance. For all the structures, the frequency range is shown from 110 to 310 cm^{-1}, as no significant intensities were found beyond this range. The prominent peaks in all cases is found in the range $196 - 240$ cm^{-1}. The IR spectra of most of the clusters appear with two or more intense peaks, this is especially more visibly seen for larger cluster sizes. Nevertheless, as it might be expected symmetric structures of Pt$_6^-$ (1), Pt$_7^-$ (1), Pt$_7^-$ (2), Pt$_{10}^-$ (1), Pt$_{10}^-$ (2), Pt$_{12}^-$ (4) and Pt$_{13}^-$ (4) have shown one intense peak. To my knowledge, no experimental IR data have actually been available to make comparisons for the negatively charged Pt clusters. However, the calculated IR spectra reported here can be used in the future for comparison with experimental measurement.

Figure 5.21: IR frequencies (cm^{-1}) for Pt$_n^-$ the structures presented in Figures 5.1, 5.2 and 5.4. The unit of the intensity is km/mol. The IR spectra are calculated at TPSS/def2-TZVP level with vibrational scaling factor of 1.0. Note the intensity scaling can be different for the different structures.
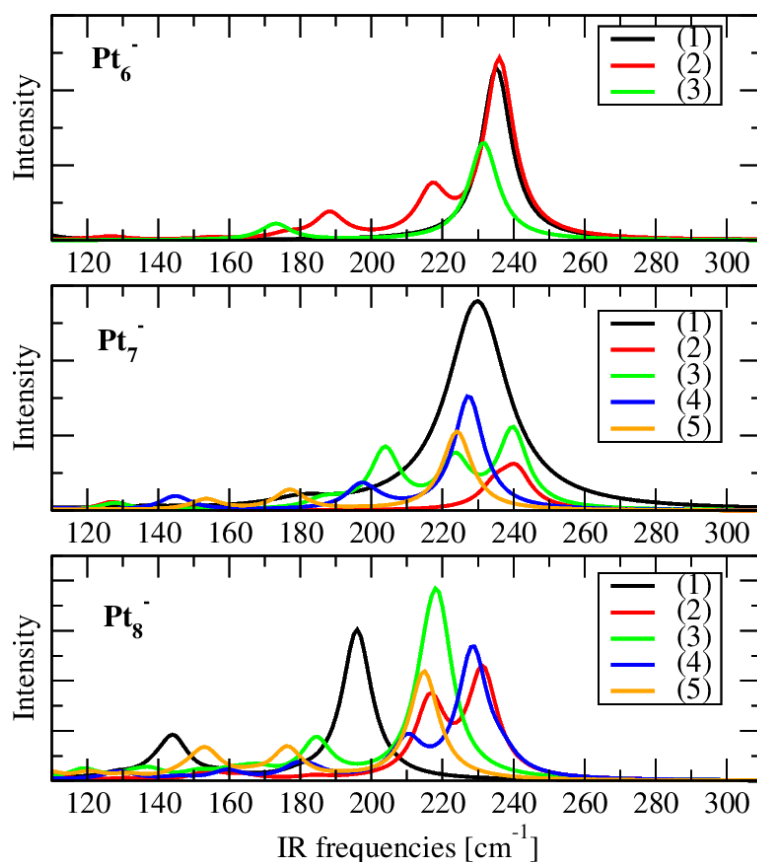
Figure 5.22: IR frequencies (cm^{-1}) for Pt_n^- the structures presented in Figures 5.6, 5.8, 5.10, 5.12 and 5.14. The unit of the intensity is km/mol. The IR spectra are calculated at TPSS/def2-TZVP level with vibrational scaling factor of 1.0. Note the intensity scaling can be different for the different structures.
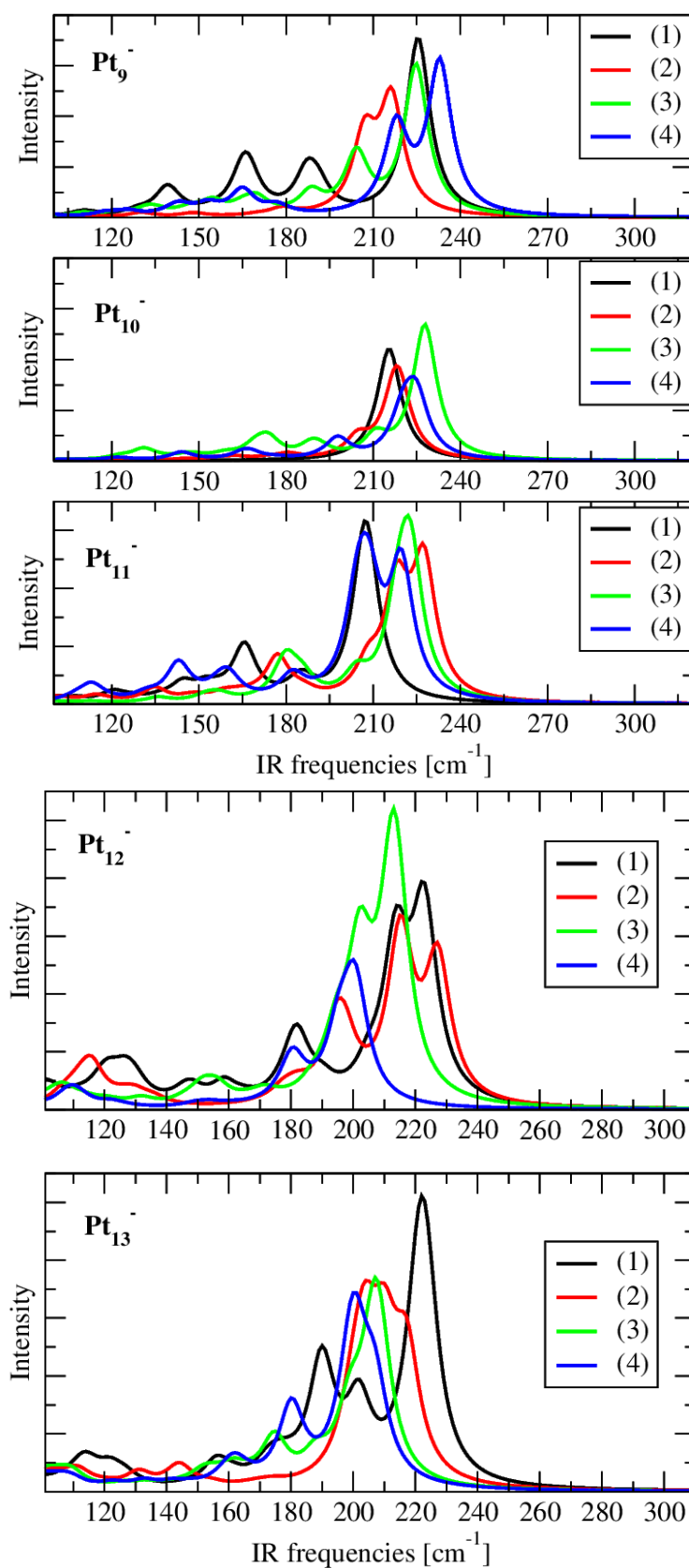
5.2   Conclusions

Structures of small platinum anions Pt_n^- (n = 6 - 13), have been assigned by combining DFT coupled genetic algorithm global optimization method and the results of trapped ion electron diffraction measurements. Best fitting structures correspond either to the putative global minimum isomers or to energetically close-lying isomers. The best theory and experiment agreed structures are given in Figure 5.23. As evidenced from the assigned structures, there were sizes
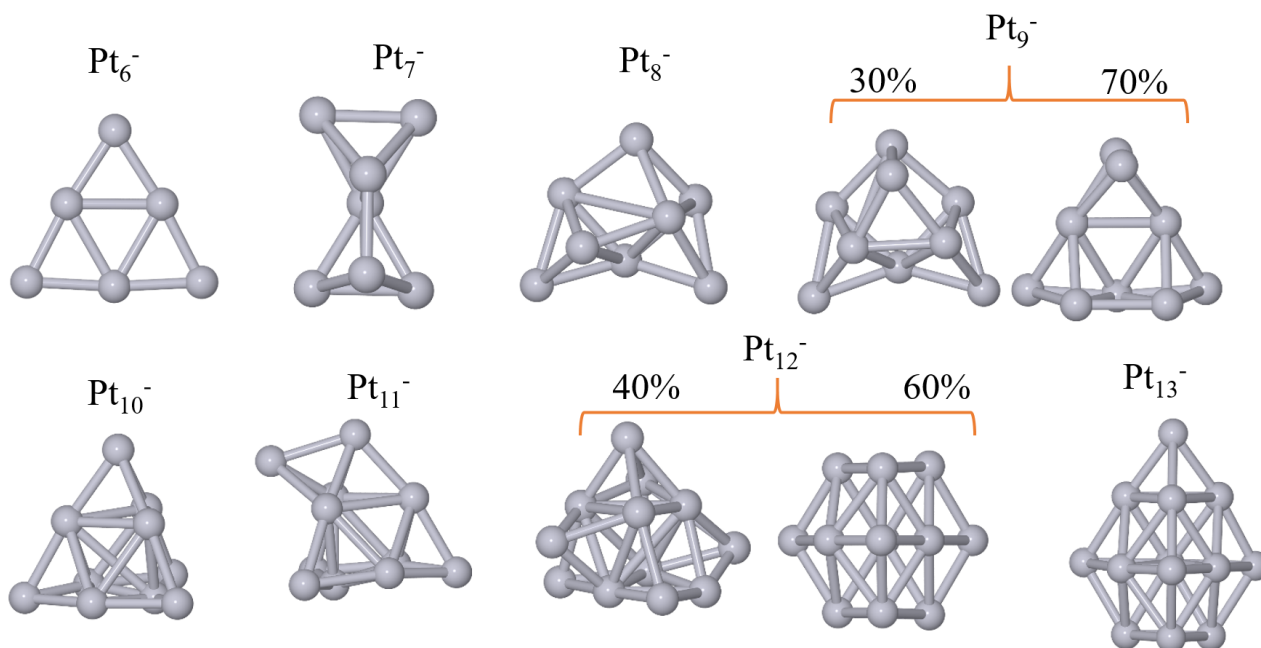

Figure 5.23: The assigned structures for each size based on the theory and TIED measured data. For Pt_9^- and Pt_{12}^- a mixture of two structures assumed with one of the structures is dominant motif.

evolution from Pt_7^- to Pt_9^-, from Pt_{10}^- to Pt_{11}^- and from Pt_{12}^- to Pt_{13}^-. Among the structures studied, Pt_6^- and Pt_{10}^- show high stability and Pt_6^- is the only planar motif. Correction of DFT energies with the thermodynamic Gibbs free energy calculation at experimental condition (95 K and 1 mbar) did not change the relative energy ordering. For all structures the average bond length found in the range between 245–268 pm. Small HOMO-LUMO gap between 0.07 and 0.5 was calculated. DFT correction calculations (SOC, RPA and dispersion correction) were carried out. As a result, it was determined that SOC decreases significantly the relative energy of isomers compared to the pure TPSS functional, sometimes up to 0.4 eV. In addition, the relative energy ordering remains the same as TPSS with exception of Pt_7^-, Pt_9^- and Pt_{10}^-, in which the ordering is also changed. Furthermore, the influence of dispersion correction were determined to be insignificant. On the other hand, the effect of RPA calculation on relative energy is not clear. Thus, it is difficult to draw a conclusion on RPA influence to the relative energy of the clusters. In general, compact and symmetric structures are obtained for Pt_{10}^-, Pt_{12}^- and Pt_{13}^- as putative global minimum motif. Pt_6^- and Pt_{10}^- shows better stability and good

fitting with the experiment than the other sizes. It is non-trivial to determine the low energy structures as the number of isomers separated by only a few eV. The inclusion of spin-orbit effect treatment is very important for energetic properties. The only planar structure among the studied is Pt_6^-. Pt_{12}^- and Pt_{13}^- seems to be hcp cut and they might be a starting point of transition to fcc crystal packing. Moreover, the calculated vibrational spectra for all the structures presented in this work are provided, which can be applicable for comparison with experimental measurements.

Part II

Chapter 6

Introduction to Adsorption studies

The description of the interaction of molecules and atoms with surfaces of metals is the essential basis for understanding of surface chemical reactivity and catalysis. It is well known that all surface chemical reactions involve some elementary reaction steps between reactants and products. When a chemical reaction takes place on the catalyst surface, the first step is usually atomic and molecular adsorption. The catalytic activity of a solid surface is related to the energies of the adsorbed intermediates and transition states. Most importantly, with these energies of surface chemical events it is possible to determine reactivity and selectivity of the surface towards a certain chemical reaction [94]. Medford et al. [95] have used DFT calculated adsorption energies to create scaling relations between bond energies and reaction barriers, which also enables to generate the so-called volcano plots based on the Sabatier principle [96, 97]. In this way it is possible to make predictions of activity of a catalyst for a particular reaction. In addition, adsorption energies can be used to build micro-kinetic models in heterogeneous catalysis [94]. In case of nanocatalysts, the presence of abundant active sites and type of adsorption sites can have a large effect on reaction rates and selectivity [98]. Thus, it is of great importance to calculate the energies of adsorbed reaction intermediates and transition states on nanoparticle surfaces.

6.1 CO adsorption on transition metal surfaces

The adsorption of carbon monoxide (CO) on transition metal surfaces is often considered as a prototype model that provides description for many other interesting and practically relevant adsorption processes. In the past decades, CO adsorption on transition metallic surfaces has been the subject of many experimental and theoretical studies [9]. The interest for CO adsorption mainly arises from its importance in oxidation catalysis, especially in car exhaust gas converter [2]. Moreover, understanding the adsorption mechanism of CO on metal surface can provide helpful information about the behavior of other industrially important carbonyl and complex molecular adsorbates that have similar bonding behavior. Experimentally, vibrational spectroscopy is applied to monitor the adsorption site where CO is bind at the metal surface. In particular, the experimental determination of the most stable adsorption site of CO on the surface of transition metals by employing infrared spectroscopy is straightforward. Among the

experimental techniques, diffuse reflection infrared Fourier transform spectroscopy (DRIFTS) and high resolution electron energy loss spectroscopy (HREELS) are the most commonly used measurements [99]. Nowadays, in situ DRIFTS enables to achieve highly resolved adsorption spectral data, which allow to differentiate the various possible adsorption sites. This is based on the fact that, the CO stretching mode is highly sensitive to the adsorption site where CO binds and is very different for the on-top, bridge and three-fold sites. The reason for different stretching modes is due to the dynamic dipole moment of CO at various adsorption sites which give rise to change in internal stretching mode [99]. In general, for CO adsorption on Pt and Pd metal surfaces broadly the following range of frequencies have been measured; on-top bonded 2000-2100 cm^{-1}, bridge bonded 1850-1970 cm^{-1}, and three-fold hollow bonded below 1850 cm^{-1} [100–104]. For the interest of determining the correlation of CO adsorption behavior with coordination numbers of the atom sites, particle size and coverage, several studies have been reported based on CO vibrational frequencies at Pt nanoparticles. To exemplify, at both low and high coverage, a linear correlation of the wave number of on-top bonded CO with the coordination number of the platinum atoms was found [105, 106]. In addition, regardless of coverage a wavenumber range of 2050-2100 cm^{-1} is observed for platinum with coordination numbers from 6 to 9. For a particle size distribution between 0.5 and 5 nm, Maillard et al. have studied size and site effect at various coverage [107]. At CO saturation coverages a band at 2036 cm^{-1} was assigned to nanoparticles with an average diameter of 1.7 nm and 2054 cm^{-1} to those of 3.6 nm. The authors concluded that the size effect dominates over the site effect. A recent study using DRIFTS at nanoparticles surfaces suggests that there is no size effect for particle size less than 1.29 nm, but the size effect occurs for larger nanoparticles where the number of Pt atoms of (111) facets is much larger than atoms at edges and corners [103].

Much work has been dedicated to characterize CO chemisorption on transition metal (TM) surfaces. There are many papers that deal on the electronic, structural and vibrational properties [99, 108–110]. In this respect, the central questions emphasized are the bonding mechanism of CO, the strength of the chemisorption of CO and the specific adsorption site preference for various TM series. The specific case of CO adsorption on the Pt(111) slab surface has received much attention in the past two decades, because for this system state of the art DFT calculations fail in predicting the correct site preference which was noticed the first time by Feibelman et al. in their classic paper [111]. Since then, many different variants of density functionals have been applied and regardless of program and functional, parameter-free standard DFT calculations predict the wrong adsorption site [112, 113]. That is theoretical findings suggest that three-fold sites are the most favored ones, whereas experimental measurements propose the on-top site. The same problem of wrong predictions found to have happened also for Cu and Rh metals. For this discrepancy, new findings suggest that the origin of the problem is an overestimation of the bond strength of the empty molecular frontier orbital with the substrate [113].

CO orbitals and bonding

The fundamental understanding and description of the chemical bond formed upon adsorption is very important in heterogeneous catalysis. The electronic structure analysis gives deep insight to understand the interaction between adsorbate and metals. First, let us see the electronic structure of isolated gas phase CO molecule to gain full picture of the molecular orbital (MO) before interaction with metal surface. This prior orbital resolved analysis helps to understand how the MOs of CO rearrange upon interaction to the surface [114]. The valence molecular orbitals of the isolated gas phase CO are 3σ, $4\sigma^*$, $[1\pi_{p_x}, 1\pi_{p_y}]$, $5\sigma_p$ (see Figure 6.1). The highest occupied molecular orbital (HOMO) of CO is 5σ orbital. The 5σ orbital is localized mainly on the carbon atom and the CO molecule binds in an upward position with carbon pointing towards the surface. The two bonding 1π orbitals located below the 5σ orbital and the lowest unoccupied molecular orbitals (LUMO) of the two anti-bonding $2\pi^*$ orbitals lie above the 5σ orbital. Figure 6.1 shows the atom-projected density of states (PDOS) for the isolated CO molecule with the corresponding s and p orbital contributions. The first peak represents the $4\sigma^*$ formed by sp hybridization. The second intense peak corresponds to the two fold degenerate 1π orbitals. The third peak represents the 5σ orbital that is obtained from the sp hybridization. The last intense peak located above the Fermi level represents the two fold degenerate π anti-bonding orbitals. As visualized from orbital resolved PDOS, it seems that the σ molecular orbitals are created from hybridized s and p orbitals, while the π molecular orbitals are fully from p contribution. As can be seen, the frontier molecular orbitals, i.e. 5σ and $2\pi^*$ are predominantly populated at carbon atom, whereas $4\sigma^*$ and 1π molecular orbitals mostly located at oxygen atom.
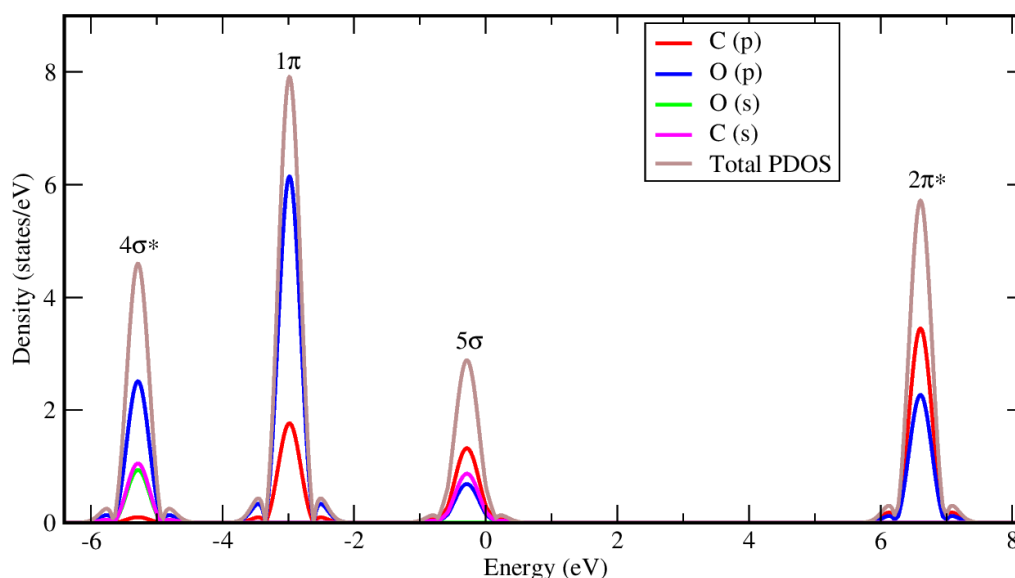
Figure 6.1: Atom projected density of states of the CO molecule. The total density of states (brown color) along with orbital resolved s and p states of C and O are shown.

The interaction between CO and metals surfaces is usually described with respect to the Blyholder model [108] in which the frontier orbitals of CO couple with the d-band of the metal. The underlying idea of the Blyholder model is that the interaction is carried out through two

way donation, i.e., forward donation from the occupied CO-5σ orbital to the empty metal band and back donation from the occupied metal band to the empty $2\pi^*$ CO orbitals. Following this model, considerable clarifications and improvements have been proposed. Many of the studies are in complete agreement with the Blyholder model [115, 116]. However, later it was found that the Blyholder model has a major limitation of ignoring the contribution of $4\sigma^*$ and 1π orbitals [117, 118]. It should be noted that basically the Blyholder method is valid except its oversimplification of the bonding by assuming that bond is created only from contribution of frontier MOs. On the other hand, based on experimental and theoretical investigations Nilsson et al. [119, 120] and Föhlisch et al. [121] suggested that the CO $4\sigma^*$, 1π, 5σ and $2\pi^*$ orbitals undergo re-hybridization upon adsorption and can all contribute to the interaction with the metal d-band.

The CO frontier orbitals, 5σ(HOMO) and $2\pi^*$ (LUMO) are located closer to the Fermi level, making the $2\pi^*$ orbital very close in energy to the metal d-band, which results in an overestimated bond strength of the the back-bonding interaction from d-band to $2\pi^*$ [122]. The bonding of CO at different adsorption sites and metals results to a different degree of back-bonding. It was found that the back-bonding increases with increasing coordination of CO in the adsorption site, i.e. hollow > bridge > top [123]. It is generally accepted that non-hybrid density functional calculations have a tendency to underestimate the HOMO-LUMO gaps for molecules, and this is the case also for CO that the LUMO energy is predicted to be lower than it should be [124]. Thus, the DFT wrong preference of problem associated with the strength of the back-bonding. For the case of Pt nanoparticles, even though the site preference error persists at the center of (111) facet, the correct preference is obtained on the edges of nanoparticles [125, 126]. The CO bonding details on Pt and Pd model surfaces will be given in section 8.1

6.2 Oxygen adsorption on transition metal surfaces

Oxygen is an important chemical species in many heterogeneous redox reactions, for example the oxygen reduction reaction, CO and hydrocarbon oxidation in catalytic converter and oxidative formaldehyde production from methanol. In this thesis oxygen adsorption is investigated in detail on Pt and Pd nanoparticles by primarily targeting CO oxidation reactions. However, the calculated oxygen adsorption properties can be transferred to many other chemical reactions including oxygen reduction reactions and methanol oxidation. The knowledge gained on oxygen bond strength will be helpful for the description of the reactivity of adsorbed oxygen on the surface of metals. In addition, the adsorption energy of oxygen can be related to other similar chemical species using scaling relationships. The reactions of adsorbed O with CO is one of the well-known oxidation reaction that follows the Langmuir-Hinshelwood mechanism [127]. The adsorption energy of the adsorbed O and CO correlates with the barrier of the CO oxidation reaction, such that the barrier is low on inert surfaces and generally higher on more reactive surfaces [128]. Under realistic reaction condition O_2 adsorbs dissociatively on Pt and Pd surfaces [129]. On Pt_{38} and Pt_{79} truncated nanoparticles, O_2 dissociation has been calculated to

be barrierless [130]. The binding strength and degree of charge transfer to adsorbed O_2 and O follow similar periodic trends. A linear correlation of adsorption energy of O and O_2 have been found on different monometallic surfaces using a scaling relation [19, 131]. To study the structural and electronic property of the oxygen adsorbate on the surface of the metal, spectroscopic techniques are frequently used. For example, vibrational spectroscopy can be used to determine the adsorption state of O_2. High-resolution electron energy-loss spectroscopy (HREELS) can be used to measure vibrations with lower wave numbers that enables to detect M-O or $M-O_2$ bonds. On the Pt(111) surface, for example, these have wave numbers of 480 and 380 cm^{-1}, respectively [132]. Low-energy electron diffraction (LEED) and scanning tunneling microscopy (STM) techniques can be applied to obtain structural information on adsorbates on the surface. On the other hand, X-ray spectroscopy methods, such as near edge X-ray absorption fine structure (NEXAFS) and surface-extended X-ray absorption fine structure (SEXAFS) can be used to determine the electronic structure and chemical nature of the adsorbed species.

Determination of adsorption properties of CO and O on Pt and Pd nanoparticles will be the central focus of the next chapters, since these species can be applicable in many reactions. Due to structural complexity different adsorption sites of nanoparticles have different adsorption strength and activity. Adsorption energy calculations on nanoparticles of different size and surface morphology can provide information for structure-function correlation.

Chapter 7

Model System and Computational Methods

7.1 Model System

The functionality of nanocatalysts is related to the particle structures in terms of size and shape. To investigate the size and shape effect towards CO and O adsorption energy, various nanoparticle sizes and shapes have been chosen. Equilibrium shapes of nanoparticle model catalysts can be constructed using the Wulff construction method [133]. These nanoparticle structures can be classified to regular octahedron, truncated octahedron, cuboctahedron and rhombicuboctahedron in which each of them consists of different features of surface structure, see Figure 7.1 [134]. All of these structures are based on face-centered cubic (fcc) crystal packing, as the thermodynamic structure for both Pt and Pd is known to be face-centered cubic. The selected model nanoparticles differ to each other by the surface planes they comprise. Regular octahedron structures are entirely constructed from {111} facets, while the truncated octahedrons are constructed from the {111} and {100} facets with {111} being the dominant part. Similarly, the surface cuboctahedron structures constructed from {111} and {100} facets and the dominant surface is {100}. Furthermore, to increase the variety rhombicuboctahedron structures are considered, which possesses adatoms and high index facets. The surface energies of the facets increase in the order {111} < {100} < {110}. Exposure of different crystal facets can substantially change the catalytic activity due to different characteristic atomic structures and surface free energies [135]. For each class of nanoparticles considered, different sizes are taken to study the size effect (which have different percentages of surface-to-volume ratio). The model nanoparticle structures investigated here are constructed using atomic simulation environment (ASE) [81] and python materials genomics (Pymatgen) [136]. These structures are stable based on the Wulf construction [134]. They have been investigated for different purposes in the reported works. For instance, for the study of CO adsorption properties Pt_{55}, Pt_{147}, Pd_{146} and Pd_{147} [15, 137] were used. For oxygen reduction reaction Pt_{38}, Pt_{79}, and Pt_{201} [138] have been employed. Similarly, Pt_{38} and Pt_{79} have been used for the study of oxygen dissociation barrier[130] .
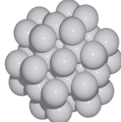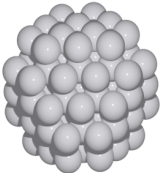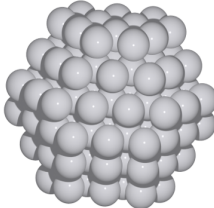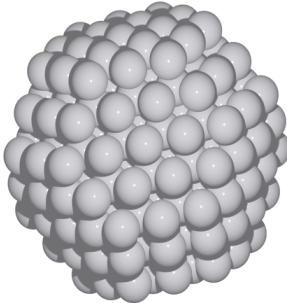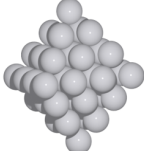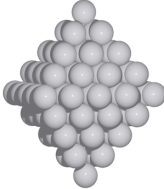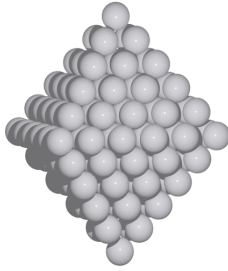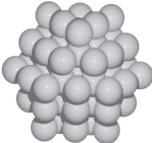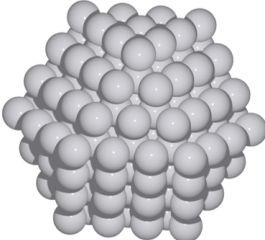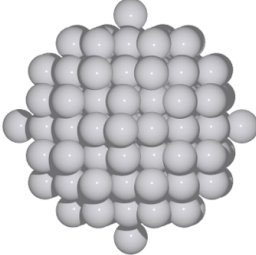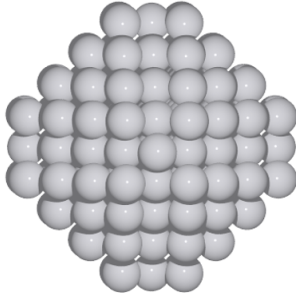
(A)

Size	M$_{38}$ (0.8 nm)	M$_{79}$ (1.1 nm)	M$_{116}$ (1.3 nm)	M$_{201}$ (2 nm)
Surface atoms (%)	84.2	75.9	67.2	60.2

(B)

Size	M$_{44}$ (0.8 nm)	M$_{85}$ (1.1 nm)	M$_{146}$ (1.6 nm)
Surface atoms (%)	86.3	77.6	69.8

(C) **(D)**

Size	M$_{55}$ (1 nm)	M$_{147}$ (1.6 nm)	M$_{141}$ (1.6 nm)	M$_{165}$ (1.7 nm)
Surface atoms (%)	76.3	62.5	69.5	74

Figure 7.1: Nanoparticle structures of truncated octahedron (A), regular octahedron (B), cuboctahedron (C) and rhombicuboctahedron (D). For each structure, the number of atoms, approximate nanometer size and percentage of surface-to-volume ratio are given. The bulk structure of Pt and Pd is face centered cubic packing (fcc).

Figure 7.2 illustrates the different surface plane fractions of truncated octahedron nanoparticle, which includes the (111) and (100) facets, i.e. terraces and defect sites (edges and corners). The representations 111 × 100 and 111 × 111 indicates the edges between (111) and (100) facets and between two (111) facets, respectively.
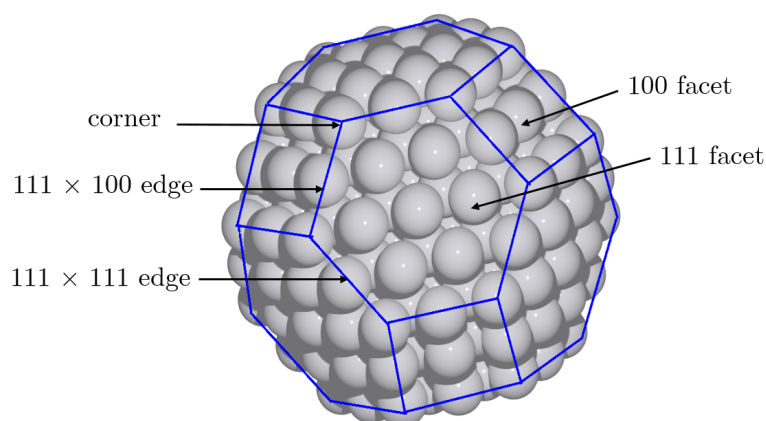
Figure 7.2: The different surface plane portions on Pt_{201} nanoparticle. The blue lines mark the area of (111) and (100) planes and the black arrows indicate terraces of (111) and (100) facets, edges and corners of the nanoparticle.

Figure 7.3 shows the possible adsorption sites on the surface of nanoparticle structures, which are on-top, bridge, 3-fold hollow and 4-fold hollow sites. The on-top (one-fold) site is when an adsorbate binds to a single surface metal atom. At the bridge (2-fold) site the adsorbate binds to two surface metal atoms. The 3-fold hollow site is when an adsorbate binds to three surface metal atoms. There are two types of 3-fold sites that are fcc and hcp. The difference between the two 3-fold hollow sites is that there is an atom in the second layer directly below the hcp, which is absent for the fcc site. Similarly, 4-fold hollow stands for adsorbates bind to four surface metal atoms.
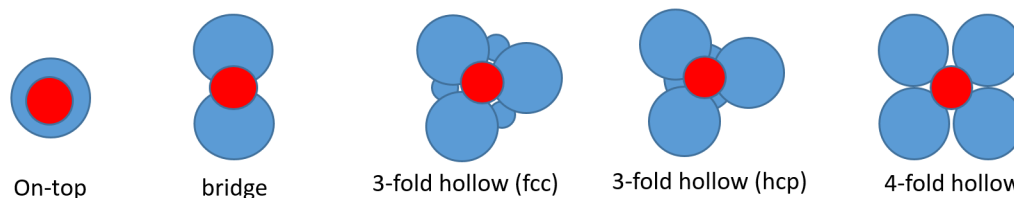
Figure 7.3: The possible adsorption sites on the surface of model catalysts. The red and blue circles indicate an adsorbate and metal atoms, respectively.

7.2   Methods

The descriptor based study of catalytic properties is very important to understand chemical catalytic phenomena and to predict the trends in catalytic activity, which will enable the rational design of surfaces with specific catalytic properties without extensive trial-and-error experiments. In this context, it is essential to find physically meaningful and yet robust descriptors to represent the various properties of catalysts. In the theoretical catalysis study, electronic and geometric descriptors have been widely applied. Specifically the average energy of the d-band relative to the Fermi level (d-band center) and generalized coordination numbers ($\overline{CN}$) are the most used parameters.

By assuming that d-electrons of transition metals play the dominant role in the chemisorp-

tion, Nørskov et al. developed the d-band center model [110, 139]. This model connects surface chemical properties with the electronic structure of metal containing surfaces and this has been generally deemed as a suitable descriptor for surface reactivity. The d-band center (ε_d) is defined relative to the Fermi level (E_f), as a function of the density of states of the metal.

$$\varepsilon_d = \frac{\int E\rho(E - E_f)dE}{\int \rho(E - E_f)dE} \tag{7.1}$$

where $\rho(E)$ denotes the projected density of states (pDOS) of the dband and E_f is the Fermi level energy.

By using the DFT calculated pDOS, the d-band center descriptor has been applied to determine trends of the adsorption energy strength for a given adsorbate on various metals. The position of the d-band center is interpreted relative to the Fermi level. The higher the d-states are in energy relative to the Fermi level, the more empty the anti-bonding states and the larger the adsorption energy (strong bonding between the adsorbate and metal surface). By comparing the relative positions of the d-band centers of different metal surfaces, the relative chemisorption energies and reactivity properties of various molecular reactions on these surfaces can be predicted. Such calculations have been widely utilized in the catalyst design for many important target reactions [140]. Even though d-band center theory is a widely used descriptor in chemical reaction modeling, it has some pitfalls. The first shortcoming is that the application of d-band center theory is limited to metal surfaces that contain d orbitals. Second, d-band center results contain no spatial information; hence, they cannot provide any description about the reactivities of different surface sites. In other words, it fails to differentiate the activity of various possible active sites of the same metal surface [141]. Yu et al. [142] have applied the d-band center model to determine the catalytic activity of the oxygen reduction reaction (ORR) by taking the adsorption energy of OH at (111) and (100) facets of various fcc metals. In their study, it was found that the d-band center does not necessarily correlate with the binding energy. They have finally claimed that without linear correlation of the d-band center and adsorption energy the quantitative relationship between the catalytic activity and d-band center is questionable. Moreover, they pointed out that d-band center depends considerably on the calculation method and the experimental setup, which makes it a less reliable indicator for ORR activity than the oxygen binding energy. In the same direction, Nørskov et al. [143] have provided comments to the reason why d-band center could not correlate with the ORR activity for metals of different coupling matrix and they have suggested to use binding energy instead of d-band center. Despite these limitations, it remains applicable for many practical surface reactions [110, 140].

Recently alternative descriptors have been introduced based on the surface geometry (coordination number) of a given catalyst without any prior electronic structure calculation [144]. In chemistry coordination numbers (CN) are used to describe the electronic environment of a solid/molecule and to predict its tendency to form bonds. For example, fcc bulk crystal atoms have a twelve fold coordination by nearest neighbor atoms. If the coordination number is below twelve (which is the case for surfaces), a tendency for bond formation will be expected to

compensate for the deficient coordination. However, in general this usual coordination number is not accurate to describe the activity of a given active adsorption site. The first thing is the bonding at a certain active site can be affected not only by the first nearest neighbor atoms but also by the second nearest neighbors. The other limitation of the usual coordination number is that adsorption site of nanoparticles of different size could have the same coordination number. For example this happens when we take terrace sites of Pt_{79} and Pt_{201} nanoparticles which both have CN = 9 but their adsorption energies are different for the same adsorbate because of the effect of the second nearest neighbors. On the other hand, the generalized coordination number [138] allows to differentiate effectively those sites by including the contributions from second nearest neighbor atoms. The generalized coordination number ($\overline{CN}$) of an atom i with n_i nearest neighbors and those neighbors are counted and weighted by their own usual coordination number defined as

$$\overline{CN}_i = \sum_{j=1}^{n_i} \frac{CN_j}{CN_{max}} \tag{7.2}$$

That means each neighbor of atom i is counted and normalized by the bulk coordination number (CN_{max}). For fcc crystal the bulk coordination number (CN_{max}) is 12.
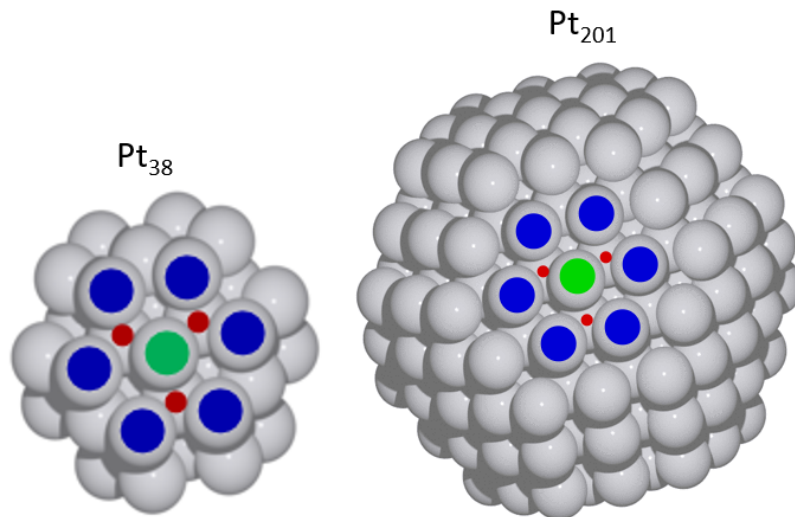
Figure 7.4: Sites with CN = 9 (green) on Pt_{38} and Pt_{201} surface.The six surface nearest neighbors (blue) and the three in the subsurface (red) are marked.

For example, the green site on Pt_{38} in Figure 7.4 has six neighbors with CN = 6 (blue) and three with CN = 12 (red). Similarly, on Pt_{201} the green site has six neighbors with CN = 9 (blue) and three with CN = 12 (red). That is both sizes have nine normal coordination number (CN). However, the generalized coordination number ($\overline{CN}$) for the green site on Pt_{38} is equal to $(6 \times 6 + 3 \times 12)/12 = 6.00$ and on Pt_{201} is $\overline{CN} = (6 \times 9 + 3 \times 12)/12 = 7.5$. In other words, each of the six neighbor atoms (blue) are in turn coordinated with six neighbors on Pt_{38} and nine on Pt_{201}. Similarly, the three neighbor atoms (red) in the subsurface are in turn coordinated with twelve neighbor atoms on both Pt_{38} and Pt_{201}. In this way, by including the contribution of the first and second nearest neighbors of an active site, the $\overline{CN}$ contains

more information about the local structure and thus can capture the local environment more accurately. The $\overline{CN}$ descriptor have been applied for oxygen reduction reaction (ORR) on Pt nanoparticles [138], in CO_2 reduction reactions on Cu surfaces [145], and prediction of catalytic activity of nanoparticles using a machine learning approach [146]. In all cases, it has proven to be a good descriptor. However, there are some cases $\overline{CN}$ is not applicable, for example, for alloyed structures or for coverage studies. Because $\overline{CN}$ is geometrical descriptor, it might not help to differentiate the atom type in alloyed system.

The adsorption energy of a CO molecule on M_N (M = Pt and Pd) nanoparticles is defined as

$$E_{ads}(\text{CO}) = -[E(M_N + \text{CO}) - E(M_N) - E(\text{CO})] \tag{7.3}$$

where $E(M_N + \text{CO})$ is the total energy of the N atom M nanoparticle with one adsorbed CO molecule, $E(M_N)$ is the energy of the isolated N atom M nanoparticle and $E(\text{CO})$ is the energy of the isolated CO molecule. Note that the adsorption energy is calculated in the reverse way with (-) sign for the purpose to use positive values. Similarly, the adsorption energy of singly adsorbed atomic oxygen is given as

$$E_{ads}(O) = -[E(M_N + O) - E(M_N) - \frac{1}{2}E(O_2)] \tag{7.4}$$

where $E(O_2)$ is the energy of an O_2 molecule. The average adsorption energy of oxygen for atomic oxygen covered nanoparticle (Θ) is defined as

$$\overline{E}_{ads}(O) = -\frac{1}{N_O}\left(E^{\text{total}}(\Theta) - E^{\text{total}}(\text{bare}) - N_O \times \frac{1}{2}E^{\text{total}}(O_2)\right) \tag{7.5}$$

where $E^{\text{total}}(\Theta)$, $E^{\text{total}}(\text{bare})$ and $E^{\text{total}}(O_2)$ are total energies of the oxygen covered nanoparticle, the bare nanoparticle and the oxygen molecule. N_O is the number of adsorbed oxygen atoms. Furthermore, the adsorption energy of CO on oxygen covered nanoparticle surfaces is given by

$$\dagger E_{ads}(\text{CO}) = -\left(E^{\text{total}}(\Theta + \text{CO}) - E^{\text{total}}(\Theta) - E(\text{CO})\right) \tag{7.6}$$

where $E^{\text{total}}(\Theta + \text{CO})$, $E^{\text{total}}(\Theta)$ and E(CO) are total energies of the CO adsorbed oxygen covered nanoparticle, oxygen covered nanoparticle and CO molecule, respectively.

7.2.1 Computational Details

All calculations were performed using the Vienna ab initio simulation package (VASP) code [147, 148] integrated with [81]. The atomic simulation environment (ASE) has been used to construct nanoparticle and slab model catalysts. The core electrons were described by using projector augmented wave (PAW) potentials [149]. The valence electron wave function was expanded using plane waves with an energy cutoff of 450 eV. The Perdew-Burke-Ernzerhof (PBE) [67] generalized gradient approximation was used to describe the exchange-correlation functional. The PBE density functional calibrated Pt and Pd lattice constants (3.97 and 3.94

Å, respectively) were used; these values are in good agreement with the respective experimental values (3.92 and 3.89 Å, respectively) [89]. All atomic geometries were fully relaxed and the spin-polarized formalism was used. The Pt and Pd nanoparticles were modeled by a supercell with 3-dimensional periodic boundary conditions in a simple cubic cell. A large vacuum region along each of the three directions was used to ensure that the interactions between each nanoparticle and its periodic image are negligible (the distance between two nearest surface atoms in neighboring images is at least 16 Å). The Brillouin zones of Pt and Pd nanoparticles were sampled by the gamma point only. The extended Pt(111), Pt(100), Pd(100) and Pd(111) surfaces were modeled by a five-layer slab and the two bottom layers were fixed during relaxation with a (2 x 2) unit cell. A vacuum layer of 10 Å was used to separate periodic images along the z direction. The Brillouin zones of the slab surfaces were sampled using a (6 x 6 x 1) k-point mesh based on the Monkhorst-Pack scheme [88]. The geometry optimizations were performed using the conjugate gradient algorithm until the maximum force on any atom was below 0.05 eV/Å and the electronic relaxation was fixed to the threshold energy 10^{-6} eV. The first order Methfessel–Paxton smearing method [150] of 0.2 eV smearing width was applied. The nudged elastic band (NEB) method implemented in ASE was used to calculate the diffusion barriers of oxygen adsorbates [81].

7.3   Data model, data store and workflow

In this work, an enormous amount of electronic structure calculations data have been generated and stored with directories in the HPC hard disk drives. However, it is hard to use the required data and to retrieve a certain calculation in the presence of vast amount of not properly structured data (even by myself after some time). However, organizing the calculation details including the inputs, outputs and calculator parameters setting in a structured format in a database helps enormously to easily reuse the data and reproduce the calculation whenever required. Moreover, such database can be used as data source for secondary complex simulation such as micro-kinetic modeling and machine learning. As a result, designing a database model that suits the nature of current calculation data will be useful. For that purpose, I have designed a data model using a MongoDB database program and the relevant information of this work are stored there.

To start from the definition, a database is a collection of organized digital information (data) which enables to access, manage and update data easily. MongoDB [151] is a non relational database program that stores documents in binary java script object notation (JSON or BSON) format and provides flexible data modeling support. JSON is a standard data format which provides a structure that align well with the object-oriented programming languages. Most modern computer programming languages provide native parsing and generation of JSON files [152]. Because scientific applications are very dynamic in terms of data models, MongoDB is a suitable choice due to its flexible schema. Unlike relational databases that store data in tables consisting of columns and rows, MongoDB stores data in collections that contains JSON object

documents.

MongoDB is a container for collection and a collection in turn is a container to a group of similar structure documents that have a set of unique indexes. A document is a single entry to the collection and all documents in a collection do not necessarily have the same set of fields. Listing 7.1 shows an example of typical MongoDB document structure in JSON format. The field values in the document can be strings, numbers, arrays and arrays of embedded documents.

```
{
        "molecule name": "CO",
        "atomic numbers": [6, 8],
        "number of electrons": 14,
        "properties": [
              "physical properties":{"melting point (K)": 68.13,
                                      "boiling point (K)": 81.6
                                     },
              "molecular properties":{"bond length (pm)": 112.8,
                                       "molecular mass (g/mol)": 28.01
                                      },
                   ],
}
```

Listing 7.1: MongoDB document example

In MongoDB, each document is identified by a unique ID (_id field), which can be given by the user upon document creation or automatically generated by the database. An index is automatically created on the ID field although other indexes can be manually created in order to speed up common queries. Relationships can be modeled in two different ways embedding documents (denormalized) or referencing documents (normalized). Embedding documents means that a document might contain other data fields related to the document. In referencing relationship, instead of embedding the whole data, the document might instead store the ID of the foreign document that targeted to be linked. For example, in Listing 7.1 the properties field has array of two embedded documents which is type of embedded relationship. This can be represented in referenced relationship by taking one of the properties field values to another document and link them by the unique identifying ID. The document relationships can be one-to-one, one-to-many and many-to-many. Generally, embedding provides better performance for read operations, as well as the ability to request and retrieve related data in a single database operation. Embedded data models make it possible to update related data in a single atomic write operation. However, embedding related data in documents may lead to situations where documents grow after creation and document growth can impact write performance and lead to data fragmentation [153]. Therefore, in case of large document a referencing relationship instead of embedding is helpful.

Data modification and query are carried out by MongoDB supported fundamental operations so called CRUD, which stands for Create, Read, Update and Delete documents. The CRUD operation takes place at the collection level. Create operation (insert operation) is used to add new documents to the collection and if the collection does not exist, it creates one.

The command to insert a document is **db.collection.insert()**. The rsead operation read or queries documents from a collection. The command to read or query a document is **db.collection.find()**. Update operations are used to modify the existing document. The command to update a document is **db.collection.update()**. Delete operations remove a document from a collection. The command to delete a document is **db.collection.delete()**. In the present work, the data model has been designed using Python language via Pymongo. Pymongo is a MongoDB driver made to work with Python programming language.

7.3.1 Data model design

In MongoDb, the user is free to design a database as she/he wishes that fits to a given application and inherent data type. The main challenge in database design is to scrutinize in advance the data application, querying and processing of data so that the designed database will be effective and easy to use. In general, a good database design needs to consider the following questions: How does the inherent structure of the data look like? What are the application requirements? What are the relationships between the data? How are we going to query and update the data?
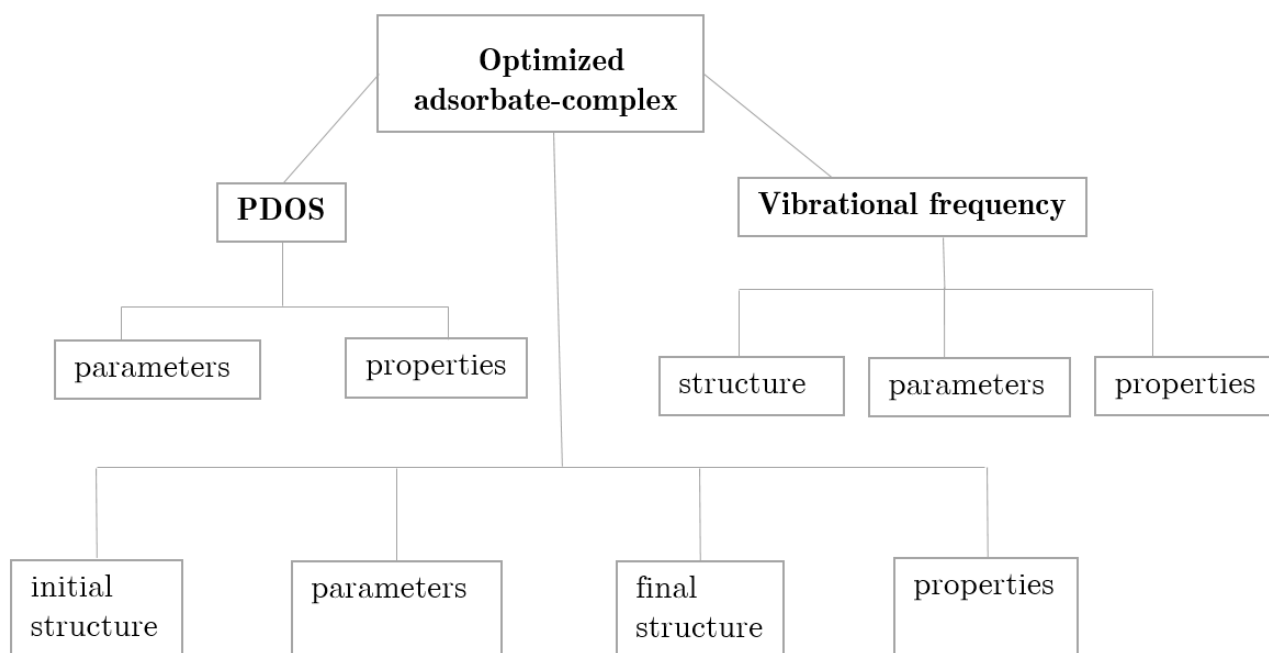
Figure 7.5: An example of calculation documents that are ingested and stored into the database. The optimized adsorbate-complex structure is taken as input for PDOS and vibrational calculations. The parameters, structures and properties documents are extracted from each of the calculations.

As for any electronic structure calculation, the data in this work consists of input/initial structure, calculator parameters, output/optimized structure and results (properties) in the format of the simulation package. However, these calculation input and output files cannot be directly taken into the database and need to be serialized into JSON format. In other words, all the structure, parameter and property files should be organized and transformed into a

MongodDB compatible data model. This step is very important and not straightforward. It requires an interfacing script that can integrate to electronic structure simulation package and ingest data from a set of calculations. The data ingestion and data modeling have been accomplished through the use of a Python script and ASE. Figure 7.5 shows an example of the data type ingested and taken into database based on an optimization step of the structure of the adsorbate-complex. For optimization calculations initial and final structure, parameters and properties files are taken and stored into the database. Moreover, vibrational mode analysis and projected density of state (PDOS) computation carried out by taking optimized structure as input. In case of PDOS, parameters and properties data are enough as the there is no structure change and for vibrational frequency, structure data is also included as it comprise constraint information. Analogously, for substrate bare nanoparticle and adsorbate, initial and final structures, parameters and properties are taken into the database.

For the purpose of data model design, those data are categorized into three collections, i.e. structure collection, parameters collection and properties collection. The structure collection contains all starting and optimized structures of the calculations. The parameters collection contains the calculator settings that have been used for a particular calculation. The properties collection contains the calculation results, for example–total energy, force, vibrational frequencies, adsorption energy etc. Figure 7.6 shows the designed database data structure
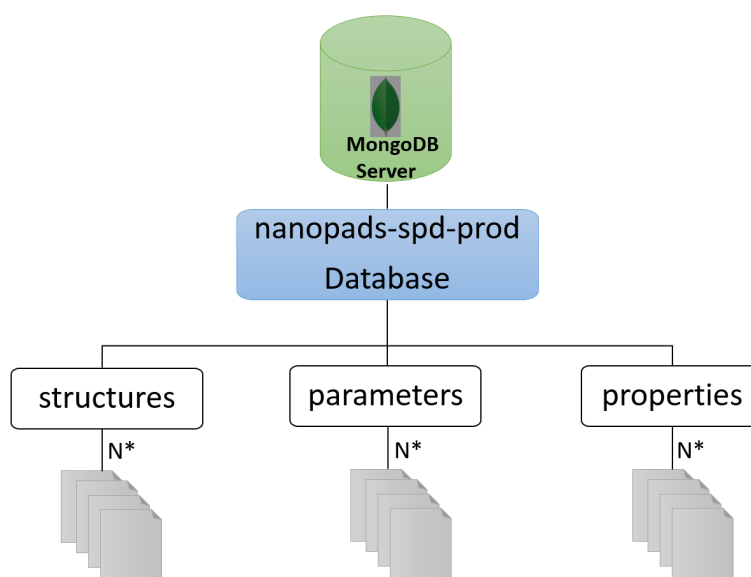
Figure 7.6: Database data structure model that organized into three collections (structures, parameters and properties) and N number of documents (N*) in each collection. The name of the database is nanopads-spd-prod.

organization. The database created is named nanopads-spd-prod which refers to nanoparticle adsorption structure-property database. Thus, the nanopads-spd-prod database contains structures, parameters and properties collection and each collection in turn contains N numbers of documents.

So far we have seen the designed database organization and the type of documents stored. However, designing a relationship between documents that belong to the same calculation is

very crucial. In this work, DBRefs method is applied for relating documents. DBRefs are used to reference one document to another using the first documents _id field, collection name and optionally, its database name. By including these names, DBRefs allow documents located in multiple collections to be more easily linked with documents from a single collection. Here, a one-to-many relationship is established by referencing parameters and structures document into the properties document using the unique identifier _id of the document. This means that while querying a certain properties document, we can dereference and find structures and parameters document that yielded the property using only the properties collection. Indeed, it is possible to query documents in each collection without dereferencing. The structures, parameters and
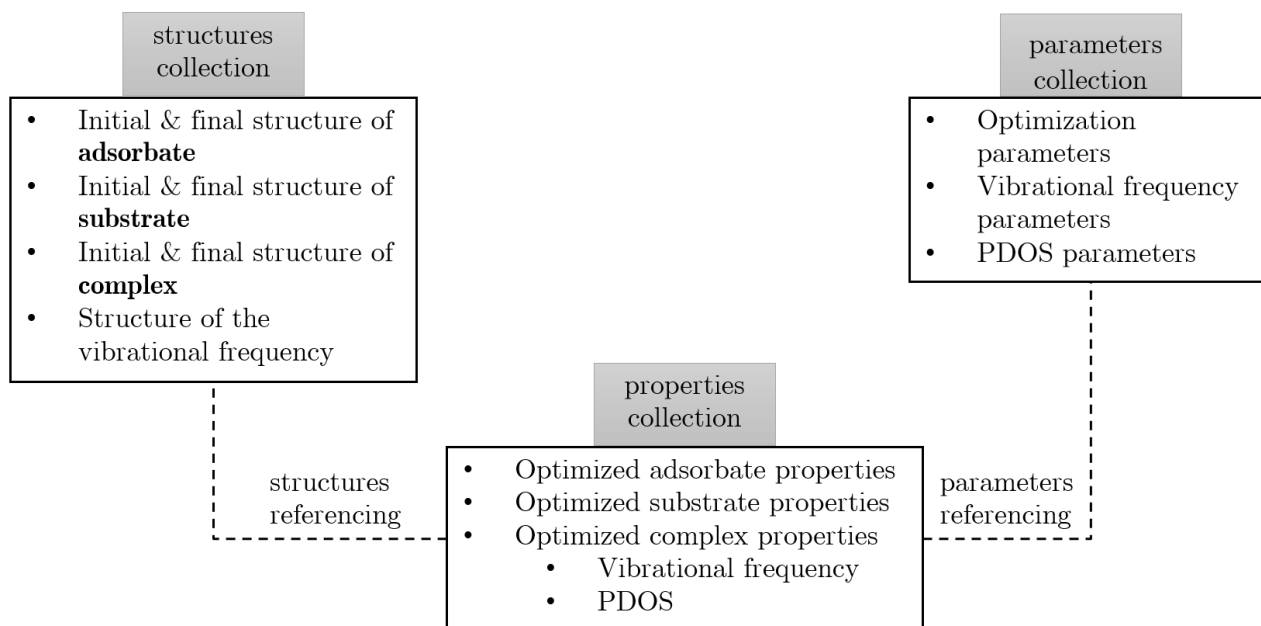
Figure 7.7: Data model relationship between documents across the collections. The parameters and structures document referenced in properties document. The _id field of parameters and structures document is linked into properties document. The type of documents inserted to each collections are listed.

properties document that belong to the same calculation are set to have the same metadata so that one can query those documents using the same metadata. The metadata contains information about the size of nanoparticle, adsorbate type, adsorption site and generalized coordination number (GCN) descriptor. Figure 7.7 shows the type of documents stored in each of the three collections and the link or relationship between the documents across the collection. The the dotted lines designate the referencing of documents of the structures and parameters collection into the documents in the properties collection. Thus, the ID of parameters and structures document are linked into the properties document. For each particular adsorption site, all the structures of the adsorbate, substrate and complex are embedded in one document and so do parameters and properties. This simplifies the query and calculation of adsorption energies. An example of a querying script and sample documents are presented in Appendix A.

7.3.2   High throughput workflow

The present work is mainly dedicated on calculation of chemisorption properties of oxygen and CO on Pt and Pd catalyst models, which cover a wide range of adsorption sites and nanoparticle sizes. All these calculations are performed in a massively parallel manner using high performance computers. Even though most of the calculation procedures are similar, the number of calculations is very large. Besides, the calculations steps and data analyses are sequentially inter-linked. For example, vibrational modes and density of states calculation are carried out using the pre-optimized structure. Furthermore, the post-process analysis requires to link two or more calculation results. Thus, manually preparing inputs and running such calculations is tedious and needs much human effort and time. Instead, automating calculation procedures using high-throughput (HT) workflow techniques, and perform simulations either in parallel or sequentially, is a very valuable approach. In this work, the FireWorks (FWs) [154] workflow management system is employed. FWs is a free, open-source code implemented
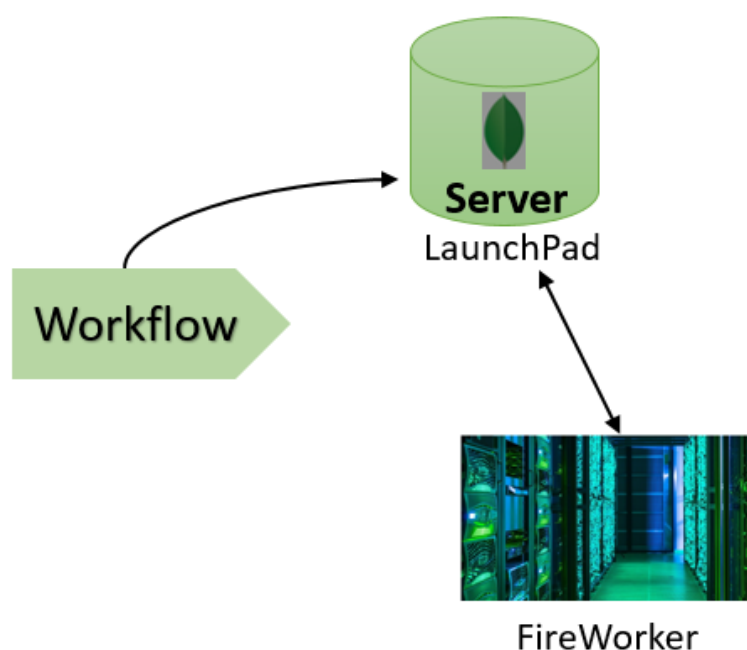
Figure 7.8: Main components of FireWorks workflow and infrastructure.

in the Python language for defining, managing, and executing complex workflows. It focuses on high-throughput computing and has been developed in the context of materials research and deployed in the Materials Project [155]. Here, a workflow refers to a full procedures and description of the calculation steps. FWs is a flexible workflow tool that possesses useful features. Some of its features are built-in tools, database back-end (MongoDB) and failure detection and supporting several queuing systems [156]. The advantage of FWs workflow is two-fold: first it helps to minimize the human effort to manage large number of calculations. Second, the results and the necessary provenance information of the calculation are directly stored to the back-end MongoDB database which enables to analyze the data and to reproduce the calculation if necessary. FWs infrastructure constitutes of three main parts: the workflows,

LaunchPad and FireWorker, see Figure 7.8. In the workflow all jobs and steps of calculation are defined. LaunchPad is a MongoDB back-end server on which the workflows and their metadata and states are stored. Query and update of workflows is carried out on LaunchPad. The FireWorkers pull workflows from the LaunchPad, execute them, and send back the results and update the workflow.
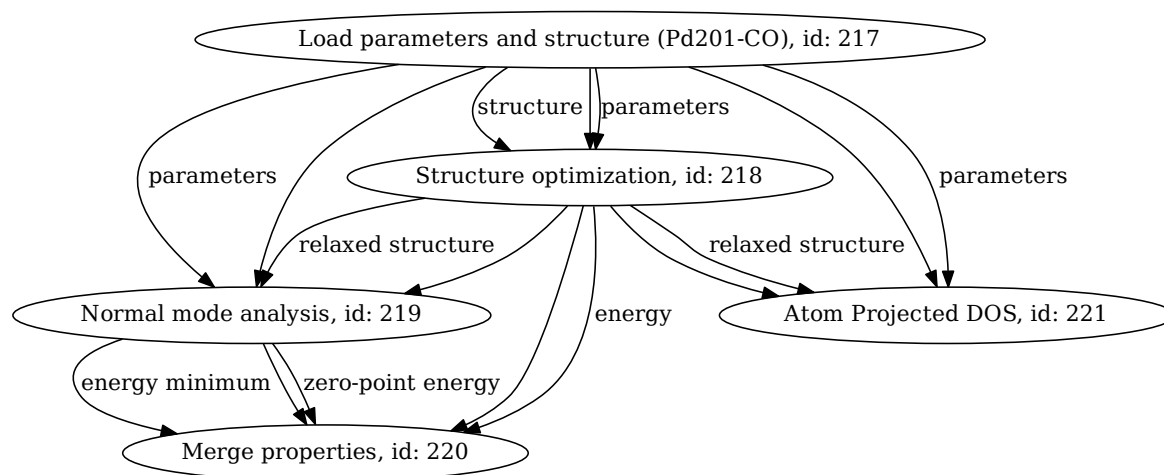
Figure 7.9: An example of workflow graph that contains five fireworks (the graph vertices) connected by dependencies (the graph edges) denoted by arrows.

Figure 7.9 depicts a workflow that carried out geometry optimization, normal mode analysis and atom projected DOS calculations. As can be seen, the first Firework (id: 217) loads structure and calculator parameters. The second Firework (id: 218) does a geometry optimization by taking structure and parameters from 217. Firework 219 calculates the normal modes but it takes the parameters from 217 and the relaxed structure from 218. Similarly, Firework 221 calculates atom projected DOS by taking parameters from 217 and relaxed structure from 218. Firework 220 collects results from the optimization and the normal mode analysis steps.

Chapter 8

Results and Discussion

8.1 CO bonding mechanism on Pt and Pd surface

CO bonding on Pt surfaces

In this work, to understand the bonding of CO molecule with Pt and Pd metal surfaces, the projected density of states of $4\sigma^*$, 1π, 5σ and $2\pi^*$ MOs of the adsorbed CO molecule are considered. Two adsorption sites that is on-top and 3-fold hollow (fcc) sites are selected to analyze the orbital-wise interaction. Figure 8.1 shows orbital resolved projected density of states for CO adsorbed on fcc and on-top sites of a Pt slab. Upon adsorption of the CO molecule at the Pt surface, the $4\sigma^*$ orbital shifted significantly to lower energies and located below the metal s and d-band. As a result, it has minor role in the bonding. A slight $4\sigma^*$ and -5σ orbital mixing is observed (green and red color). However, 5σ, 1π and $2\pi^*$ orbitals are the dominant contributors to the bonding with the Pt. These orbitals are in general shifted down and broadened upon adsorption. The empty d-band is also shifted towards the Fermi level. The 5σ orbital (HOMO) hybridized with the metal by donating electron to the empty s and d- band of the metal. This interaction is stronger on-top site than on fcc site. After adsorption the 5σ orbital lie below the 1π orbitals. Recall that it was above 1π orbitals before adsorption. The interaction of 1π and $2\pi^*$ orbitals with the metal surface, on the other hand, results to three distinctive peaks. The first peak positioned at -7 eV is mainly from interaction of 1π with metal d-band. The next peak in the energy range between -5 and -2 eV (blue shade) is newly developed non-bonding orbital ($d\pi$) and has oxygen lone pair character. Similar behavior has been found for CO on Ni(100) surface [117]. This orbital formed by main contribution of metal back donation. The last peak, at 3 eV is the empty anti-bonding $2\pi^*$-d hybridized orbital. This interaction shifts the d-band to lower energy as shown in Figure 8.1.

Considering the fcc site adsorption, the interaction is basically similar to on-top site adsorption, however, the bonding is now with three Pt atoms which leads to a slight pDOS change. The 5σ orbital is now higher energies, implying a weak interaction with d-band. This can be due to geometrical reasons that the Pt-C bond is increased compared to the on-top site. It has been shown that the 1π and $2\pi^*$ orbitals interact with the metal more strongly as justified by the intensive $d\pi$ peak below the Fermi level. Moreover, the anti-bonding $2\pi^*$ orbital is de-

Figure 8.1: Projected electronic density of states of CO adsorbed on a 2x2 slab surface (a) ontop and (b) fcc sites. The various colored lines show projections on the d and s orbitals of Pt atoms as well as $4\sigma^*$, 1π, 5σ and $2\pi^*$ orbitals of CO. The line with magenta color correspond to the adsorbate free surface d orbital projection. The Fermi level is located at 0 eV.

pleted, indicate a strong back donation of d-band and hybridization. In general it is noted that at fcc site the forward σ donation is relatively weak, whereas the π back donation is strong. Furthermore, one can say that the 5σ donation to the metal favors on-top adsorption and the back donation from the metal to $2\pi^*$ aid the 3-fold (fcc) adsorption. It is widely known that DFT functionals prefer 3-fold site CO adsorption over the on-top site at Pt(111) surface [111, 124]. It was pointed out that the reason for this wrong preference of DFT functionals is underestimation of HOMO (5σ)-LUMO ($2\pi^*$) gap in CO molecule, as a result facilitating the back donation [99].

CO bonding on Pt$_{79}$

So far we have seen the bonding mechanism of CO on Pt slab surface based on orbital projected electronic density of states. A similar analysis has done on Pt nanoparticles and compared with slab model. For that CO adsorbed on fcc and on-top site at center of Pt$_{79}$ (111) facet is chosen. Figure 8.2, shows orbital-wise projected density of states for the on-top and fcc sites. As provided from the graph, the overall orbital spectra are similar to the slab surface

Figure 8.2: Projected electronic density of states of CO adsorbed on Pt$_{79}$ surface (a) ontop and (b) fcc sites. The various colored lines show projections on the d and s orbitals of Pt atoms as well as $4\sigma^*$, 1π, 5σ and $2\pi^*$ orbitals of CO. The line with orange color correspond to the adsorbate free Pt$_{79}$ d band projection. The Fermi level is located at 0 eV.

adsorption described above. Analogues to slab model, $4\sigma^*$ located below -10 eV. However, some interesting features are emerged to the Pt$_{79}$. For example, unlike slab model, the HOMO (5σ) and 1π of CO exist as overlapped degenerate states. In addition, for the on-top adsorption two distinct peaks appear in the energy range -7 to -6.5 eV that is fingerprint of mixture of 5σ (red shade) and 1π (blue shade) which was not observed in the slab surface adsorption case. The d-band (black line) shifted to the Fermi level up on interaction with the 5σ and $2\pi^*$ CO orbitals compared to the bare Pt$_{79}$ d-band (orange). The LUMO ($2\pi^*$) of CO positioned between 3 to 4 eV and the $d\pi$ orbital hardly visible around -3 eV. On the other hand, in the case of fcc adsorption the two distinct peaks that appears on-top site is now exist as one peak due to the strong back-donation from metal d-band to empty $2\pi^*$. Nevertheless, the degeneracy

of 5σ and $2\pi^*$ retained. The degenerate peak shows up shift towards Fermi level compared to the on-top site reflecting strong back-donation and a visible $d\pi$ observed ≈ -2 eV. Moreover, the $2\pi^*$ peak intensity get lowered because of charge filling via metal d-band donation. Overall, stronger σ and π orbital hybridization is observed in case of Pt_{79} compared to slab model.

CO bonding on Pd surfaces

The overall bonding mechanism of CO adsorption on Pd surface is very similar to the bonding behavior of Pt surface as can be seen in Figure 8.3. Upon adsorption the d-band of Pd shifted
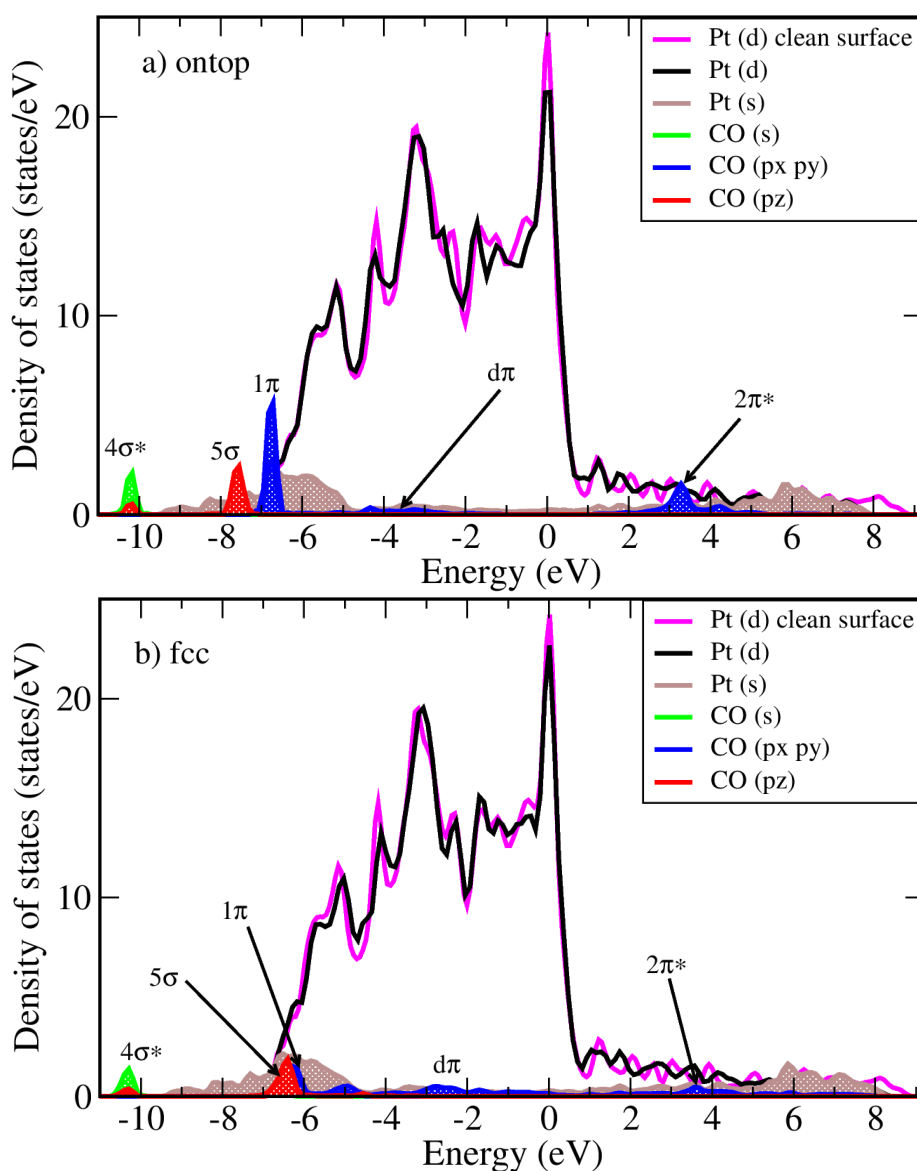

Figure 8.3: Projected electronic density of states of CO adsorbed on a 2x2 slab surface (a) ontop and (b) fcc sites. The various colored lines show projections on the d and s orbitals of Pd atoms as well as $4\sigma^*$, 1π, 5σ and $2\pi^*$ orbitals of CO. The line with magenta color correspond to the adsorbate free surface d orbital projection. The Fermi level is located at 0 eV.

towards Fermi level, as shown in black line. The magenta color represent pDOS of Pd d-band for the clean surface. The 5σ (HOMO) orbital is located below the 1π orbital. The 1π and 5σ orbitals lie below the d-band in both on-top and fcc sites, which is not the same at Pt

surface. Similar to what is observed at Pt surface the non-bonding $d\pi$ orbital is developed in the energy range between -4 to -2 eV, but not as intense as in the case of Pt. It has been argued that the $d\pi$ orbital is created from mixed contribution of 1π and $2\pi^*$ after back donation [99]. The 5σ orbital peak remains unperturbed even in the fcc site adsorption, suggesting the forward donation σ to d-band is weak. Petersson et al. [157] has been pointed out that the σ donation can be Pauli repulsion character for high d-occupancy transition metals. This argument holds true for the present work as d-band of Pd is fully occupied d^{10}. The other evidence for this weak interaction is the 5σ orbital peak remain unchanged (not broaden) and the d-band positioned way above it. On the other hand, even though the peak is not intense, the $2\pi^*$ orbital in the energy range between 2 to 5 eV is still noticeably visible. The relative depletion of $2\pi^*$ orbital indicates the presence of strong back donation. Thus, the surface chemical bond is obtained from the balance between the repulsive character from σ channel and attractive nature of π system and the adsorbate electronic structure involves re-hybridization during adsorption process. As evidenced from the experimental work [117], the magnitude of repulsive and attractive interactions can be different depending on the adsorption site. This give a reason for CO forms different surface coordination structure, i.e, on-top, bridge and hollow sites. The π-bond is found to be strong at high coordination sites, which is manifested with increasing of $d\pi$ orbital peak and increasing of 1π polarization. In general, upon bonding to the metal surface the CO internal bonding becomes weak by re-hybridization of 1π and $2\pi^*$ orbitals. This finally results in increase in C-O bond length and decrease the internal CO stretching frequency.

CO bonding on Pd_{79}

A similar pDOS analysis has been made for Pd_{79} for the same site CO adsorption as has been done on Pt_{79}. What is different here is that the two distinct peaks sustain to retain even at fcc site with a broad peak at -6 eV. If we compare the Pd_{79} with the corresponding slab model, two peaks appear around -7 eV and 5σ and 1π orbitals exist as degenerate. This behavior was observed also on Pt_{79}. The overall other features are very similar to the Pd slab model and all the explanations that have been given above should equally describes CO bonding on Pd_{79}.

To sum up, a stronger back-donation is obtained at fcc site than on-top site for both Pt slab and Pt_{79}, which can be seen from depleted $2\pi^*$ and overlap of 5σ and 1π. On Pt_{79}, unlike to Pt slab, the 5σ and 1π orbitals as degenerate state. Moreover, stronger σ and π orbital hybridization is observed in case of Pt_{79} compared to slab model. For Pd, weak forward donation σ to d-band is determined due to that fact that d-band of Pd is fully occupied. However, the back-donation is strong. In general, the extent of the attractive and repulsive interaction can be different on different adsorption sites and surfaces.
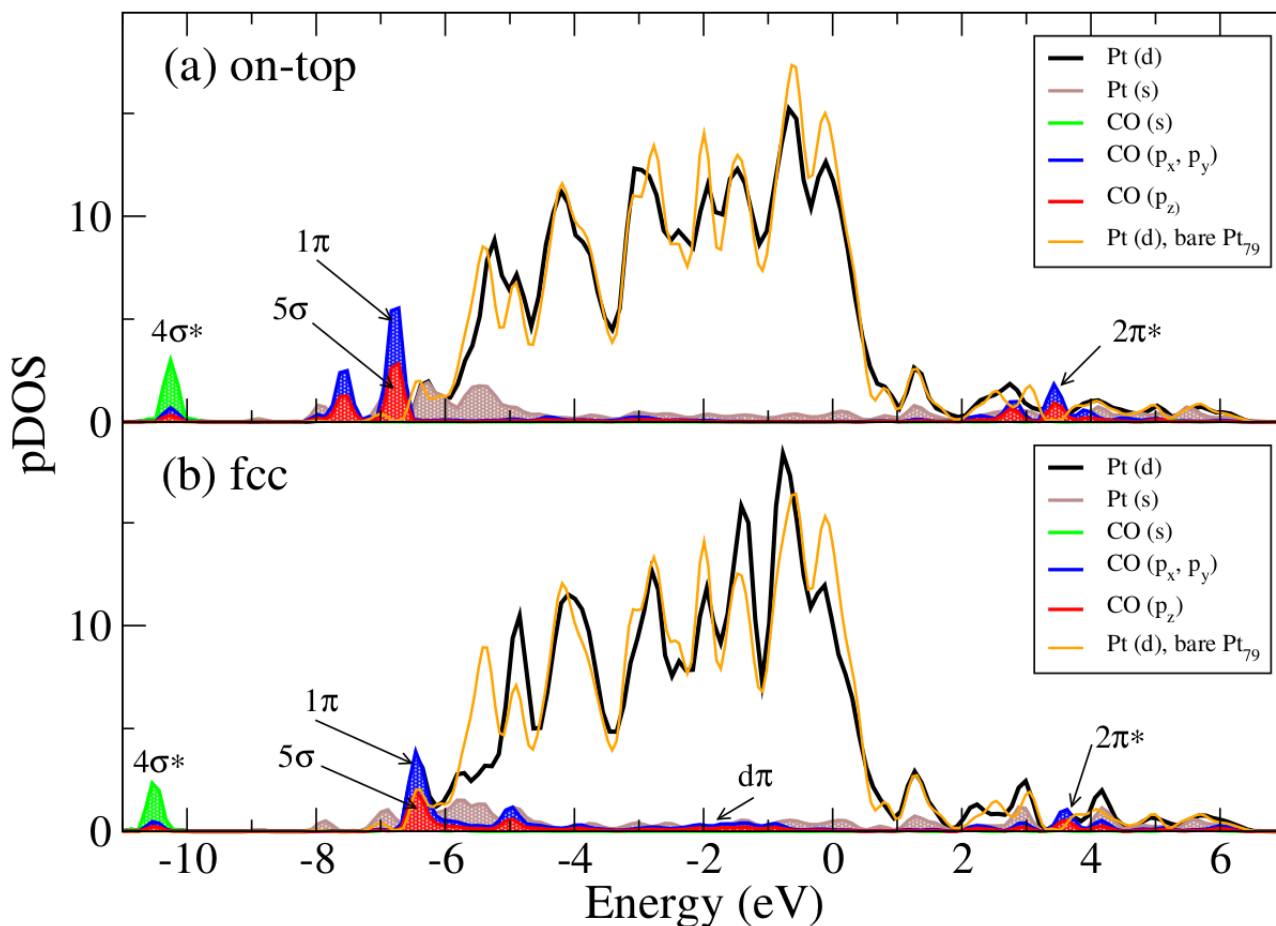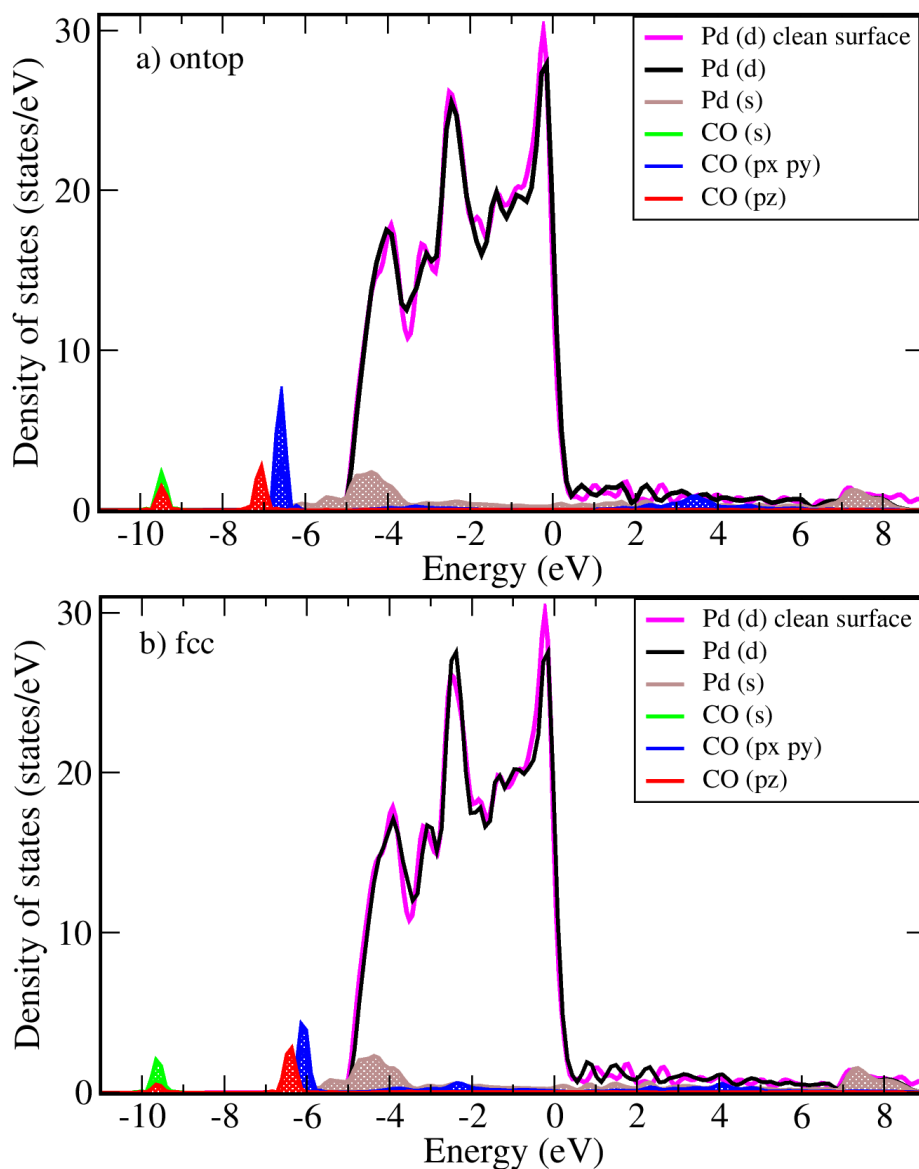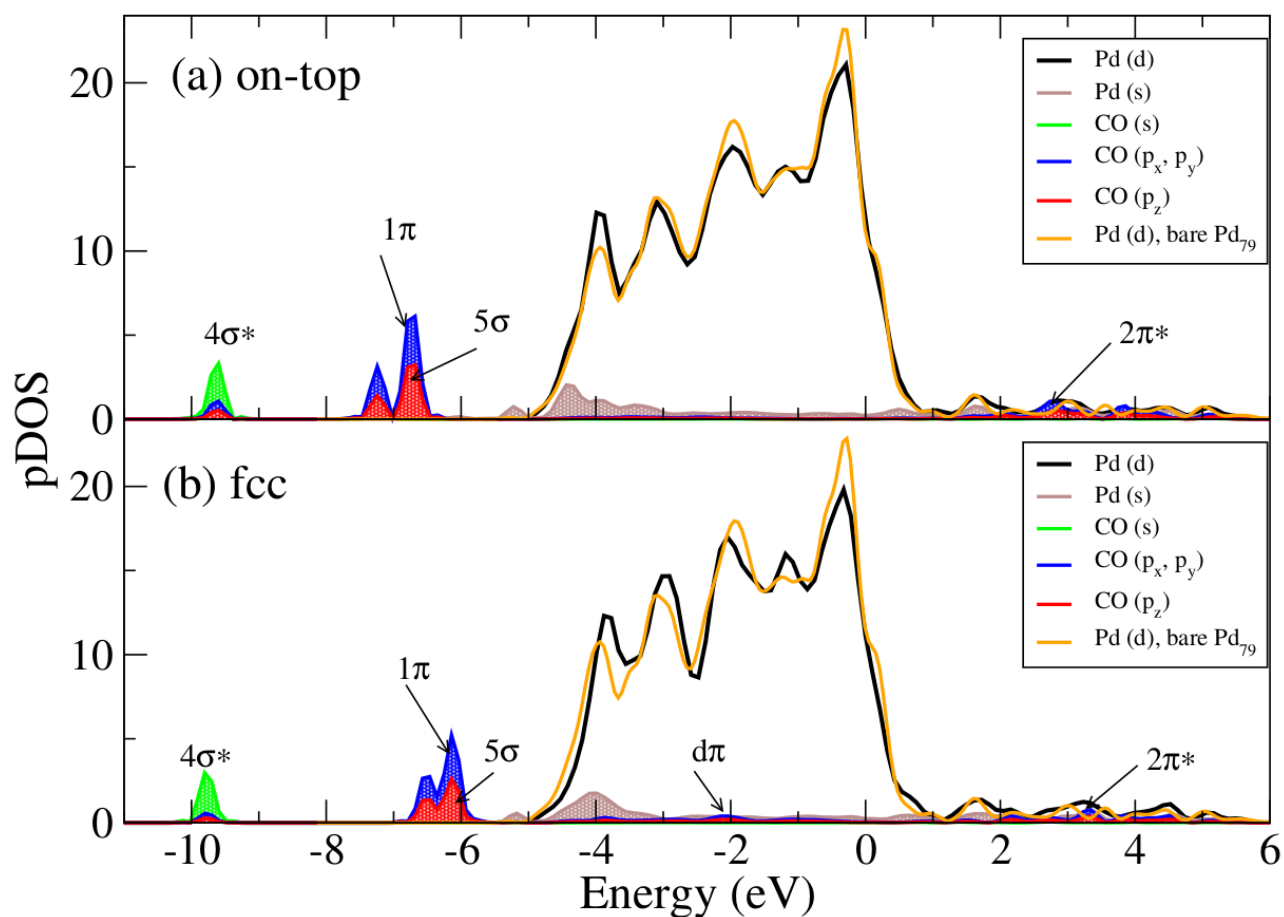
Figure 8.4: Projected electronic density of states of CO adsorbed on Pd_{79} surface (a) ontop and (b) fcc sites. The various colored lines show projections on the d and s orbitals of Pd atoms as well as $4\sigma^*$, 1π, 5σ and $2\pi^*$ orbitals of CO. The line with orange color correspond to the adsorbate free Pd_{79} d band projection. The Fermi level is located at 0 eV.

8.2 CO adsorption on Pt and Pd model catalyst

Generalized coordination number and d-band center descriptors have been considered in this work for analysis of CO and oxygen adsorption energy at various nanoparticles and slab surface. However, d-band center cannot be applicable for description of adsorption energy at different adsorption sites for the same metal surface and the same adsorbate. This is because d-band center model is developed to determine surface reactivity of different metals surfaces in terms of their electronic structure [110]. On the other hand, generalized coordination number ($\overline{CN}$) can provide better description for adsorption energy at various adsorption sites. For example, Figure 8.5 shows a monotonic correlation of $\overline{CN}$ with adsorption energy of CO at on-top sites of the same system. The correlation would seem also predictable, in which lower coordinated sites (corners and edges) show higher adsorption energies than the higher coordinated terrace sites. Thus, in the present work the $\overline{CN}$ descriptor is chosen for adsorption energy analysis at pure Pt and Pd model catalysts. For oxygen coverage study, d-band center has shown very good correlation with average adsorption energy, so that it is employed for coverage analysis.

8.2.1 Geometric structure of adsorbate on the surface

It is very common that to use DFT for geometric structure determination and many reliable results have been reported in previous studies. For adsorption complex, since invaluable information can be obtained about the interaction, analyzing the geometric changes might be helpful. Regarding CO adsorption on TM surface, in all studied surfaces CO molecule adsorbs vertically upward position with carbon atom bonded to the surface. In Table 8.6, the C-O bond length ($d_{\text{C-O}}$) variation on various adsorption sites of Pt_{201} and Pd_{201} nanoparticles and slab model is given. In addition, the Pt-C and Pd-C bond distance is illustrated for both the 201 atom nanoparticle and slab model. As already mentioned, the degree of back-donation vary for the different adsorption sites, indicating that the highest back-donation is observed for the three-fold hollow site. Up on adsorption, the $d_{\text{C-O}}$ length is increased when going from one-fold to 3-fold adsorption site and the same holds true for $d_{\text{M-C}}$. The calculated gas phase CO bond length is 1.144 Å.

For the on-top sites, on average the $d_{\text{C-O}}$ found is 1.61 Å for both Pt and Pd. However, slight difference of $d_{\text{C-O}}$ is observed for the various coordination site ($\overline{CN}$), indicating that as the $\overline{CN}$ increases, the $d_{\text{C-O}}$ decrease. As can be observed in Table 8.6, for Pt the longest $d_{\text{C-O}}$ is calculated 1.163 Å at $\overline{CN}$ 4.25 and the shortest 1.158 Å at $\overline{CN}$ 7.50. On the other hand, $d_{\text{C-O}}$ on Pd shows no significant variation with increase in $\overline{CN}$, in which 1.161 and 1.159 Å is observed for low and high $\overline{CN}$ values, respectively. Analogously, the Pt/Pd-C bond length, decreases with $\overline{CN}$ and the $d_{\text{Pd-C}}$ found to be slightly longer than the $d_{\text{Pt-C}}$ distance. Turning to the bridge (2-fold) site, the $d_{\text{C-O}}$ is obtained in the range 1.183-1.185 Å for both Pt and Pd, which is ≈ 0.02 Å longer than the on-top (1-fold) site. The metal-carbon distance ($d_{\text{M-C}}$), is also elongated in comparison to the on-top site by ≈ 0.17 Å for Pt and ≈ 0.13 Å for Pd. Moreover, the Pt-C distance is somewhat longer than the Pd-C, which is in contrast to the on-top site observed

Table 8.1: Three-fold, on-top and bridge sites CO adsorption on truncated octahedron nanoparticles (M_{201}) and slab surface. The outer(inner) values of E_{ads}, d_{M-C}, d_{C-O} and ω correspond to Pt(Pd) metals.

M_{201}

on-top

$\overline{CN}$	E_{ads} (eV)	d_{M-C} (Å)	d_{C-O} (Å)	ω (cm^{-1})
4.25	2.14(1.59)	1.847(1.862)	1.163(1.161)	2075(2035)
5.16	2.03(1.53)	1.839(1.857)	1.162(1.161)	2074(2055)
6.33	1.83(1.48)	1.835(1.856)	1.161(1.161)	2079(2056)
6.95	1.72(1.43)	1.830(1.845)	1.159(1.159)	2105(2070)
7.50	1.56(1.35)	1.829(1.849)	1.158(1.159)	2106(2075)

bridge

$\overline{CN}$	E_{ads} (eV)	d_{M-C} (Å)	d_{C-O} (Å)	ω (cm^{-1})
4.44	2.01(1.96)	2.010(1.973)	1.185(1.183)	1906(1887)
5.16	1.80(1.83)	2.021(1.984)	1.184(1.184)	1914(1880)
5.55	1.99(1.85)	2.012(1.982)	1.184(1.185)	1908(1879)
6.94	1.88(1.86)	2.001(1.982)	1.184(1.183)	1927(1889)

3-fold holow

$\overline{CN}$	E_{ads} (eV)	d_{M-C} (Å)	d_{C-O} (Å)	ω (cm^{-1})
4.59(fcc)	1.81(2.04)	2.120(2.055)	1.197(1.197)	1816(1799)
5.50(fcc)	1.77(1.99)	2.201(2.061)	1.193(1.195)	1844(1804)
6.41(fcc)	1.97(2.07)	2.090(2.054)	1.198(1.196)	1821(1816)
5.09(hcp)	1.84(2.03)	2.101(2.056)	1.198(1.196)	1815(1799)
6.95(hcp)	1.91(2.06)	2.090(2.056)	1.196(1.195)	1834(1818)

slab model

$\overline{CN}$	E_{ads} (eV)	d_{M-C} (Å)	d_{C-O} (Å)	ω (cm^{-1})
7.5(on-top)	1.68(1.41)	1.841(1.856)	1.159(1.159)	2014(2044)
6.95(fcc)	1.79(1.94)	2.116(2.074)	1.193(1.190)	1758(1811)

Experiment

—	E_{ads} (eV)	d_{M-C} (Å)	d_{C-O} (Å)	ω (cm^{-1})
Pt (on-top)	1.37[99]	1.85±0.01 [158]	1.15±0.05 [158]	2065-2090 [100]
Pd (fcc)	1.42[99]	2.04±0.05 [158]	1.15±0.05 [158]	1813-1836 [100]

result. As for 3-fold sites, the value of $d_{\text{C-O}}$ is determined in the range 1.193-1.197 Å for both Pt and Pd. Thus, for both Pt and Pd the $d_{\text{C-O}}$ at 3-fold sites are longer than on-top by ≈ 0.037 Å and bridge by ≈ 0.014 Å. Similarly, the $d_{\text{M-C}}$ is increased to some extent compared to the on-top and bridge for both metals. The next question is how C-O bond length on metal surface vary with adsorption energy and vibrational stretching frequency of CO. Table 8.6 shows the adsorption energy and CO stretching frequencies with the corresponding C-O bond length at various adsorption sites. Overall, as C-O bond length variation with $\overline{\text{CN}}$ is very small, there is no clear systematic relation between C-O bond length and adsorption energy. However, one particular case, for Pt on-top site adsorption there is a monotonic increase with the C-O bond length, implying that the CO bond is weakened on gaining charges from the metal through the back-donation channel. Likewise, the correlation of C-O bond length and stretching frequency is complex.

As it can be clearly seen in Table 8.6, generally speaking, the calculated geometric parameters and the stretching frequencies are found to be in the experimental range while the adsorption energy is overestimated. This more stable prediction of adsorption energies than they are experimentally is typical case for PBE and other semi-local functionals [122, 159]. Comparing the slab model adsorption energies with the experimental data shows a difference of about 0.3 eV for on-top site adsorption on Pt and very small difference for fcc site adsorption of Pd (about 0.04 eV). Here, it might not be feasible to compare the given experimental data with nanoparticle result due to the fact that the experiment was based on single crystal surface. However, it could be possible to compare the most coordinated site adsorption energy at the center of (111) facet, for example, $\overline{\text{CN}}$ 7.5 for on-top site on Pt and $\overline{\text{CN}}$ 6.41 for fcc site on Pd. In doing so, for Pt on-top site relatively better agreement is observed with difference of 0.2 eV. But for fcc site adsorption on Pd nanoparticle the difference is about 0.6 eV. A more detailed result of change of adsorption energy with particle size, shape and adsorption site will be given in the next sections.

8.2.2 Effect of adsorption site and shape

Here, one important question is how does the surface structure (coordination number) of the adsorption site affect the bond strength between the surface and CO adsorbate. Table 8.6 presents the calculated adsorption energy at various coordination number for model systems of 201 atom nanoparticle and extended surface. The coordination numbers correspond to corner, edge and terrace sites in which the lowest $\overline{\text{CN}}$ represent the corner site and the large $\overline{\text{CN}}$ values are at terrace sites. For the on-top sites, the overall trend observed is adsorption energy increases with decrease in coordination number, i.e. corner and edge sites are more favored than terrace sites. However, given that the adsorption energy variation is very slight for the various $\overline{\text{CN}}$, for bridge and 3-fold hollow sites no clear trend is observed. For CO adsorption on Pd (111) extended surface, 3-fold hollow site is known to be energetically favorable site based on both experimental measurements and periodic slab model calculations [160, 161]. Thus, the experiment and the theory findings are in agreement for CO adsorption on Pd metal
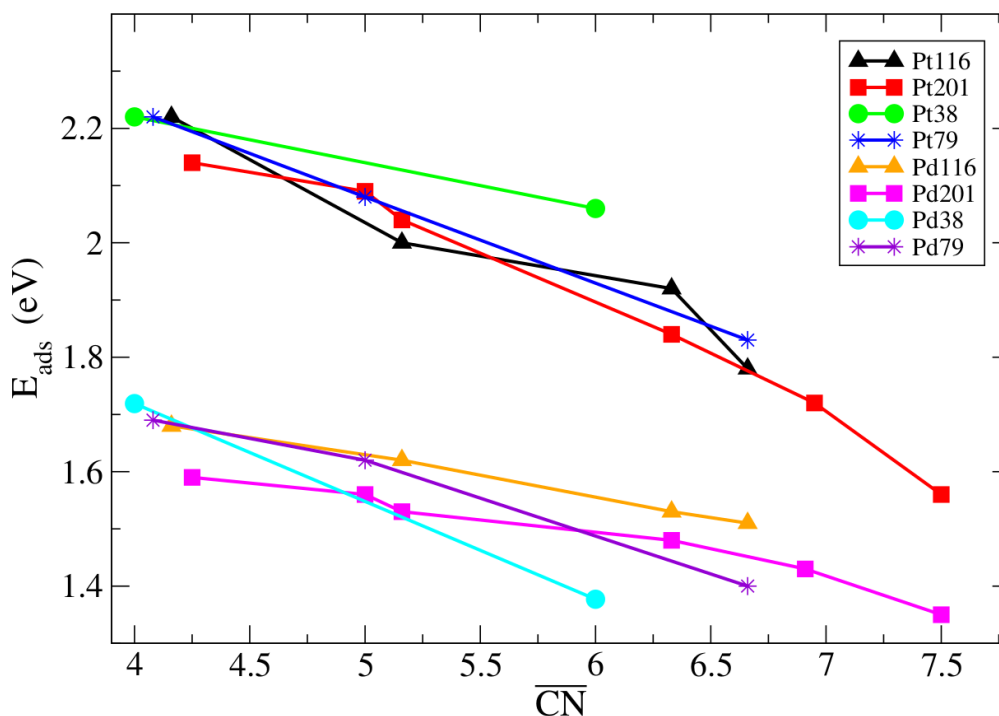
Figure 8.5: On-top site adsorption of CO on truncated octahedron nanoparticles of Pt and Pd metals at various site and size.

surface. On the other hand, based on experimental investigation the preferred CO adsorption site on Pt(111) surface is on-top site, while DFT predicts the 3-fold site being energetically favored [111]. A recent DFT study reported that in the case of nanaparticles the wrong site preference does not occur on Pt for lower coordinated sites (edges and corners) [125, 126]. To investigate the adsorption energy of CO on Pt and Pd metals, various shapes and sizes of nanoparticles are considered in the following sections. To see the effect of shape, various shapes of model nanoparticles have been selected which can be grouped into truncated octahedron, cuboctahedron and regular octahedron types.

Truncated Octahedron Nanoparticles

Truncated octahedral nanoparticles comprised of (111) and (100) facets and the dominant portion is (111) facet. For this class of particles various sizes are chosen, i.e., with 38, 79, 116 and 201 atoms for both Pd and Pt metals. All possible non-equivalent adsorption sites (coordination numbers) were investigated for the 1-fold (on-top), 2-fold (bridge) and 3-fold (fcc, hcp) bonding sites. Figure 8.5 shows on-top adsorption of CO on Pt and Pd nanoparticles of different size at various adsorption sites. Interestingly, the adsorption energy (E_{ads}) of CO on Pt and Pd surface is clearly different for the two metals and the general trend with increase in $\overline{CN}$ is remarkably very similar. Thus, for the on-top site regardless of size, E_{ads} of CO on Pt is always higher than on Pd. Apparently, higher E_{ads} is observed at under-coordinated sites $\overline{CN}$ value of less than 5.5. The $\overline{CN}$ value 4.0 represent the corner sites and between 5 and 5.5 correspond to the edge sites. The terrace sites represented by $\overline{CN}$ value of ≥ 6. For size M_{116} and M_{201} at terrace site, $\overline{CN}$ 6.33 is found at center of (100) facet. From the graph we can

note that the difference in E_{ads} between Pt and Pd progressively decreases as $\overline{CN}$ increases. The maximum difference is calculated at the corner and edge sites ≈ 0.5 eV and at the terrace sites 0.4 to 0.2 eV with the exception of size 38 in which relatively high difference is observed. As might have been expected, the adsorption energy decreases in the order corner > edge > terrace site. It should be noted that E_{ads} difference between corner and terrace sites can be significantly large. However, this is more pronounced in the case of Pt than Pd. For example, for Pt_{201} 0.58 eV difference is calculated, but for Pd_{201} small difference, 0.24 eV is obtained and the same difference is determined for the other sizes. Taken together, the results suggest that adsorption energy is highly influenced by the local surface geometric structure.

Turning now to the size effect on the adsorption energy, the result shows that there is no simple relation between the cluster size and adsorption energy at least at the low coordinated sites (corners and edges). However, if one takes E_{ads} at terrace site center of (111) facet, a linear correlation of size and adsorption energy can be obtained for Pt nanoparticles. Figure 8.6 left panel (a) shows a linear fit of E_{ads} of various size with the corresponding high $\overline{CN}$ site at (111) facet and compared with the (111) slab model. Recently, similar work has been reported for the same system at (111) facets using PW91 density functional [162] and remarkable agreement is obtained which is depicted in Figure 8.6 (b) the right panel. On one hand, as this case is
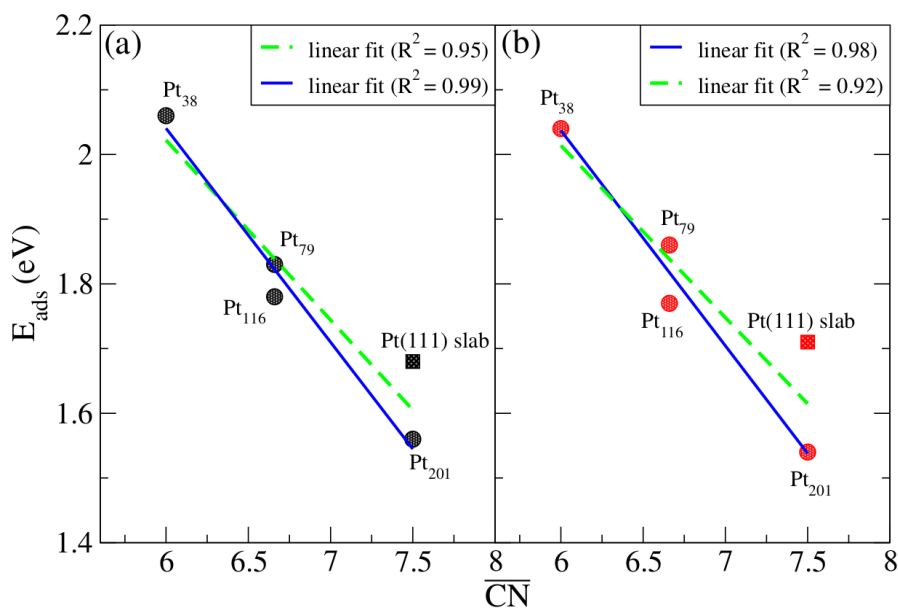
Figure 8.6: On-top site adsorption energy of CO on truncated NPs of Pt(111) facet terrace (high coordinated site) at various size (filled circle) and slab model (filled square). The left panel (a) shows calculated results in this work and right panel (b) shows the reported literature for the same system [162]. The linear fit of adsorption energy with $\overline{CN}$ and hence, size are shown in solid blue line(only NPs) and green dotted line (both NPs and slab model).

clearly demonstrated, the linear decrease in E_{ads} with size is expected to converge eventually to the bulk result and that will be the point where finite size effect vanish. The experimental measured adsorption energy on single crystal surface is 1.37 eV [111] and 1.56 eV is calculated for Pt_{201} which is the largest size considered in this work. An implication of this is possibly that already Pt_{201} size range is the finite size limit, bearing in mind that GGA functionals slightly

overestimate the E_{ads}. The linear fit in blue solid line is only for NPs and the green dotted line is for both the NPs and slab model. As evidenced by the regression coefficient (R^2) value, better linear fit is obtained when only nanoparticles taken for correlation.

As already mentioned above, according to experiment the preferred site for CO adsorption on Pt surface is on-top, while 3-fold site is favored on Pd surface. Figure 8.7 presents CO adsorption energy at on-top (upper panel) and 3-fold (lower panel) sites for M_{201}. The overall trend of CO adsorption energy variation with $\overline{CN}$ for Pt and Pd metals is quite similar to each other. It can be seen that on-top site CO E_{ads} on Pt surface is always larger than on Pd surface and vice versa is determined for 3-fold sites. These result can be taken as a justification for the experimental finding of Pt favors on-top and Pd 3-fold sites. In the following I will address the claim [111] that GGA functionals fail to predict the correct CO adsorption preference on Pt surface. The current finding suggested that on Pt NPs the wrong preference has existed only on terrace site, i.e. when $\overline{CN}$ is larger than 6 in which 3-fold site is favored. Conversely, on-top site is preferred at low coordinated sites ($\overline{CN} < 6$) that is at corners and edges, this is clearly shown in Figure 8.7. Thus, in the present calculations using the PBE density functional no site preference problem occur at defect sites (corners and edges). On the other hand, in the case
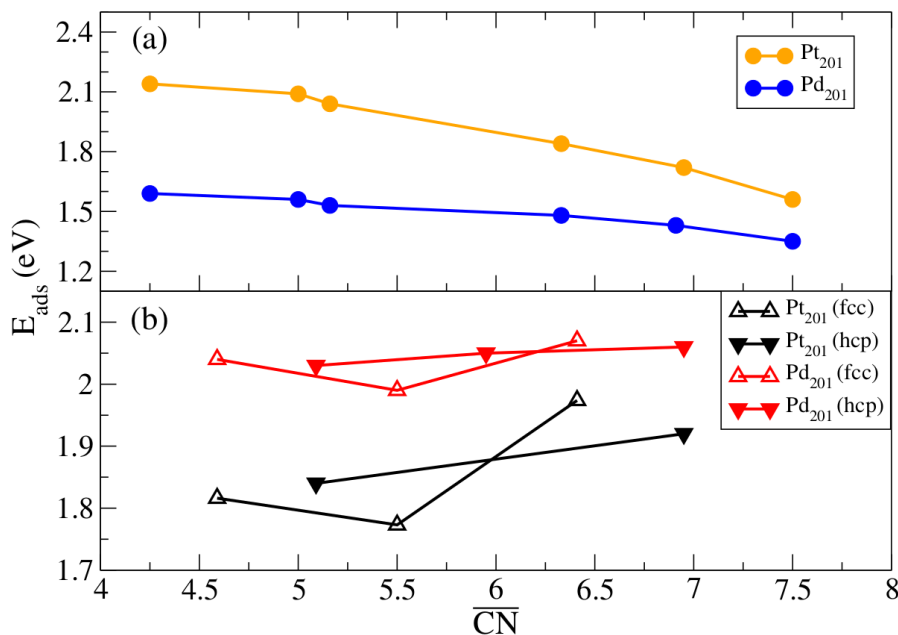
Figure 8.7: CO adsorption energy on Pt_{201} and Pd_{201} (a) for the on-top sites and (b) 3-fold sites.

CO adsorption on Pd, 3-fold sites E_{ads} are always significantly larger than on-top sites with a minimum difference of ≈ 0.5 eV and this comply with the experimental result [160]. The other striking behavior emerging from 3-fold site is that unexpectedly E_{ads} would seem to be large at highly coordinated site. Furthermore, the preference between fcc and hcp sites cannot be understood clearly as the two sites have very close E_{ads}. Moreover, the bridge site CO E_{ads} (data not shown) fall somewhere between on-top and 3-fold site and no clear trend of change in E_{ads} is observed. However, the corner and edge sites E_{ads} of the on-top site is higher than the bridge sites.

Regular Octahedron Nanoparticles

Regular octahedron NPs are constructed entirely from (111) facets with eight (111) facets, 12 edges and six vertices. For these class of NPs three series of sizes have been selected: M_{44}, M_{85} and M_{146}. Figure 8.8 shows fcc and on-top site adsorption of CO on Pt_{146} and Pd_{146} surfaces. As evidenced in the graph, the results on fcc and on-top sites for M_{146} shares a number of similarities to the truncated NPs of size M_{201}, see Figure 8.8 and Figure 8.7. As anticipated, the on-top site E_{ads} decreases as the coordination number increases for both Pt and Pd which is quite similar to the observed result at M_{201}. E_{ads} of CO on Pt is always larger than on Pd for the on-top sites and the inverse is calculated for the fcc site that E_{ads} is large at Pd surface. Analogously to what is observed on the truncated nanoparticles, the on-top site E_{ads} close to the edges and vertices are higher than the 3-fold sites. However, on the terrace, 3-fold sites E_{ads} are larger than the on-top sites. Moreover, again terrace sites seem more favored than near edges and vertices for fcc sites.
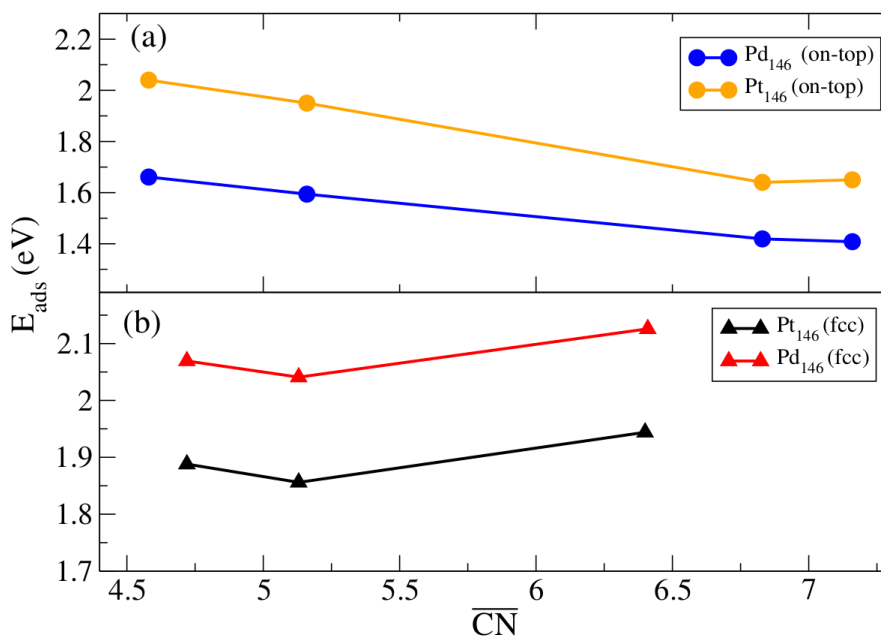
Figure 8.8: CO adsorption energy on Pt_{146} and Pd_{146}.

If we now turn to bridge site CO adsorption on this class of nanoparticles, at terrace of Pd, bridge sites turn out to be unstable (moves to nearby 3-fold site on course of geometry optimization) and only edge site adsorption is favorable. This is peculiar to the Pd surface and it has not observed at Pt surface. Figure 8.9 shows bridge site adsorption of CO on Pt_{85} (black line) and Pt_{146} (red line) NPs. As might have been expected edge and vertices site are found to have relatively large E_{ads}. It should be noted that bridge site E_{ads} at center of (111) facet, i.e. at terrace, increases with coordination number (Figure 8.9) and such feature was observed at 3-fold site. Furthermore, E_{ads} of Pt_{85} determined to be larger than Pt_{146} which is particularly more pronounced at higher $\overline{CN}$.

To check whether or not the adsorption energy at these NPs size are converging to the extended (111) ideal surface, the adsorption site at the center of (111) facet has picked and the E_{ads} result compared with the calculated extended surface (see Figure 8.10). Since according
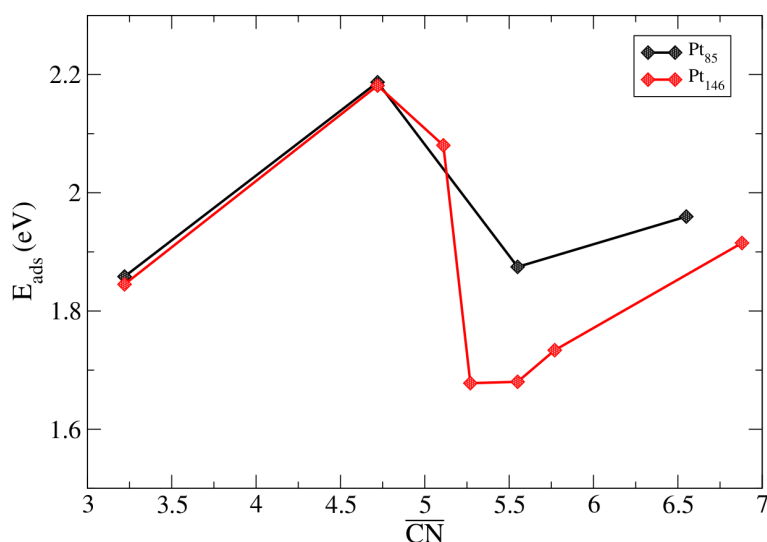
Figure 8.9: CO adsorption energy on various bridge sites of Pt_{85} and Pt_{146} NPs.

to experiment CO favors on-top site at Pt(111) and 3-fold sites at Pd(111) surface, only those sites are chosen accordingly. As can be seen from Figure 8.10, on both cases (a) and (b) the
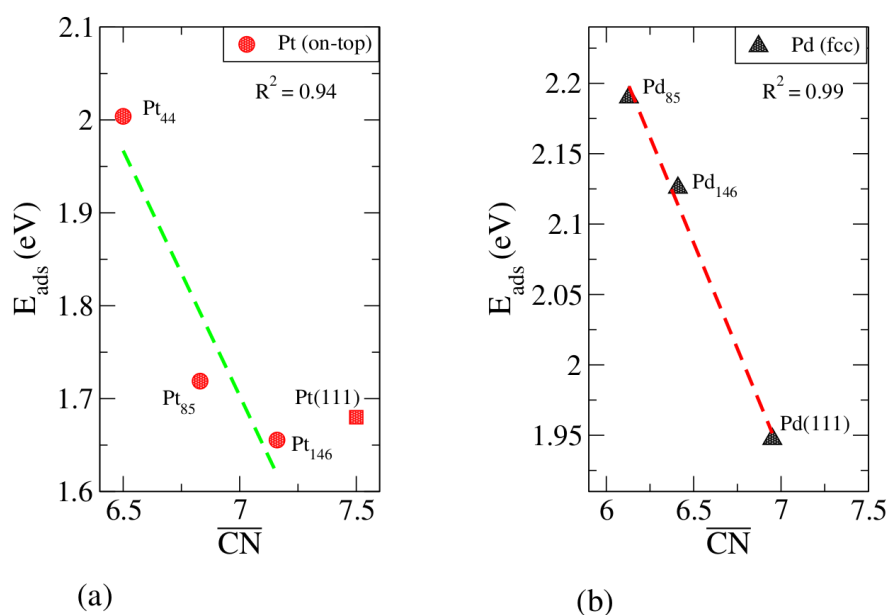
Figure 8.10: CO adsorption energy on regular octahedron NPs (a) on-top site adsorption at terrace of Pt for various size (filled red circle) and pt(111) extend surface (filled red square). The green dotted line indicate the linear fit for the NPs with regression coefficient (R^2 =0.94) (b) fcc site adsorption at terrace of Pd for various size and Pd(111) extended surface. The red dotted line shows the linear fit for NPs and slab model with regression coefficient (R^2 =0.99).

E_{ads} is decreasing monotonically with size. However, on-top site adsorption of CO on Pt(111) seems converging fast to the slab model with a linear fit coefficient of R^2 =0.94. Indeed, the experimental measured result for on-top site adsorption of CO at the single crystal surface (1.37 eV) is lower than the calculated result, but it is known that GGA functionals overestimate the binding strength. Similarly, E_{ads} of CO on fcc site of Pd is converging even more steeply than what is observed on Pt on-top site with linear fit coefficient of R^2 =0.99. However, the calculated adsorption energy of the slab surface is 1.94 eV which is again higher than the experimental

value of 1.47-1.54 eV at low coverage (0.25 ML) on single-crystal Pd(111) surface.

In general, for regular octahedron Pt NPs the highest E_{ads} calculated at bridge-edge sites and followed by top-edge site. Thus, the adsorption energy ordering follows: bridge-edge > top-edge > fcc-terrace > bridge-terrace > hcp-terrace > top-terrace. On the other hand, on Pd surface fcc site E_{ads} determined to be always higher than other sites. The bridge sites are not favorable for CO adsorption on this class of NPs except at edge locations, and hence, CO diffuse to the vicinity 3-fold site on courses of geometry optimization. Consequently, E_{ads} on Pd decrease in the following order: fcc > hcp > bridge-edge > top site.

Cuboctahedron Nanoparticles

Cuboctahedral nanoparticles possessing eight triangular (111) and six square (100) facets with the major portion from (100) facet. Two sizes Pt_{55} and Pt_{147} structures are selected and CO adsorption is investigated.

Table 8.2: Three-fold, on-top and bridge sites CO adsorption energies (E_{ads}) on Pt and Pd cuboctahedron nanoparticles. The outer(inner) values of E_{ads} correspond to Pt(Pd) metals.

M_{147}

on-top $\overline{CN}$	E_{ads} (eV)	bridge $\overline{CN}$	E_{ads} (eV)	3-fold hollow $\overline{CN}$	E_{ads} (eV)
3.33	2.33 (1.72)	3.83	— (1.98)	4.04 (hcp)	1.90 (—)
5.00	2.18 (1.64)	4.72	— (2.15)	4.41 (fcc)	1.63 (1.89)
6.50	2.13 (1.52)	5.33	1.78 (—)	5.18 (hcp)	1.98 (2.16)
6.51	1.66 (1.48)	5.50	2.23 (1.94)	4-fold	1.86 (—)
		6.44	2.39 (1.97)		

Pt_{55}

on-top $\overline{CN}$	E_{ads} (eV)	bridge $\overline{CN}$	E_{ads} (eV)	3-fold hollow $\overline{CN}$	E_{ads} (eV)
3.33	2.47	3.61	2.21	3.41 (fcc)	1.48
4.66	2.23	5.16	2.44	3.77 (hcp)	2.07
6.33	2.14				

The calculated E_{ads} on Pt are the highest for all the structures investigated in the present work, see Table 8.2. The highest adsorption energy was determined on bridge site of (100) terrace and on-top site of corner point that connects a triangular (111) facet and square (100) facet. As we can see from Table 8.2, the highest bridge site E_{ads} at Pt_{147} is 2.39 eV and at Pt_{55} 2.44 eV. Analogously, the largest on-top site E_{ads} at Pt_{147} is 2.33 eV and at Pt_{55} 2.47 eV. On Pt_{147}, the lowest bridge site and on-top site E_{ads} have been obtained on (111) facet, at $\overline{CN}$ 5.33 and 6.51, respectively. Overall, it is observed that on-top and bridge sites E_{ads} is substantially large compared to other shapes of NPs considered in this work. Nevertheless, unlike bridge and on-top sites, 3-fold sites adsorption energy does not show unusual features. In fact, the (111)

facet is comparably small so that all 3-fold sites are directly neighboring the edge and corner sites. We have seen from the other NPs that CO adsorption on 3-fold terrace sites are more favored than on-top terrace sites, i.e. when $\overline{CN}$ is larger than 6, see also Figure 8.7 and 8.8. It should be pointed out that hcp sites have higher E_{ads} than fcc site for both Pt_{55} and Pt_{147}. In addition, E_{ads} of hcp sites are larger than bridge and on-top sites at center of (111) terrace which is in agreement with the previous study on Pt_{147} [125].

The calculated adsorption energies of Pd_{147} are in general comparable to the other Pd NPs. However, on-top-corner determined to have the highest E_{ads} compared to other on-top sites of all Pd NPs studied. Moreover, 3-fold hollow sites E_{ads} are larger than the corresponding 3-fold hollow sites on Pt which is consistently observed regardless of size and shape for NPs studied in this work.

8.2.3   Nanoparticle size effect on CO adsorption energy

So far we have seen CO adsorption at different adsorption sites for Pt and Pd nanoparticles of various shapes. Here, to check the variation of adsorption energy as a function of nanoparticle size, CO adsorption energies of all sites and nanoparticles presented above are evaluated by means of box-plot statistical analysis. This kind of statistical representation of the data can summarize the overall data distribution. Figure 8.11 shows box-plot analysis of adsorption energies at various size. The box-plot helps to characterize the adsorption energy distribution for each size. For a given NP size, all adsorption energies are collected regardless of site. Then, the adsorption energies are grouped into four quartiles. The zigzag line that divides the box is the median which marks the mid-point of data. Half of the data (50%) is above the median and the other half is below the median. The lower quartile (25%) located below the box represents the lowest 25% adsorption energy out of all adsorption energies. The next 50% of the adsorption energies are represented in the green box. The upper quartile located above the box represents the highest 25% adsorption energies. As clearly seen from the result, it would
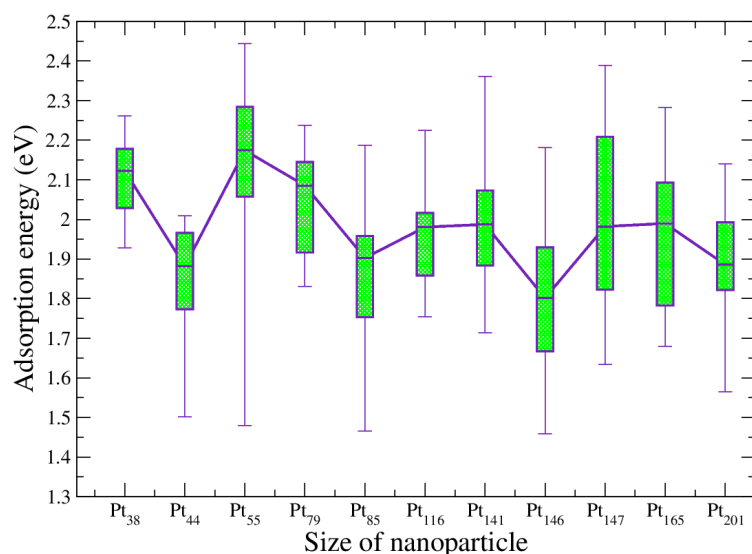
Figure 8.11: CO adsorption energy on Pt nanoparticles of various size.

seem that there is no clear correlation of adsorption energy and nanoparticle size. Rather the nanoparticle shape has a noticeable effect, for example, the regular octahedron nanoparticles (Pt_{44}, Pt_{85} and Pt_{146}) have comparatively lower median, and hence, lower adsorption energies. As already described above, this class of NPs have only (111) facet, hence limited number of lower coordinated sites are available. Moreover, the most spread data distribution is observed for cuboctahedron particles (Pt_{55} and Pt_{147}). The long lower whisker at Pt_{55} indicates that the adsorption energies within the lower quartile vary significantly. The highest adsorption energies is calculated at Pt_{55}. The adsorption energies on truncated octahedron nanoparticle (Pt_{38}, Pt_{79}, Pt_{116} have the least scattering detected in the short boxes and whiskers. Overall, the calculated CO adsorption energies at the studied Pt nanoparticles lie between 1.4 to 2.5 eV. Furthermore, it seems that adsorption site and nanoparticle shape have more influence on the adsorption energy than the nanoparticle size has.

Similar analysis has been carried out for CO adsorption on Pd nanoparticles. Figure 8.12 presents box-plot analysis of adsorption energies at various size. Generally, a similar analysis result is obtained, however, the adsorption energies are more strongly scattered at Pd. This can be easily seen especially by comparing truncated octahedron NPs (38, 79, 116 and 201). The same is true for regular octahedron NPs (44, 85 and 146). The overall CO adsorption
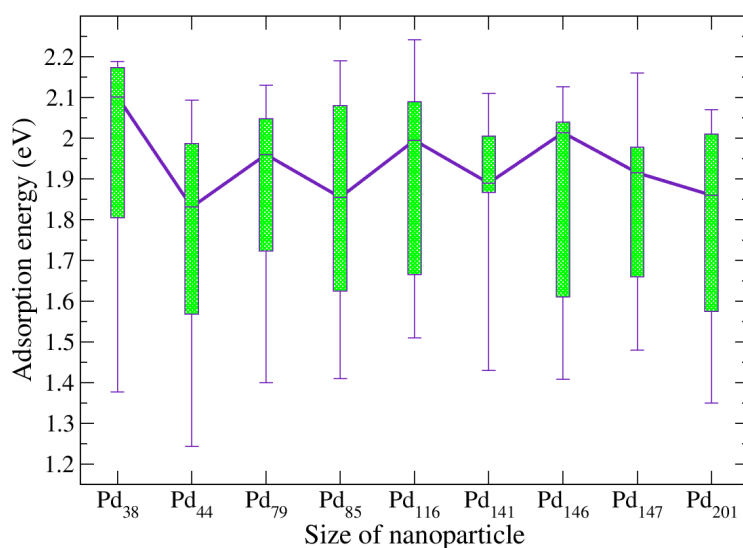
Figure 8.12: CO adsorption energy on Pd nanoparticles of various size.

energies lie in the range 1.25 to 2.25 eV and the median in the 2.1 to 1.85 eV. Taken together, using a statistical analysis of the available data it is not possible to identify so simple and useful correlation between adsorption energy and nanoparticle size as in the case between adsorption energy and adsorption site type.

8.2.4 CO vibrational frequencies

In this work, CO vibrational spectra at on-top, bridge, and 3-fold sites of Pt and Pd surfaces are found in the ranges 2050-2106 cm^{-1}, 1890-1930 cm^{-1} and 1750-1850 cm^{-1}, respectively. These results comply with the reported experimental and theoretical work [100–104]. Thus, it

is straightforward and clear to recognize whether CO adsorbed on on-top, bridge or 3-fold sites on the basis of stretching frequency. The next questions are how does vibrational spectra of CO vary with size, shape and coordination number of the adsorption sites? Or would it be possible to differentiate CO at lower and higher coordinated site from the CO vibrational spectra? In the present work, CO vibrational frequencies were evaluated for various coordination site and size distribution.
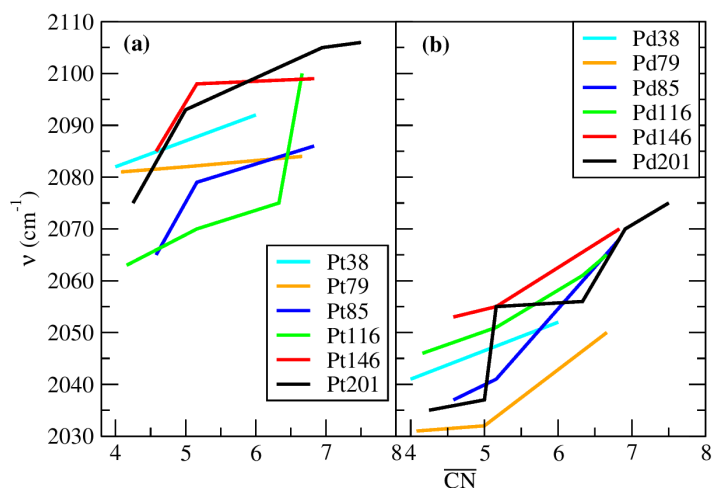
Figure 8.13: The variation of on-top sites vibrational frequency as a function of $\overline{CN}$ (a) on Pt nanoparticles and (b) on Pd nanoparticles.

Figure 8.13 shows change of ν with various coordination number at different on-top sites of Pt and Pd nanoparticles. As can be seen ν varies monotonically with coordination number. The highest vibrational frequencies are at sites with high coordination number which is found at terrace site of (111) and (100) facets for both Pt and Pd. The lowest ν are obtained at low coordination sites, i.e. at corner sites and edge sites lie between the terrace and corner locations. These characteristic variation is found for all nanoparticle sizes. Furthermore, as can be seen, the CO stretching vibration on Pt (a) is slightly higher than on Pd surface (b). The reason for the increase of vibrational frequency with coordination number is associated to decrease in adsorption energy. As already discussed above, the adsorption energy of CO at terrace site was determined to be lower than at lower coordination sites (corners and edges). Figure 8.14 shows the correlation of vibrational frequency with E_{ads} for selected larger nanoparticles. As clearly seen, lower adsorption energies are related to higher CO stretching vibration, these is because at low E_{ads} the Pt–CO bond strength is weak resulting in lower effect on C–O bond strength. These systematic variation of on-top CO adsorption is very helpful to understand the catalyst structure and this is in particular important at Pt surface as CO preferred to adsorb at on-top sites at Pt. Experimental findings have been reported for such monotonic correlation of coordination number with vibrational frequency [105].

Even though monotonic change of vibrational frequencies with E_{ads} and $\overline{CN}$ were obtained for the on-top sites of Pt and Pd, the bridge and 3-fold sites did not show a similar trend. As 3-fold site is the favored site on Pd surface, Table 8.3 shows 3-fold sites E_{ads} and ν with coordination number for the various sites for the selected model structures. It is apparent from

Table 8.3: Three-fold site CO adsorption energies (E_{ads}) and vibrational frequencies (ν) on Pd nanoparticles.

	Pd_{146}	
GCN	E_{ads} (eV)	ν (cm^{-1})
3.04 (fcc)	2.03	1781
4.72 (fcc)	2.07	1792
5.13 (fcc)	2.04	1809
6.41 (fcc)	2.13	1814
6.04 (hcp)	2.01	1806
6.95 (hcp)	2.05	1812

	Pd_{116}	
GCN	E_{ads} (eV)	ν (cm^{-1})
4.13 (fcc)	2.07	1791
5.22 (fcc)	2.08	1800
4.95 (hcp)	2.13	1790
6.41 (hcp)	2.24	1797

	pd_{85}	
GCN	E_{ads} (eV)	ν (cm^{-1})
3.04 (fcc)	2.07	1786
4.72 (fcc)	2.11	1795
6.13 (fcc)	2.19	1794
5.86 (hcp)	2.01	1806

	pd_{79}	
GCN	E_{ads} (eV)	ν (cm^{-1})
4.40 (fcc)	2.06	1795
5.86 (fcc)	2.13	1802
4.45 (hcp)	1.95	1789
5.68 (hcp)	2.01	1798

|	Pd(111) slab	
GCN	E_{ads} (eV)	ν (cm^{-1})
6.95 (fcc)	2.07	1762
7.50 (hcp)	2.05	1760
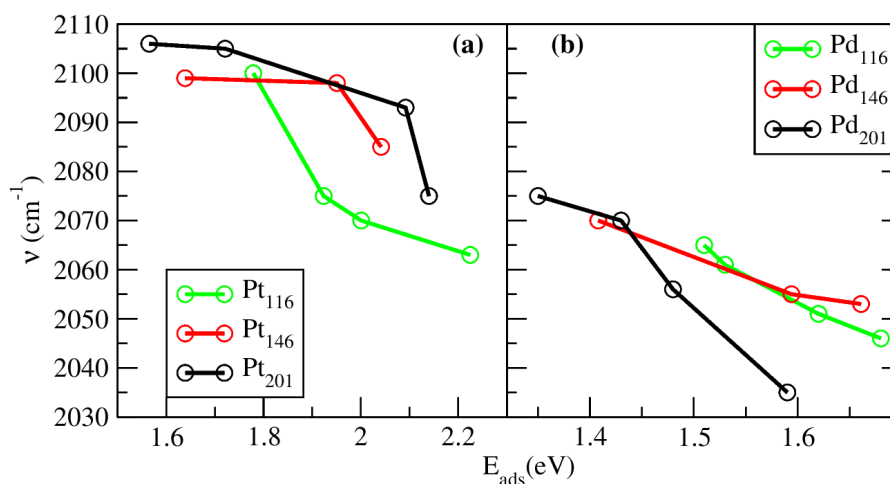
Figure 8.14: The variation of on-top sites vibrational frequency as a function of E_{ads} (a) on Pt nanoparticles and (b) on Pd nanoparticles.

the table that there is increase in ν as the $\overline{CN}$ increases if fcc and hcp sites are considered separately. Furthermore, the CO vibrational frequency value at the nanoparticles surface is higher than the slab model by about $20\,\mathrm{cm}^{-1}$. Regarding size effect on CO stretching vibration, no clear effect is observed to draw a conclusion for the systems investigated in the current work. In general, from the calculated vibrational frequencies it is straightforward to identify the on-top, bridge and 3-fold hollow site adsorption. However, differentiating between the different site coordination numbers for the same adsorption site type, in particular 3-fold hollow sites is not straightforward. But the on-top sites show some correlation with $\overline{CN}$, which can tell whether CO adsorbed at the terrace or other defect sites.

8.3   O chemisorption on Pt and Pd model catalyst

In this section, the adsorption energy changes of atomic oxygen on Pd and Pt metals of different model systems that is nanoparticle and extended surface is presented. To investigate the chemical adsorption of O in detail, various nanoparticle sizes and extended surfaces with different surface structure (coordination site) have been considered. All possible unique adsorption sites, i.e. on-top, bridge, 3-fold hollow (fcc, hcp) and 4-fold hollow at (111) and (100) facets has been considered. Experimental studies have shown that the most prefered atomic oxygen adsorption site on Pt(111) and Pd(111) surface is 3-fold site [163, 164]. Figure 8.15 shows various on-top and three-fold site adsorption energies on M_{201}. In this study, it was found that O prefers the 3-fold hollow sites for both Pt and Pd metals which is in line with other theoretical [129] and experimental [165, 166] studies. The on-top site adsorption energy is the lowest compared to other sites. Oxygen is not stable at bridge site and slide to the nearby three-fold sites except edge bridge sites of nanoparticles which agree well with other reported works [137, 167]. As can be seen in Figure 8.15 (a), the on-top site E_{ads} of Pt is always greater than that of the Pd and it decreases monotonically with increase in coordination number ($\overline{CN}$). It is observed that
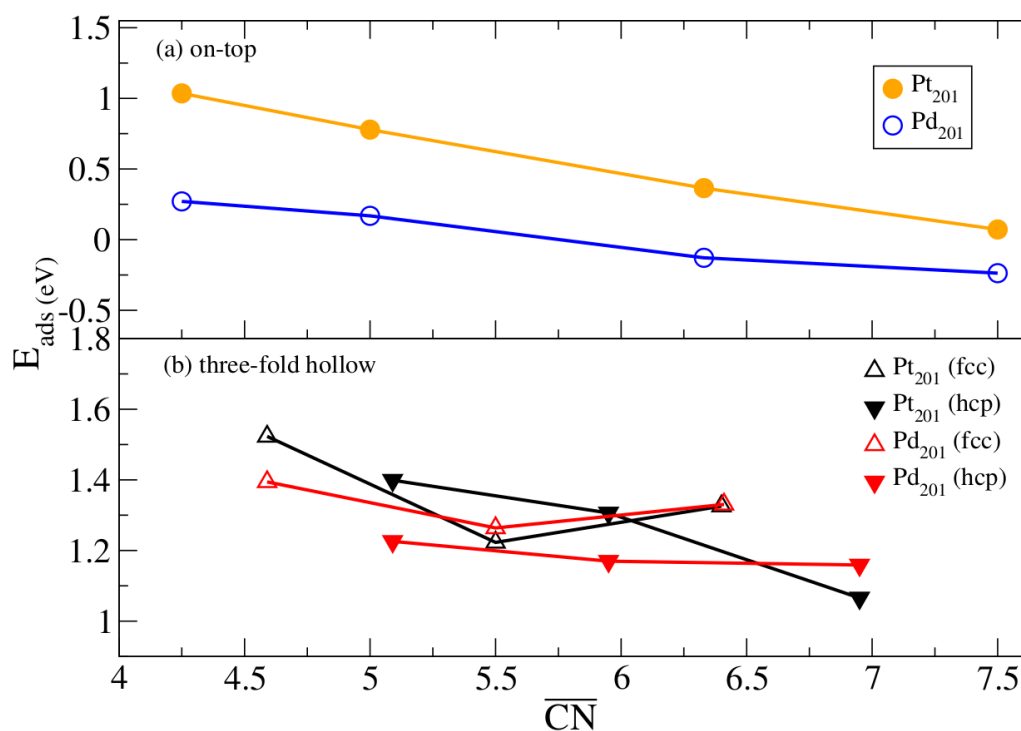
Figure 8.15: O adsorption on Pt_{201} and Pd_{201} nanoparticle at three-fold hollow and on-top sites. (a) the upper panel shows the on-top site E_{ads} with blue line (open circle) for Pd and orange line (filled circle) for Pt. (b) the lower panel shows the three-fold hollow sites E_{ads} with black lines for Pt and red lines for Pd.

for Pd at higher $\overline{CN}$ (7.5) the adsorption is endothermic (i.e. $E_{ads} < 0$). In general, for Pt (Pd) on-top site E_{ads} are in the range 1.03 to 0.07 (0.27 to -0.23) eV and three-fold sites are in the range 1.52 to 1.06 (1.39 to 1.15) eV. The average E_{ads} difference of all the on-top and 3-fold sites are 0.7 (1.2) eV for Pt (Pd). In the case of three-fold sites, as can be expected the hcp sites decrease with increase in $\overline{CN}$, however, the fcc site has not shown regular decrease of E_{ads} with $\overline{CN}$. Further detailed analysis of E_{ads} with various sites, sizes and shapes will be given the following sections. To see the effect of shape, various shapes of model nanoparticles have been selected which can be grouped into truncated octahedron, cuboctahedron and regular octahedron types. Because the three-fold sites E_{ads} is much higher than the on-top site and bridge sites are sliding off to 3-fold sites, mainly 3-fold sites will be considered in detail.

8.3.1   Effect of adsorption site and particle shape

Truncated Octahedron nanoparticles

The adsorption energies of atomic oxygen on three truncated octahedron model nanoparticles of different size that is M_{38}, M_{79} and M_{201} are investigated. Here M represents Pt and Pd metals. The adsorption energies of atomic oxygen on truncated octahedron model nanoparticles of Pt and Pd are plotted in Figure 8.16 and Table 8.4. The nanoparticles M_{38}, M_{79} and M_{201} have one, two and three unique fcc sites, respectively and the same is true for hcp sites. As illustrated in Figure 8.16, with the exception of M_{201} fcc site at $\overline{CN}$ 5.5, the value of E_{ads} decreases as $\overline{CN}$
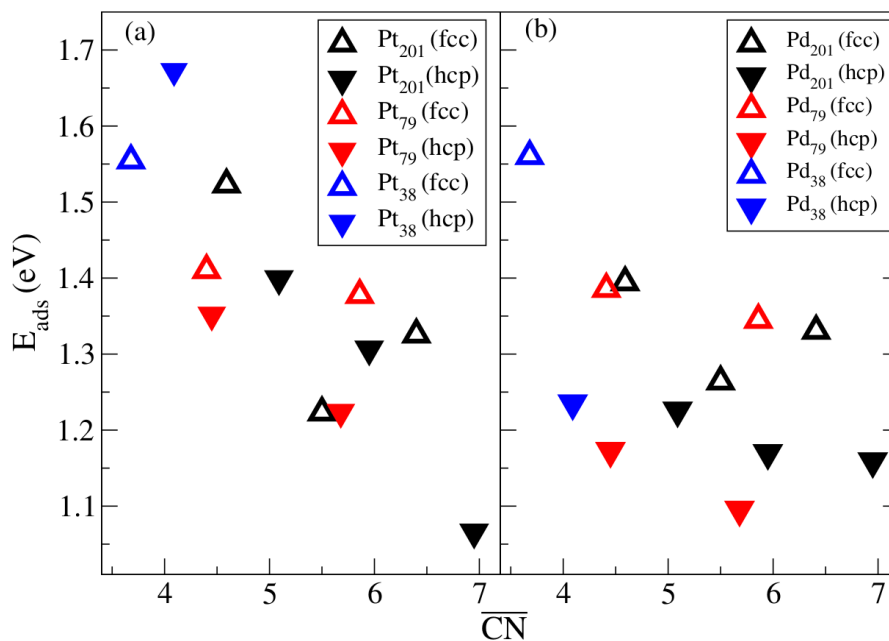
Figure 8.16: O adsorption energies of truncated ocatahedron nanoparticles of (a) Pt and (b) Pd at different three-fold hollow sites. The filled triangle down and open triangle up represent hcp and fcc sites. The black, red and blue colors correspond to M_{201}, M_{79} and M_{38}, respectively.

increases. If we see the local bonding at the site $\overline{CN}$ 5.5, two of the bonding metal atoms are from (111) facet and one metal atom is from (100) facet, which is weakly bonded to oxygen. It might be important to see the fcc and hcp sites separately. For Pd all fcc site E_{ads} lie above the hcp site meaning that hcp site adsorption is weaker than fcc site. On the other hand, in the case of Pt there is no such clear difference between hcp and fcc sites. Indeed, fcc sites oxygen E_{ads} of Pt_{79} are stronger than the hcp sites but the opposite is found for Pt_{38}. Thus, it is apparent from Figure 8.16 and Table 8.4 that the effect of metal coordination number on adsorption energy of different sites at a given fixed size is significant.

As illustrated in Table 8.4, the bond length r_{M-O} variation with various adsorption site for both Pd and Pt nanoparticles is not significant. For Pt-O, the bond length is found between 200 - 206 pm and Pd-O is between 198 - 200 pm. Following this almost similar bond length, very slight change in stretching frequency of Pt-O and Pd-O is calculated. The Pt-O and Pd-O stretching frequencies for nanoparticles are found in the range 500-524 cm^{-1} and 437-459 cm^{-1}, respectively. In the case of extended surfaces, compared to nanoparticles a slightly lower stretching frequencies are obtained, i.e. 439-459 cm^{-1} for Pt and 423-433 cm^{-1} for Pd with the fcc site is greater than hcp site. The experimental value on the Pt(111) surface fcc site is 480 cm^{-1} [132].

At the extended Pt(111) surface the favorable O adsorption site is fcc with 0.41 eV E_{ads} larger than hcp site, which is consistent with the scanning tunneling microscopy (STM) measurement [168] and the reported theoretical study [169]. Similarly, fcc sites are the most favored sites over hcp sites at Pt_{79}, whereas for Pt_{38} the opposite is obtained, i.e. hcp is preferred over fcc site with 0.11 eV E_{ads}. However, for Pt_{201} no clear preference was detected. For the extended Pt(111) surface the calculated Pt-O bond lengths at fcc and hcp sites are 205.2 and 205.3 pm,

Table 8.4: Three-fold site atomic oxygen adsorption energies (E$_{ads}$), vibrational frequencies (ν) and bond length (r$_{M-O}$) on Pt and Pd trunctated octahedron nanoparticles. The outer(inner) values of E$_{ads}$, ν and r$_{M-O}$ correspond to Pt(Pd) metals.

	M$_{201}$		
$\overline{CN}$	E$_{ads}$ (eV)	ν (cm^{-1})	r$_{M-O}$ (pm)
4.59 (fcc)	1.52 (1.39)	519 (454)	205.1 (200.1)
5.50 (fcc)	1.22 (1.26)	503 (453)	206.0 (199.5)
6.41 (fcc)	1.32 (1.33)	524 (452)	202.2 (198.4)
5.09 (hcp)	1.40 (1.22)	522 (456)	204.0 (200.0)
5.95 (hcp)	1.30 (1.17)	514 (440)	203.0 (198.7)
6.95 (hcp)	1.06 (1.16)	513 (436)	202.3 (198.5)

	M$_{79}$		
$\overline{CN}$	E$_{ads}$ (eV)	ν (cm^{-1})	r$_{M-O}$ (pm)
4.41 (fcc)	1.41 (1.38)	514 (457)	205.2 (199.6)
5.86 (fcc)	1.38 (1.34)	514 (455)	200.1 (199.8)
4.45 (hcp)	1.35 (1.17)	510 (448)	205.1 (199.6)
5.68 (hcp)	1.22 (1.09)	500 (437)	203.0 (198.0)

	M$_{38}$		
$\overline{CN}$	E$_{ads}$ (eV)	ν (cm^{-1})	r$_{M-O}$ (pm)
3.68 (fcc)	1.55 (1.56)	509 (459)	202.0 (199.6)
4.09 (hcp)	1.67 (1.23)	512 (449)	205.0 (199.7)

	M(111) slab		
$\overline{CN}$	E$_{ads}$ (eV)	ν (cm^{-1})	r$_{M-O}$ (pm)
6.95 (fcc)	1.25 (1.32)	459 (433)	205.2 (199.2)
7.50 (hcp)	0.84 (1.14)	439 (423)	205.3 (198.7)

respectively, which is in a complete agreement with the experimental data of 201 ± 5 pm [169]. Essentially, all Pt-O bond lengths of the nanoparticles are also in line with the the extended surface experimental values.

For the extended Pd surface, the fcc preference over hcp with E$_{ads}$ difference of 0.2 eV is in good agreement to the reported 0.2 eV by Todorova et al. [170]. Strikingly, regardless of site and size difference, for Pd the E$_{ads}$ at fcc sites is always larger than at hcp sites. This regularity is not present at Pt surface. The high resolution energy electron loss spectroscopy (HREELS) measured Pd-O stretching frequency 485 cm^{-1} is comparable to the calculated values in this work [164].

The other important question is how particle size can affect E$_{ads}$ of oxygen. For smaller size nanoparticles the fraction of corners and edges is large which would result to high fraction of under-coordinated sites at the surface. Below a certain size, the adsorbate at the (111) facet
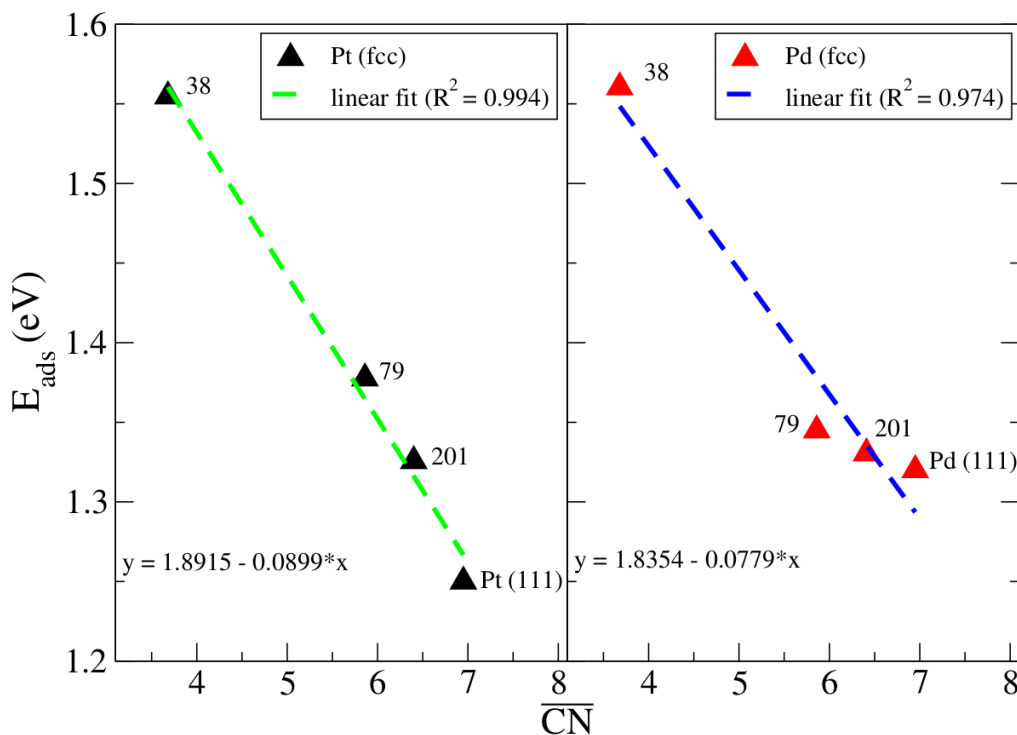
Figure 8.17: O adsorption energies of truncated ocatahedron nanoparticles and M(111) extended surface of Pt (left panel) and Pd (right panel) at fcc sites. The dashed lines are linear fit of the points, the equation and correlation coefficients are also given.

is influenced by the nearest-neighbor corner and edge atoms. The critical size at which this local effect becomes negligible depends on the metal type. For example, it was reported in the earlier works that in case of Au clusters this geometric effect disappears at distances beyond 2.7 nm, while in case of Pt this effect vanishes at 1.6 nm [171, 172]. In order to find a possibly simple relation between adsorption energy and cluster size, it is necessary to consider similar adsorption sites as much as possible for each size. Here, to investigate whether there is size effect or not on E_{ads} of O, the largest coordination site on the (111) facet of each size is picked and compared with the extended surface, which is shown in Figure 8.17. Up on change in size from M_{38} to M_{201} and then to extended surface, a very good linear correlation of E_{ads} with size is obtained for the high coordinated fcc site (Figure 8.17). In the case Pt the correlation coefficient found to be 0.99 and for that of Pd is 0.97. For size Pt_{38}, E_{ads} of O is 0.17 and 0.22 eV higher than Pt_{79} and Pt_{201}, respectively. These large differences in E_{ads} is mainly due to large fractional under-coordinated sites and increase in exposed surface atom. In case of Pt_{38}, 84 % of the atoms are exposed to the surface and the fcc sites are surrounded by lower coordinated edges and corners, this lead to increase in E_{ads}. As size increases going towards Pt_{201}, the surface area of (111) facet gets increase thereby the fraction of lower coordinated sites to the total sites becomes lowered. Thus, the fcc site at center of (111) facet of Pt_{201} is relatively far way from edges and corners and result to lower E_{ads}. On further increase in size, at certain point the finite-size effect can be reached that will provide the same value of E_{ads} to that of the bulk crystal. Based on the data in Figure 8.17, Pt_{201} is approaching to the corresponding extended surface Pt(111) with E_{ads} difference of 0.07 eV, but Pd_{201} shows much

closer E_{ads} to the Pd(111) single-crystal surface with only 0.003 eV deviation.

Regular octahedron particles

The regular octahedron particles are entirely made from (111) facets. Previous studies have been shown that on variation of shape (and hence facets) of nanoparticles can have different catalytic properties [173]. Here, to assess E_{ads} of atomic oxygen on regular octahedron particles, three sizes have been selected, i.e. 44, 85, 146 atoms. Table 8.5 summarizes E_{ads} of O on regular octahedron of various size. First of all, aforementioned weak E_{ads} on-top sites and instability at bridge site are also occurred in these category of nanoparticles. Thus, besides the 3-fold sites, only stable bridge and on-top sites E_{ads} are presented in Table 8.5. The stretching frequency and M-O bond lengths found to lie in similar range as presented above (Table 8.4) for truncated octahedron. For that reason only the value of E_{ads} is presented for this class of nanoparticles. Generally, for 3-fold sites the stretching frequency for Pt-O is in the range 500-516 cm^{-1} and for Pd-O in the range 437-452 cm^{-1}. The on-top sites exhibit larger frequency compare to 3-fold sites, 760-790 and 665-695 cm^{-1} for Pt-O and Pd-O, respectively. The bridge site lie somewhere in between on-top and 3-fold sites that is in the range 610-620 and 525-540 cm^{-1} for Pt-O and Pd-O, respectively.

Interestingly, for Pt at 3-fold sites significant decrease in E_{ads} was found in comparison to the truncated octahedron nanoparticles and this behavior is not shown clearly for Pd. This can be in part due to the fact that regular octahedron possess low proportion of under-coordinted sites (less number of edges and corners) compared to truncated octahedron that has (100) and (111) crystallographic facets. It has been long recognized that usually surface energies of Pt(111) facet is less than the Pt(100) facet [174]. This implies that the (111) surface is more stable and hence, it should result in weak adsorption. In line with this, it has been reported that the low index (111) facet has shown lower activity compared to other high index facets [175]. Therefore, for this class of nanoparticles Pd would seem exhibit rather strong binding towards oxygen compared to Pt. Regarding on-top and bridge sites, it has been found that O at highly coordinated sites moved to the 3-fold site on course of relaxation. Among bridge sites only edge sites are favorable for O adsorption. For the on-top site, unlike to truncated octahedron case, highly coordinated sites at center of (111) facet, that is $\overline{CN} > 5.16$ found to be unfavorable sites for both Pd and Pt. The stable on-top and bridge sites E_{ads} of O are given in Table 8.5. The bond lengths are found in the range 177-179 pm for Pt-O and 178-180 pm for Pd-O, which is basically in similar range of the truncated clusters. Generally, comparing to truncated octahedron nanoparticles, much smaller adsorption energies are obtained for this class of nanoparticles. This is clearly seen especially on Pt.

Cuboctahedron nanoparticles

This class of particles have eight triangular faces of (111) facet and six square faces of (100) facet. Table 8.6, list atomic oxygen E_{ads} at Pt_{55} and Pt_{147} cuboctahedron nanoparticle surfaces. The results reveals that in this class of particles, E_{ads} of O at hcp sites are higher than fcc sites, which

Table 8.5: Three-fold, on-top and bridge sites atomic oxygen adsorption energies (E_{ads}), vibrational frequencies (ν) and bond length (r_{M-O}) on Pt and Pd regular octahedron nanoparticles. The outer(inner) values of E_{ads} correspond to Pt(Pd) metals.

M146					
3-fold hollow		on-top		bridge	
$\overline{CN}$	E_{ads} (eV)	$\overline{CN}$	E_{ads} (eV)	$\overline{CN}$	E_{ads} (eV)
3.04 (fcc)	0.80 (1.19)	2.33	1.33 (0.41)	3.22	1.12 (0.97)
4.72 (fcc)	0.79 (1.41)	4.58	0.46 (0.12)	4.72	1.26 (1.12)
5.13 (fcc)	1.35 (1.42)	5.16	—— (0.18)	5.11	1.34 (1.17)
6.41 (fcc)	0.99 (1.34)				
6.04 (hcp)	0.92 (1.14)				
6.95 (hcp)	0.81 (1.06)				

M85					
3-fold hollow		on-top		bridge	
$\overline{CN}$	E_{ads} (eV)	$\overline{CN}$	E_{ads} (eV)	$\overline{CN}$	E_{ads} (eV)
3.04 (fcc)	0.91 (1.18)	2.33	1.32 (0.48)	3.22	1.10 (1.03)
4.72 (fcc)	1.38 (1.19)	4.58	0.46 (0.18)	4.72	1.34 (1.18)
6.13 (fcc)	1.09 (1.35)	5.16	0.32 (0.23)		
5.86 (hcp)	0.96 (1.09)				

M44					
3-fold hollow		on-top		bridge	
$\overline{CN}$	E_{ads} (eV)	$\overline{CN}$	E_{ads} (eV)	$\overline{CN}$	E_{ads} (eV)
3.04 (fcc)	0.98 (1.05)	2.33	1.00 (0.37)	3.22	0.91 (0.89)
4.31 (fcc)	1.44 (1.41)	6.50	0.21 (0.41)	4.33	1.10 (1.05)
4.54 (hcp)	1.06 (1.14)				

is different from what is found for regular and truncated octahedron particles. However, this result is in complete agreement with the previous reported results obtained for Pt nanoparticles [137, 176]. This is because of hcp sites are located at near to corner bonding directly to the corner and edge atoms, where as fcc site is center of the (111) facet, even though the latter is also surrounded by the (111) × (100) edges. The other characteristic behavior observed for these particles is that O binds strongly on bridge sites and have not moved from the place it has initially bind except bridge sites at center of (111) facet. As can be seen from Table 8.6, on average rather large E_{ads} is calculated for cuboctahedron particles at bridge sites. These bridge sites are mainly from the (100) facets and edge of (111) × (100). Regarding on-top sites, O binds weakly similar to the previous results shown for regular and truncated octahedron but corner sites exceptionally shown higher E_{ads}.

Table 8.6: Three-fold, on-top and bridge sites atomic oxygen adsorption energies (E_{ads}) on Pt cuboctahedron nanoparticles. The outer(inner) values of E_{ads} correspond to Pt(Pd) metals.

3-fold hollow		Pt$_{147}$ on-top		bridge	
$\overline{CN}$	E_{ads} (eV)	$\overline{CN}$	E_{ads} (eV)	$\overline{CN}$	E_{ads} (eV)
4.40 (fcc)	0.99	3.33	1.21	3.83	1.68
4.04 (hcp)	1.28	6.50	0.11	4.72	1.58
5.18 (hcp)	1.14			5.5	1.35
				6.44	1.36

3-fold hollow		Pt$_{55}$ on-top		bridge	
$\overline{CN}$	E_{ads} (eV)	$\overline{CN}$	E_{ads} (eV)	$\overline{CN}$	E_{ads} (eV)
3.40 (fcc)	0.94	3.33	1.31	3.61	1.56
3.77 (hcp)	1.35	4.66	0.66	5.16	1.40
		6.33	0.48		

8.4 Oxygen Coverage

The activity of CO oxidation on the surface of small Pt nanoparticles known to accompany oscillatory behavior under realistic conditions and results different activity. The reason for this oscillatory behavior is correlated to cyclic oxidation reduction of Pt surface. Oscillations are known to occur on single crystal catalyst and nanoparticle under both vacuum conditions and actual catalytic conditions [177]. There is consensus that under reduced condition CO covered metallic surface shows low activity because of poisoning by the CO. The higher activities are observed for oxidized surface structure which can be either a surface oxide or an oxygen covered surface [178]. Recently Boubnov et al. [177] have studied CO oxidation on Pt nanoprticles and found that the smaller nanoparticles (< 2 nm) are prone to oxidation at higher temperature. Atomic level understanding of oxygen coverage effect on the Pt surface is important as the reactivity of Pt catalyst at real operation condition depends strongly on the type of oxide surface structure formed. In this context here oxygen coverage at different Pt nanoparticles size is examined in order to understand the surface structure under various coverage.

8.4.1 Assessment of stable adsorbate arrangement

So far we have seen adsorption energy of single adsorbate on the surface of the metal. But it is also important to see the influence of coverage on adsorption energy. The presence of more than one adsorbates has an effect on adsorption energy because of adsorbate-adsorbate interaction. In this section the influence of oxygen coverage to the adsorption energy on the surface of platinum nanoparticles is presented. As coverage of oxygen increase, the average separation between oxygen adsorbates becomes short which results to weak adsorption energy. This implies

Table 8.7: Configurations of two adsorbed oxygen atoms on Pt$_{79}$ at various O-O distance with their relative energy (E$_{rel}$) with respect to the lowest energy configuration (J) and adsorption energy (E$_{ads}$). The average adsorption energy (Average E$_{ads}$) of the singly adsorbed oxygen at same site where the two adsorbates placed are also presented. The relative energy (E$_{rel}$) is calculated with respect to the lowest energy structure (J).

distance	configuration	$\overline{CN}$ (site)	E$_{rel}$ (eV)	E$_{ads}$ (eV)	Average E$_{ads}$ (eV)
1.60 Å					
	A	5.86(fcc)+5.68(hcp)	0.824	1.06	1.30
	B	4.40(fcc)+4.45(hcp)	0.657	1.14	1.38
	C	5.68(hcp)+4.40(fcc)	0.625	1.16	1.32
2.77 Å					
	D	5.68(hcp)+5.68(hcp)	0.651	1.15	1.22
	E	4.40(fcc)+5.86(fcc)	0.220	1.36	1.39
	F	4.45(hcp)+5.68(hcp)	0.442	1.25	1.29
3.20 Å					
	G	5.86(fcc)+4.45(hcp)	0.306	1.32	1.36
4.80 Å					
	H	4.45(hcp)+5.68(hcp)	0.484	1.23	1.29
5.54Å					
	I	4.45(hcp)+4.45(hcp)	0.212	1.35	1.35
	J	4.40(fcc)+4.40(fcc)	0.000	1.42	1.41

that the interaction is repulsion at short distance. The repulsion interaction at higher coverage might be important to keep the coverage of the adsorbates less than a monolayer. Even at low coverage the interaction can be repulsive if oxygen adsorbates are close to each other at the surface. Thus, at given coverage depending on the configuration of oxygen on the surface of nanoparticles, the adsorption energy per atom can be different. That means isomers of the same number of oxygen will have different relative stability and adsorption energy per atom at the surface of the nanoparticle. In this work, to study increasing of oxygen coverage at Pt nanoparticle surface, two and three pairs of oxygen atoms are arranged systematically on Pt$_{79}$ nanoparticle at different distances and their energies are computed (Table 8.7 and Table 8.8). In this way, the most stable possible arrangements are selected and applied for oxygen coverage study at Pt nanoparticle surface.

As can be seen in Table 8.7 and Table 8.8, for the systematic arrangement of oxygen atoms several possible adsorbate-adsorbate distances are considered. In the case of two adsorbates, five O-O distances, i.e. 1.60, 2.77, 3.20, 4.80 and 5.54 Å has been investigated. The shortest possible distance between oxygen adsorbates is 1.60 Å and the most stable configuration (C) has adsorption energy per atom of 1.16 eV, which is considerably weaker compared to the average adsorption energy of two singly adsorbed oxygen at the same sites (1.32 eV). At this distance, two other isomers (A and B) are calculated and their adsorption energy is less than 1.16 eV. It was observed that the two oxygen atoms repel each other and diffuse away from
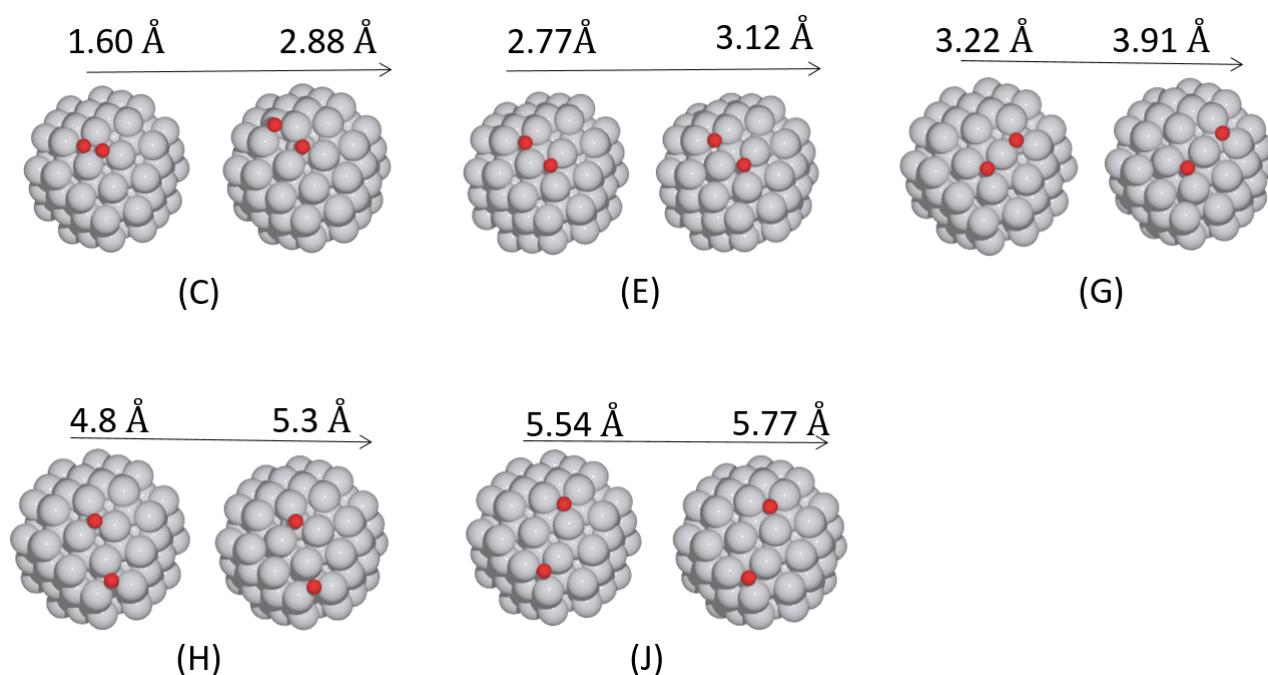
Figure 8.18: The O-O distance for stable configurations of two oxygen adsorbates before and after geometrical relaxation on Pt_{79}. These structures correspond to the stable isomers (C, E, G, H and J) that are given in Table 8.7.

their initial position to create enough space so that to minimize the repulsion interaction. Figure 8.18 illustrates the oxygen adsorbates position before and after local relaxation for the stable isomers of various distance and shows the extent of repulsion. The next O-O distance is 2.77 Å, in which three isomers are studied. The most stable isomer (E) among them has adsorption energy of 1.36 eV. The other configurations at O-O distance of 3.20 Å and 4.80 Å have adsorption energy per atom of 1.32 eV and 1.23 eV, respectively. The longest possible O-O distance considered for Pt_{79} size is 5.54 Å, in which the most stable isomer found to have adsorption energy of 1.47 eV. In general, as evidenced from the results when the adsorbates become close each other (shorter distance) the adsorption energy becomes low, indicates weak metal-oxygen bond. The lowest relative energies of all the configurations are found at longest distance implies that the repulsion interaction is minimized. The adsorption energies at this distance is not reduced compared to the average adsorption energy of singly adsorbed oxygen at the same sites or even somewhat increased, this might be because of strain effect as they are adsorbed close to the edges.

Table 8.8 shows different arrangement of three oxygen adsorbates sitting symmetrically at various distances. Four O-O distances are inspected, i.e. at 1.60, 2.77, 4.81 and 6.01 Å. The general tendency of decreasing adsorption energy with shortening in O-O distance is the same as in the case of two oxygen adsorbates discussed already above. As expected the lowest adsorption energies are obtained at the shortest distance 1.60 Å. and gradually increase with distance. At the longest distance (5.54 Å) the adsorption energy remains the same as the average adsorption of singly adsorbed oxygen atom. Figure 8.19 shows some of the stable configurations at different O-O distance that corresponds to Table 8.8 results. Overall, O-O adsorption at 1.60 Å i.e. next neighbor adsorption that leads to complete mono-layer coverage seems not

Table 8.8: Configurations with three adsorbed oxygen atoms on Pt_{79} at various O-O distance with their relative energy (E_{rel}) with respect to the lowest energy configuration (G) and adsorption energy (E_{ads}). The average adsorption energy (Average E_{ads}) of the singly adsorbed oxygen at same site where the three adsorbates placed are also presented. The relative energy (E_{rel}) is calculated with respect to the lowest energy structure (G).

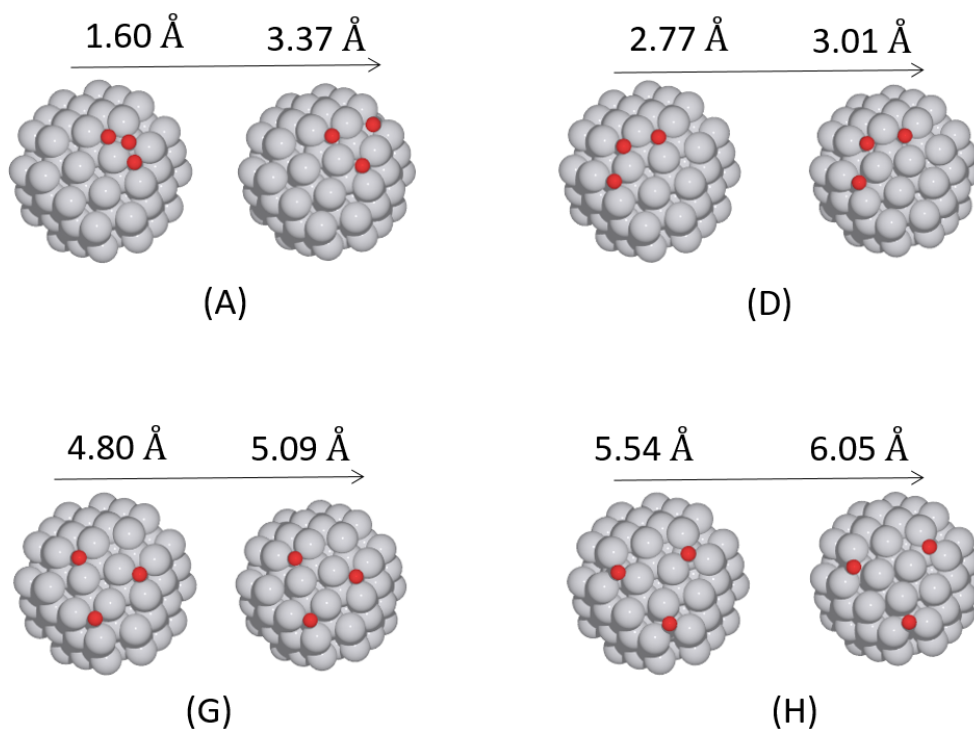| distance	configuration	$\overline{CN}$	E_{rel} (eV)	E_{ads} (eV)	Average E_{ads} (eV)
1.60 Å					
	A	2(4.40)+4.45	0.562	1.20	1.39
	B	2(4.40)+5.68	0.695	1.15	1.35
	C	2(5.68)+5.86	1.017	1.05	1.27
2.77Å					
	D	3(4.40)	0.054	1.37	1.41
	E	2(4.45)+5.68	0.269	1.29	1.31
	F	2(4.40)+5.86	0.268	1.29	1.39
4.81Å					
	G	3(4.40)	0.000	1.39	1.41
5.54Å					
	H	3(4.45)	0.088	1.36	1.35

Figure 8.19: The O-O distance for stable configurations of three oxygen adsorbates before and after geometrical relaxation on Pt_{79}. These structures correspond to the stable isomers (A, D, G and H) that are given in Table 8.8.

favored, while the other distances adsorption energy is still relatively strong. Thus, based on the result we can infer that adsorbing oxygen next to each other within 1.60 Å will not be stable arrangement. The relative stability of the configurations are also in line with this conclusion that long distance has better stability. To conclude, the systematic study reveals that the most stable adsorption configurations for both two and three oxygen adsorbates are obtained when oxygen adsorbs at 3-fold hollow site close to edges and corners (lower coordination sites). When oxygen adsorbates are placed close to each other within 1.60 Å the repulsion is strong leads to diffusion. The results suggested that at least there should be 2.77 Å O-O distance to avoid diffusion.

8.4.2   Coverage effect on adsorption energy

Here, the effect of oxygen coverage on adsorption energy for size Pt_{79}, Pt_{116} and Pt_{201} are presented in detail at various coverage. A particular coverage can have so many possible arrangements and it will be computationally expensive to address all configurations. To this end, initial oxygen distribution was made based on the knowledge gained on two and three O configuration calibration that has been assessed above. Thus, oxygen was adsorbed on 3-fold hollow sites at (111) facet with a minimum distance of 2.77 Å between each proximate O adsorbate. In the case of Pt_{116} and Pt_{201}, the (100) facet is extended in which about half portion of the surface is from this facet. For that reason, in addition to the 3-fold sites, O was adsorbed on 4-fold sites at (100) facet with 2.85 Å between each proximate O adsorbate. As much as possible low coordinated sites close to edges and corners have been given priority as these sites have relatively higher adsorption energy. The coverage (Θ) was defined as monolayer ($\Theta = 1$ ML) when all 3-fold and 4-fold sites are occupied by O. In other words, a given fractional coverage obtained by dividing the number of occupied sites by the total number of 3-fold and 4-fold sites. In all sizes, the maximum possible coverage for which the oxygen atoms remain at their initial adsorption sites is about 0.5 ML and increasing coverage beyond 0.5 ML results in oxygen diffusion to other sites or desorption from the surface. For this reason, the maximum coverage presented in this work is 0.62 ML at Pt_{116}.

Pt_{79}

Figure 8.20 shows structural configuration of three different coverages for Pt_{79}, i.e. 0.22, 0.43 and 0.51 ML. In all cases, oxygen adsorbed on 3-fold sites of all (111) facets mostly close to edges and corners. The adsorption energy per oxygen atom (eV/O) is shown in Figure 8.22. The adsorption energy decreases with increase in O coverage. The value of E_{ads} per O atom calculated at coverage 0.22 ML is 1.12 eV and at 0.51 ML is 0.93 eV. The difference in E_{ads} per O atom between the two coverages is ≈ 0.2 eV. If we compare those adsorption energies at coverage 0.22, 0.43 and 0.51 ML with the average adsorption energy of singly adsorbed oxygen on the corresponding sites, we get a difference of 0.25, 0.33 and 0.44 eV, respectively.
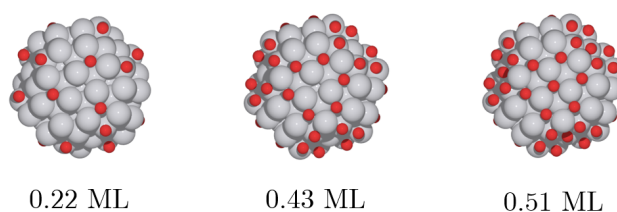
0.22 ML   0.43 ML   0.51 ML

Figure 8.20: Optimized Pt_{79} nanoparticle covered with atomic oxygen at different coverage (Θ). The white(red) balls represent Pt(O).

Pt_{116}

For Pt_{116} again three different coverages, 0.37, 0.44, 0.62 ML are evaluated. Figure 8.21 shows the structural configuration for three coverages. Since Pt_{116} comprises of both (100) and (111) extended facets, oxygen atom adsorbed on 3-fold site at (111) facets and on 4-fold site at (100) facets. The sites close to edges and corners have been given priority to adsorb oxygen because of reason that these sites are energetically favored. During geometrical optimization significant surface structure change is observed in particular at (100) facet. What is observed is that Pt

0.37 ML   0.44 ML   0.62 ML

Figure 8.21: Optimized Pt_{116} nanoparticle covered with atomic oxygen at different coverage (Θ). The white(red) balls represent Pt(O).

atoms at the center of (100) sink down towards the interior and Pt atoms at the edges somehow expanded outward (see Figure 8.21). Moreover, after the Pt atom at the center of (100) facet sink, the oxygen atom on 4-fold sites move towards the edge and corner and rearrange to 3-fold adsorption. This effect is more pronounced at 0.37 and 0.44 ML whereas it attenuates at 0.62 ML. This can be due to the fact that at $\Theta = 0.62$ ML most sites at every side of facet is occupied by O, which result equally balanced strain in all sides that helps to avoid the dislocation of surface Pt atoms. As shown on Figure 8.22 (middle panel), the adsorption energy gets decrease with increase in Θ. Generally, the relative adsorption energy difference between these coverages is not substantial. However, comparing with average adsorption energy of the singly adsorbed O on the same sites, the difference is large, i.e. 0.28, 0.40 and 0.41 eV for the 0.37, 0.44 and 0.62 ML coverage, respectively.

Pt_{201}

Figure 8.23 illustrates the four different oxygen coverages at Pt_{201}. Pt_{201} has the same (100) facet area as that of the Pt_{116} but has larger (111) facet area than the Pt_{116}. Analogues to what has happened at Pt_{116} (100) facet, the surface Pt atom dislocation were observed on course of
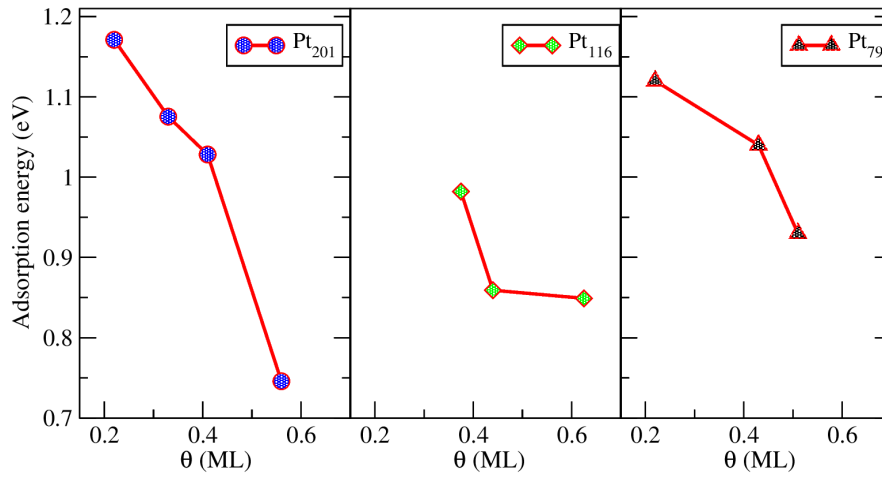
Figure 8.22: Variation of adsorption energy per O atom (E_{ads}/O) as a function of atomic oxygen coverage(Θ) on Pt_{201} (most-left panel), Pt_{116} (middle panel) and Pt_{79} (most-right panel).

geometry optimization. Nevertheless, the overall surface structure change up on adsorption is less severe compared to the Pt_{116} because of the large surface area of (111) facet. Figure 8.22 (most-left panel), presents the adsorption energies for the different coverages considered on Pt_{201}. As anticipated, the adsorption energy decreases monotonically with increase in oxygen coverage (Θ). Going from lower coverage (0.22 ML) to higher coverage (0.56 ML), 0.42 eV relative adsorption energy difference is calculated. At Θ = 0.22 ML the adsorption energy lessen slightly (0.13 eV) from the average adsorption energy of the singly adsorbed oxygen at the same sites. On the other hand, a considerable difference (0.56 eV) is calculated for Θ = 0.56 ML.
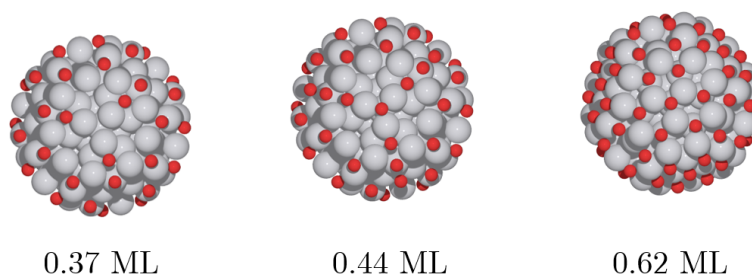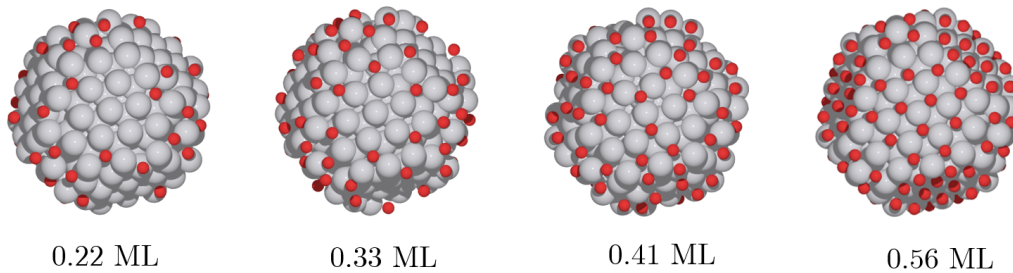

Figure 8.23: Optimized Pt_{201} nanoparticle covered with atomic oxygen at different coverage (Θ). The white(red) balls represent Pt(O).

Taken as a whole, the adsorption energy decreases with increase in coverage as shown in Figure 8.22. Up on adsorption oxygen atoms always keep away from each other. Oxygen adsorption coverage on (100) surface leads to a significant surface structure deformation and this was large in particular for the sub-truncated Pt_{116} nanoparticle. In the case of Pt_{79}, oxygen adsorbed only at (111) facet and no substantial surface structure change has been observed. The difference between the average adsorption energy of the singly adsorbed oxygen and adsorption energy of the highest oxygen coverage is 0.44 eV for Pt_{79}, 0.41 eV for Pt_{116} and 0.56 eV for Pt_{201} .

The d-band center descriptor is employed to check whether the electronic structure can
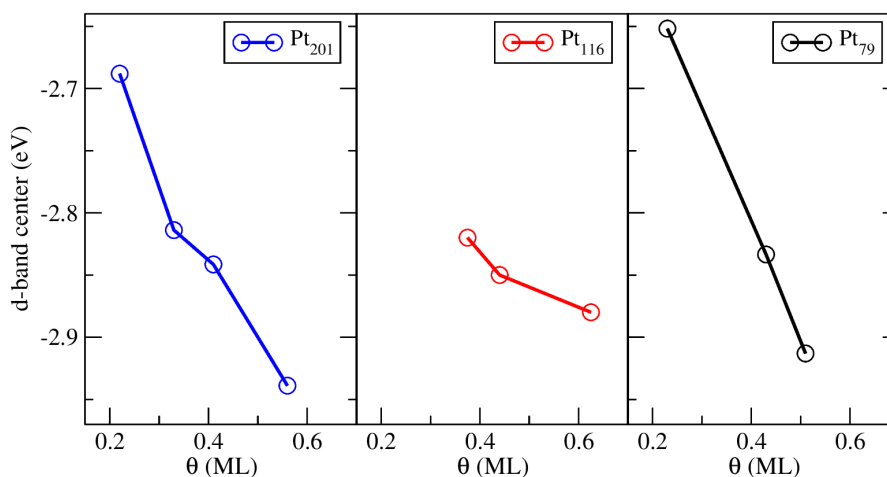
Figure 8.24: The calculated d-band ceneter for Pt_{201} (most-left panel), Pt_{116} (middle panel) and Pt_{79} (most-right panel) as a function of the O coverage. These coverages correspond to the configurations presented in Figures 8.20, 8.21 and 8.23.

correlate with oxygen coverage on nanoparticle surface. It should be pointed out that it is not possible to apply the geometry descriptor $(\overline{CN})$ for coverage study since oxygen is adsorbed at different sites. Figure 8.24 depicts d-band center variation as a function of O coverage for configurations presented in Figures 8.20, 8.21 and 8.23. For all nanoparticle sizes, almost a linear lowering of the d-band center with increase in O coverage is observed. If we compare the d-band center change with the change in adsorption energy per atom shown in Figure 8.22, a change closer to linear is observed. This down shift of d-band center with coverage indicates the weakening of oxygen bonding strength. A similar d-band center change with coverage has been reported previously on both slab model and nanoparticles [137, 179, 180].

8.4.3 CO vibrational frequency in the presence of oxygen coverage

To investigate the CO stretching vibrational modes changes in the presence of various oxygen coverage, single CO was adsorbed at oxygen covered Pt_{201} surface. Table 8.9 summarizes the adsorption energy and vibrational frequency of CO at different coverages. The CO adsorption energy decreases in the range from $\Theta = 0.00$ ML to $\Theta = 0.33$ ML. Going from $\Theta = 0.00$ ML to $\Theta = 0.22$ ML the CO adsorption energy is lowered by $\approx 0.5\pm0.3$ eV. In comparison with $\Theta = 0.00$ ML, at $\Theta = 0.33$ ML CO adsorption energies at lower $\overline{CN}$ drop by about 0.9 ± 0.1 eV, while very significant drop (1.56 eV) is observed at $\overline{CN} = 6.33$ which is at (100) facet. Further increase in coverage at $\Theta = 0.41$ ML, the same site ($\overline{CN} = 6.33$) E_{ads} of CO increases strongly to large value 2.87 eV. This would seem indication of the presence of substantial surface structure change due to oxygen load especially at (100) facet and this was also seen visually from the relaxed structure (see Figure 8.23). Similar over-binding of CO on oxidized Pt surface has been reported from experimental measurment by Boubnov et al. [177]. In that work the authors underline that at oxidized surface of about 2 nm nanoparticles the binding of CO is relatively strong and not easy to remove from the surface even after purging with He. They have measured also the CO vibration band of 2119–2123 cm^{-1} and 2085–2089 cm^{-1} at oxidized

and reduced surface, respectively, which is inline with the calculated result in this work. The result in Table 8.9 reveals that the CO vibrational frequencies increase in the presence of oxygen coverage.

Table 8.9: On-top sites CO adsorption energies ($\dagger E_{ads}$) in eV and vibrational frequencies (ν) in cm^{-1} on oxygen covered Pt$_{201}$ nanoparticles. Θ represents oxygen coverage.

$\overline{CN}$	$\Theta = 0.00$ ML		$\Theta = 0.22$ ML		$\Theta = 0.33$ ML		$\Theta = 0.41$ ML	
	$\dagger E_{ads}$	ν	$\dagger E_{ads}$	ν	$\dagger E_{ads}$	ν	$\dagger E_{ads}$	ν
4.25	2.14	2075	1.44	2105	1.35	2141	2.00	2130
5.00	2.09	2093	1.27	2118	1.09	2129	1.08	2170
6.33	1.84	2079	1.21	2139	0.28	2169	2.87	2127
7.50	1.56	2106	1.45	2117	1.40	2115	—	—

8.4.4   Gibbs free energy of adsorption for oxygen coverage

So far we have seen in detail how CO adsorption energy depends on adsorption site and oxygen coverage. It is also known that coverage depends on pressure and temperature. When metal surfaces exposed to oxygen, depending on the partial pressure and temperature various structures can be formed, such as surface adsorbed oxygen, surface oxide films or bulk metal oxides [181]. Atomistic thermodynamics approach, using density functional theory calculations can be applied to quantify the thermodynamics of various surface-adsorbate structure and to relate them to the composition of the gas phase under realistic experimental conditions [182, 183]. This approach has been widely applied to oxidation catalysis in which gaseous O$_2$ is the principal source of surface oxygen. The Gibbs free energy is the appropriate thermodynamic potential to be considered for fixed temperature and pressure (T, p). For an infinite and homogeneous system, if such a system is considered as a reservoir, the Gibbs free energy per formula unit or particle is equivalent to the chemical potential μ. In the present context, the O$_2$ gas acts as a reservoir, because it can give (or take) any amount of oxygen to (or from) the sample [182].

In order to investigate the effect of temperature and pressure on the stability of oxygen covered structures that have been presented above, the Gibbs free energy of adsorption is applied using the equation:

$$\Delta G^{ad}(T,p) = \frac{1}{A}(G(\Theta) - G(\text{bare}) - N_O \mu_O(T,p)) \tag{8.1}$$

where $\Delta G^{ad}(T,p)$ is the Gibbs free energy of adsorption, $G(\Theta)$ and $G(\text{bare})$ are Gibbs free energy of oxygen coverage complex and bare nanoparticle. A is the surface area. N_O is the number oxygen atoms on the surface and $\mu_O(T,p)$ is the chemical potential of oxygen at certain temperature and pressure condition.

In Eq. 8.1, the solid phase Gibbs free energy and gas phase oxygen chemical potential

comprises of entropy, enthalpy and total energy contributing terms. It might be reasonable to neglect the effect of temperature and pressure for coverage complex and bare nanoparticle. Neglecting pressure is meaningful as the solid phase are not that much compressible, so that it is expected that there will not be significant energy change. For neglecting the temperature, it is assumed that the oxygen over-layer and the bare nanoparticle are equally affected by the temperature and these temperature dependent terms will cancel each other in the calculation. Therefore, the dominant term in the Gibbs free energy of coverage complex and the bare nanoparticle will be the total energy, which can directly compute from DFT. However, the temperature and pressure effect for the gas phase is significant and need to be included to the gas phase oxygen chemical potential $\mu_O(T, p)$. This allows to rewrite eq. 8.1 as

$$\Delta G^{ad}(T, p) \approx \frac{N_O}{A}\left(\overline{E}_{ads} - \mu_O(T, p)\right) \tag{8.2}$$

the term $\overline{E}_{ads}$ is the average adsorption energy, which is given by

$$\overline{E}_{ads} = -\frac{1}{N_O}\left(E^{total}(\Theta) - E^{total}(bare) - N_O \times \frac{1}{2}E^{total}(O_2)\right) \tag{8.3}$$

where $E^{total}(\Theta)$, $E^{total}(\text{bare})$ and $E^{total}(O_2)$ are total energies of oxygen covered nanoparticle, bare nanoparticle and oxygen molecule.

In eq. 8.2, $\mu_O(T, p)$ consists of the temperature and pressure correction terms for the gas phase oxygen molecules, which is expressed mathematically as

$$\mu_O(T, p) = \frac{1}{2}\left[E_{O_2}^{ZPE} + \Delta\widetilde{\mu}_{O_2}(T, p^0) + k_B T \ln\left(\frac{p_{O_2}}{p^0}\right)\right] \tag{8.4}$$

where p^0 corresponds to standard state pressure (1 atm) and p_{O_2} is the partial pressure of oxygen molecule. $\Delta\widetilde{\mu}_{O_2}(T, p^0)$ includes the contributions from vibrations and rotations of the molecule, as well as the ideal gas entropy at 1 atmosphere. $E_{O_2}^{ZPE}$ is the zero point energy (ZPE) correction of oxygen molecule. For $\Delta\widetilde{\mu}_{O_2}(T, p^0)$ experimental values are taken from NIST webbook and calculated by using the Shomate equations [184].

At this point it might be insightful to see first the effect of temperature and pressure on free energy of O$_2$ gas at realistic experimental conditions. For temperature dependent change in Gibbs free energy we can use $\Delta\widetilde{\mu}_{O_2}(T, p^0) = \Delta H - T\Delta S$ and for pressure dependent change $k_B T \ln(\frac{p_{O_2}}{p^0})$. The pressure effect is also temperature dependent. Figure 8.25 shows the Gibbs free energy change of O$_2$ gas as a function of temperature (a) and pressure (b). As clearly seen, the change in pressure and temperature has significant effect on the Gibbs free energy of O_2 gas. As the temperature increases the Gibbs free energy lowers linearly. The experimental relevant temperature range change, i.e., from 300 K to 800 K result to energy drop of by about 1 eV. Similarly Gibbs free energy changes linearly with pressure and the slope is more steep at high temperature. From this we can understand that the effect of experimental temperature and pressure on gas phase O_2 molecule is substantial and including this effect to the Gibbs free energy of adsorption seems to be necessary.
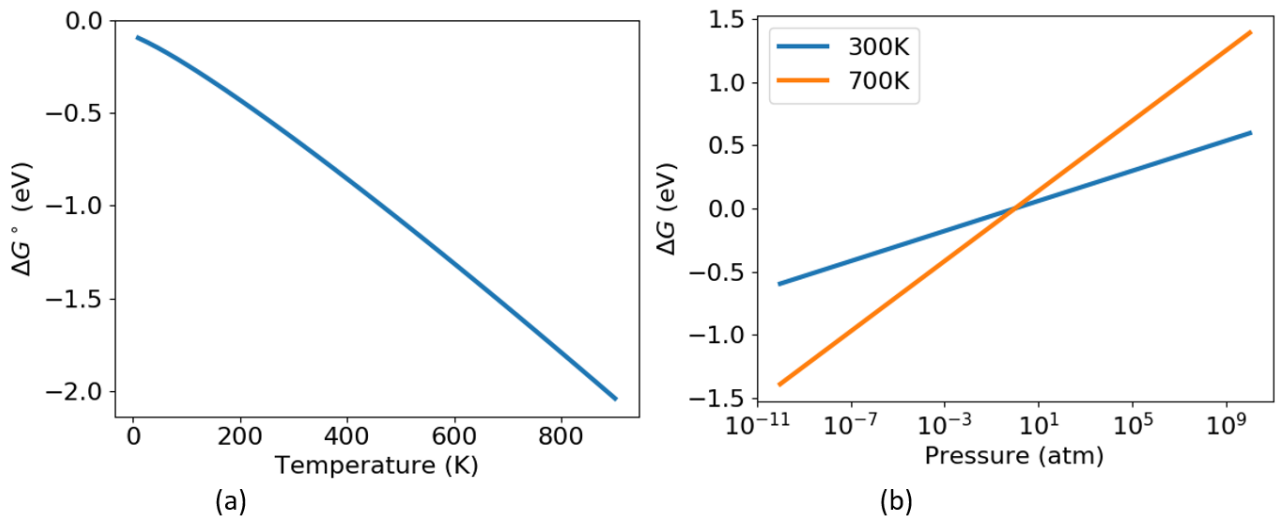
Figure 8.25: Gibbs free energy of O_2 gas (a) as a function of temperature at standard state (1 atm) and (b) as a function of pressure at 300 K and 700 K.

Let us now look at the stability of various oxygen coverage at the surface of Pt_{201} and Pt_{79} under realistic experimental conditions corresponding to a particular oxygen chemical potential. Equation 8.2 allows to directly plot the Gibbs free energy of adsorption as a function of oxygen chemical potential. On the basis of this, Figure 8.26 illustrates the Gibbs free energy adsorption of various coverage oxide over-layer as a function of oxygen chemical potential at 600 K with a range of partial pressures of O_2. Such type of plot can give a information about the stability of a particular coverage at a given $\Delta\mu_O$ under environmental (T, p) condition.

On the basis of Eq. 8.2 as presented in Figure 8.26, the limit of an infinitely dilute gas $(\mu_O(T, p) \to -\infty)$, a nanoparticle surface structure containing oxygen ($N_O \neq 0$) will exhibit an infinitely negative ΔG^{ad}, reflecting that it is very unfavorable to maintain oxygen adsorbed at the surface under such conditions. It means the bare surface will therefore always result as most stable in such environments. With increasing oxygen content in the gas phase, $\mu_O(T, p)$ will become less negative and the ΔG^{ad} becomes more positive (stable).

Here for Pt_{201} and Pt_{79} NPs, four and three oxygen coverages were considered, respectively. For the sake of comparison the bulk oxide is also included using its calculated heat of formation. The various coverages are represented with different colored lines and the slope of ΔG^{ad}-line is determined by fractional coverage Θ. The more oxygen contained in the nanoparticle, the more steeper is the slope. This high coverage structures become more favorable at higher oxygen chemical potential, while the bare structure is more stable at lower oxygen chemical potential. The bulk oxide red color coded line is clearly the steepest line and it becomes more stable than the bare nanoparticle for $\Delta\mu_O > -0.69$ eV (red dotted vertical line). The bulk oxide (PtO_2) is assumed to be the ultimate oxygen rich environment. The next steepest line is $\Theta = 0.56$ (0.53) for Pt_{201} (Pt_{79}) represented by solid green line and become more stable than the bare structure for $\Delta\mu_O > -0.75$ (−0.93) eV (green dotted vertical line). Finally the least coverage structure $\Theta = 0.22$ (0.23) become favorable at lower chemical potential ($\Delta\mu_O > -1.17$ (−1.12) eV) compared to the higher coverage structures. From the result we can see that higher coverage structures are more closer to the bulk oxide phase than the lower coverage structures.

Figure 8.26: Gibbs free energy of adsorption as a function of oxygen chemical potential $\Delta\mu_O$ for various oxygen coverage (a) on Pt_{201} and (b) on Pt_{79} nanoparticle surfaces at 600 K with a range of partial pressures of O_2. An adsorbate coverage phase is more stable than the bare nanoparticle surface (used as a reference), if its $\Delta G^{ad} > 0$ for some oxygen chemical potential at a given (T, p) condition. The vertical dashed lines (same color code as solid line counterpart) show the oxygen chemical potential limit. For values greater than the chemical potential of gaseous O_2, the different coverage structures become more stable than the bare structure.

The lower coverage structures slope is less steeper and more closer to the bare nanoparticle phase. In general, slight ΔG^{ad} differences are observed for Pt_{201} and Pt_{79} structures for similar coverages. The slight differences arise from the average adsorption energy differences. Most importantly, it should be pointed out that the structure for $\Theta = 0.56$ ML (the green line) is not the most stable at any pressure. This is also true for Pt_{79} structure at coverage of 0.53 ML at the given temperature. It can be concluded that at temperature T = 600 K the structures with coverage larger than 0.5 ML are not stable for both Pt_{79} and Pt_{201} nanoparticles and may not be observed.

In the following the temperature dependence of the Gibbs free energy of adsorption will be discussed. Figure 8.27 shows the Gibbs free energy of adsorption as a function of oxygen chemical potential for various oxygen coverage on Pt_{201} nanoparticle surface under pressure conditions of 1 atm and ultra high vacuum (UHV) 10^{-13} atm. These two pressures are selected since most of the studies in CO oxidation have been carried out either at UHV or in the range
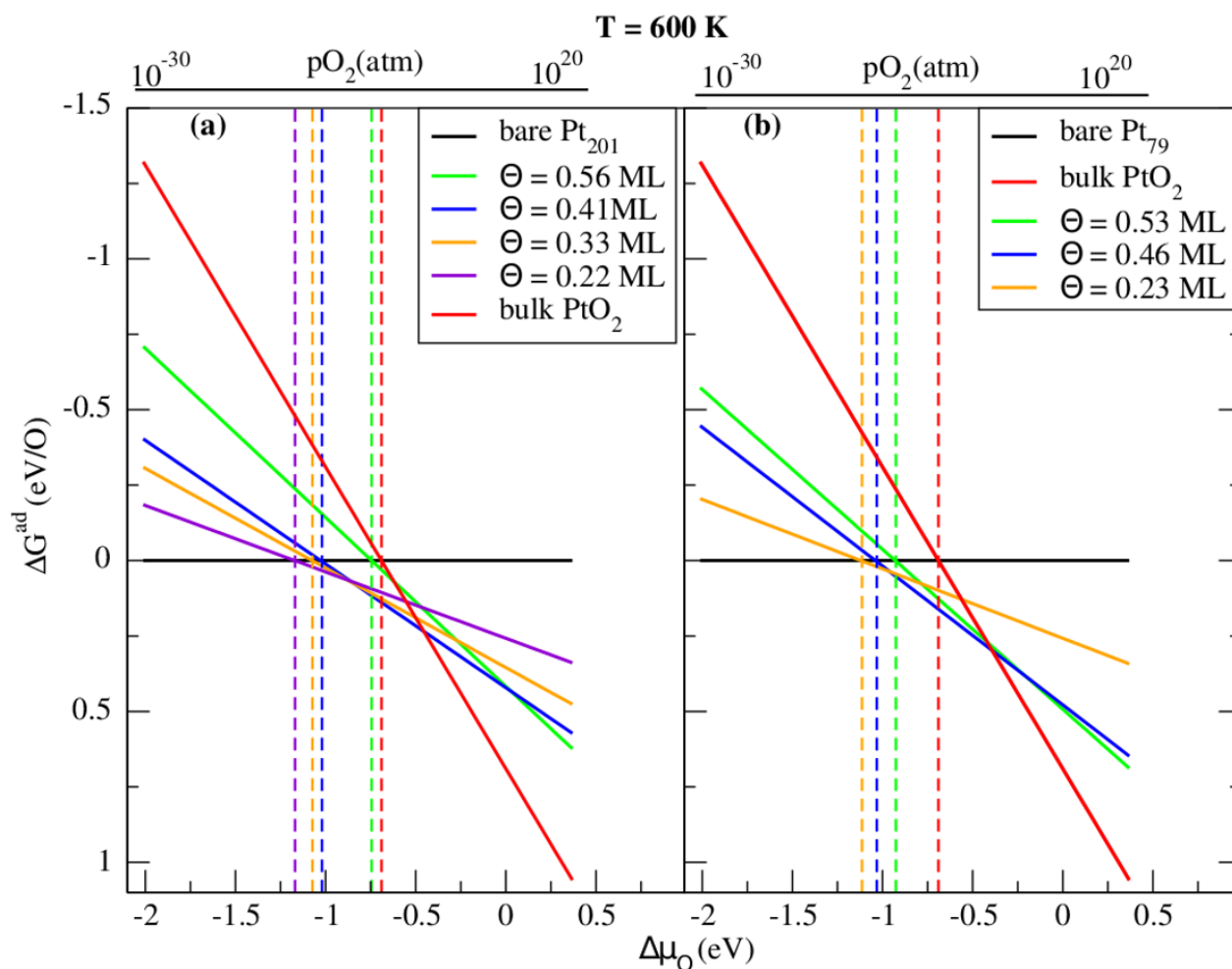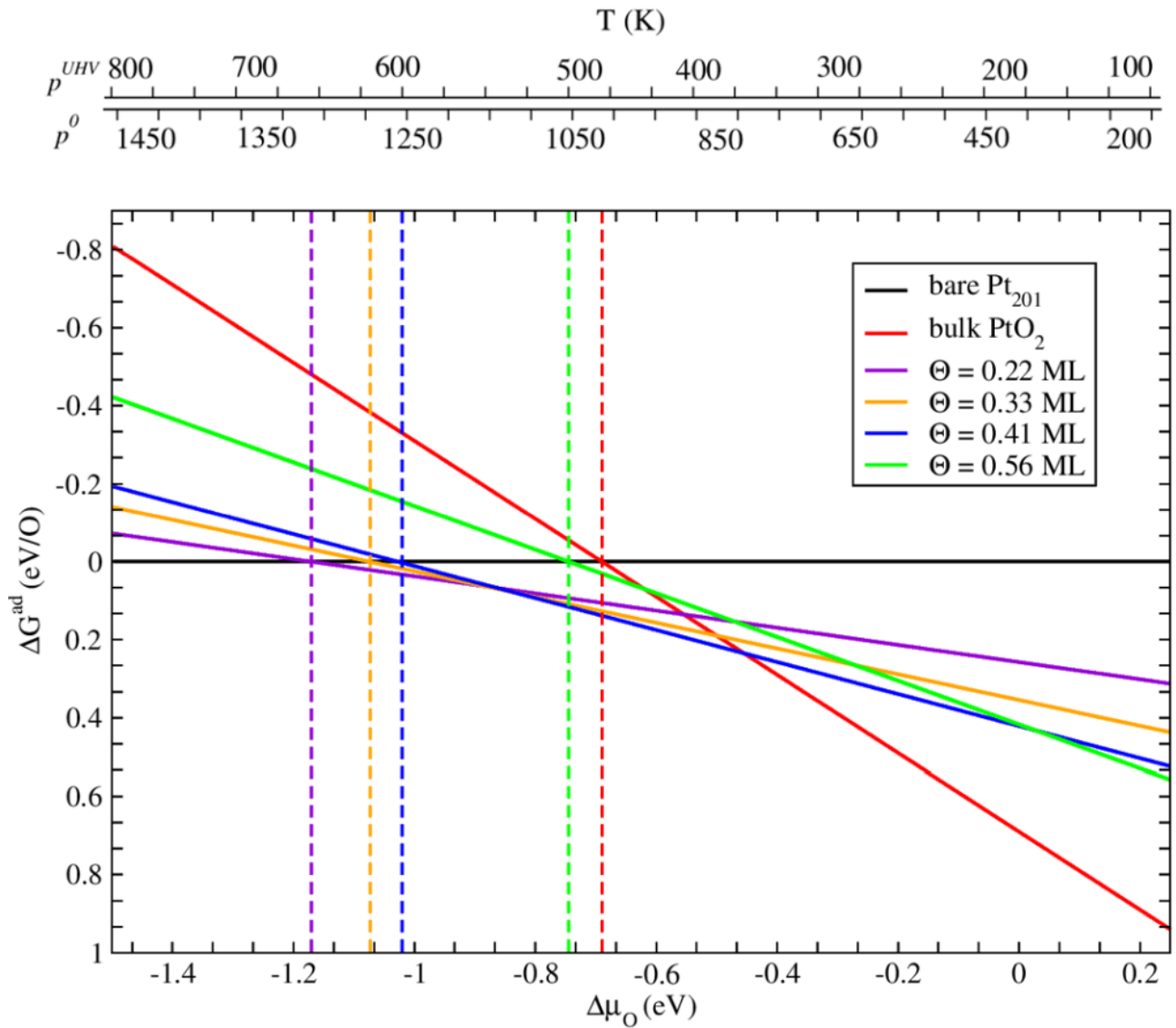
Figure 8.27: Gibbs free energy of adsorption as a function of oxygen chemical potential $\Delta\mu_O$ for various oxygen coverage on Pt_{201} nanoparticle surface. Temperature scales in Kelvin for values of $\Delta\mu_O$ at oxygen partial pressures corresponding to UHV (10^{-13} atm) and standard (1 atm) conditions are given at the top.

of 1 atm pressures [177, 185]. The temperature scales for the corresponding pressures are given on top of the plot. At higher temperature the value of $\Delta\mu_O$ is low and none of the coverages is stable below $\Delta\mu_O = -1.2$ eV. All the dotted vertical lines show the oxygen chemical potential value at which each coverages become stable on going from low chemical potential to high chemical potential. For instance, coverage $\Theta = 0.22$ ML become stable at $\Delta\mu_O = -1.17$ eV which corresponds to ≈ 650 K (at UHV) and 1300 K (at 1 atm). Analogously, the bulk PtO_2 becomes stable for $\Delta\mu_O > -0.69$ eV which corresponds to ≈ 480 K (at UHV) and 950 K (at 1 atm). The high coverage structure ($\Theta = 0.56$ ML) becomes stable at -0.75 eV which is closer to the bulk value of -0.69 eV.

8.4.5 Adsorbed oxygen diffusion barrier

The CO oxidation reaction can be affected by oxygen diffusion and diffusion of adsorbates in general is considered as part of the elementary steps in surface chemical reactions [176, 186, 187]. Here atomic oxygen diffusion from one site to the other is calculated on the surface of Pt_{79} using nudged elastic band (NEB) method [81].
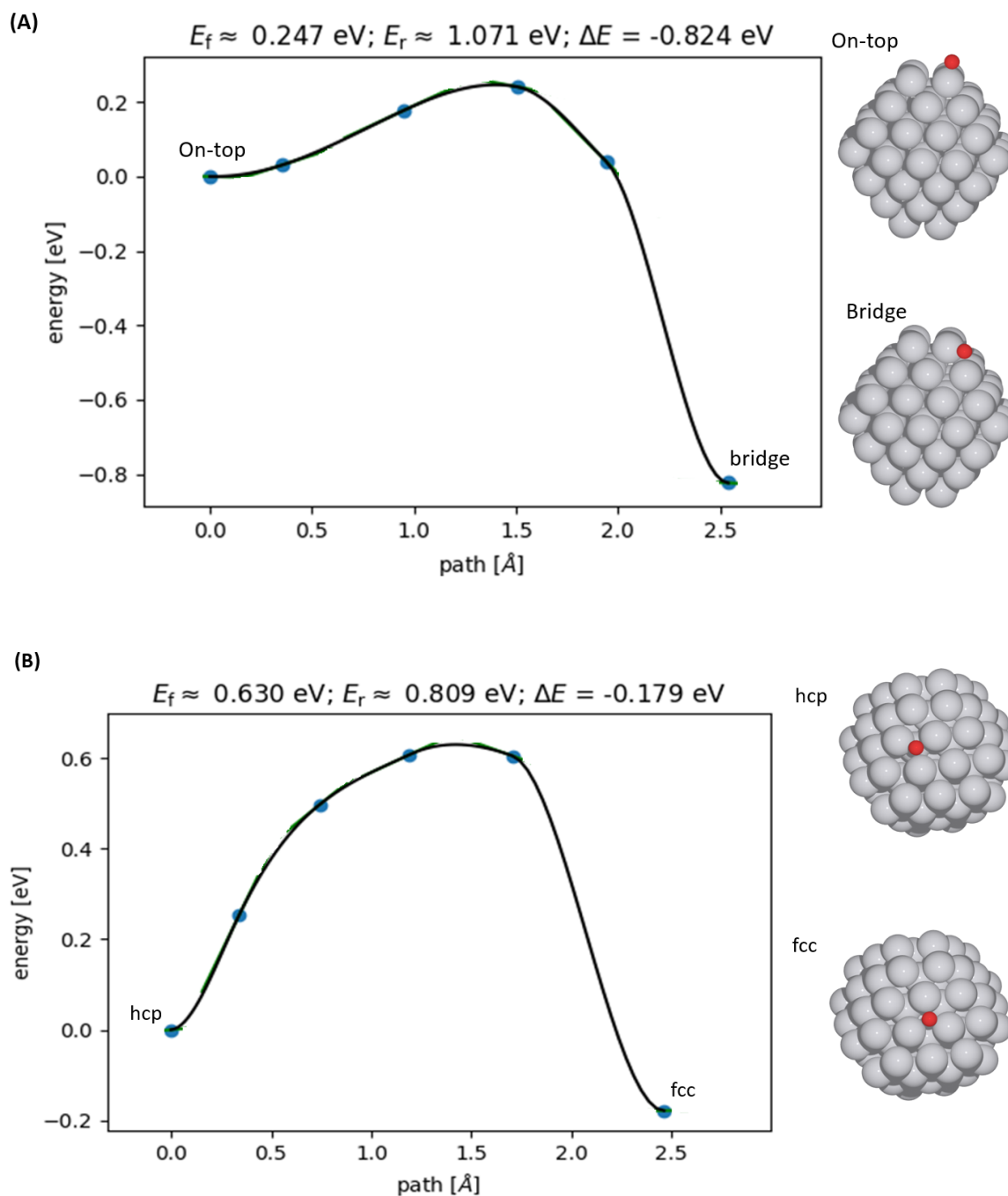
Figure 8.28: Atomic oxygen diffusion barrier on the surface of Pt_{79} as a function of diffusion path (A) from corner on-top site to edge-bridge site and (B) from hcp site to fcc site. The energy profiles are given at the very top in which E_f and E_r are the forward and reverse energy barriers, respectively and ΔE is the energy difference between initial and final point.

Figures 8.28 and 8.29 present oxygen diffusion profiles for the fcc, hcp, bridge and on-top sites. The diffusion barrier depends on oxygen binding strength. Previously we have seen the

adsorption strength of oxygen at various sites of Pt and Pd nanoparticles. Recall that oxygen favored 3-fold sites and the on-top sites adsorption is found to be comparably weak. The bridge sites adsorption have been determined to be unstable since the adsorbate O moved to 3-fold sites in the course of relaxation except at edge sites.
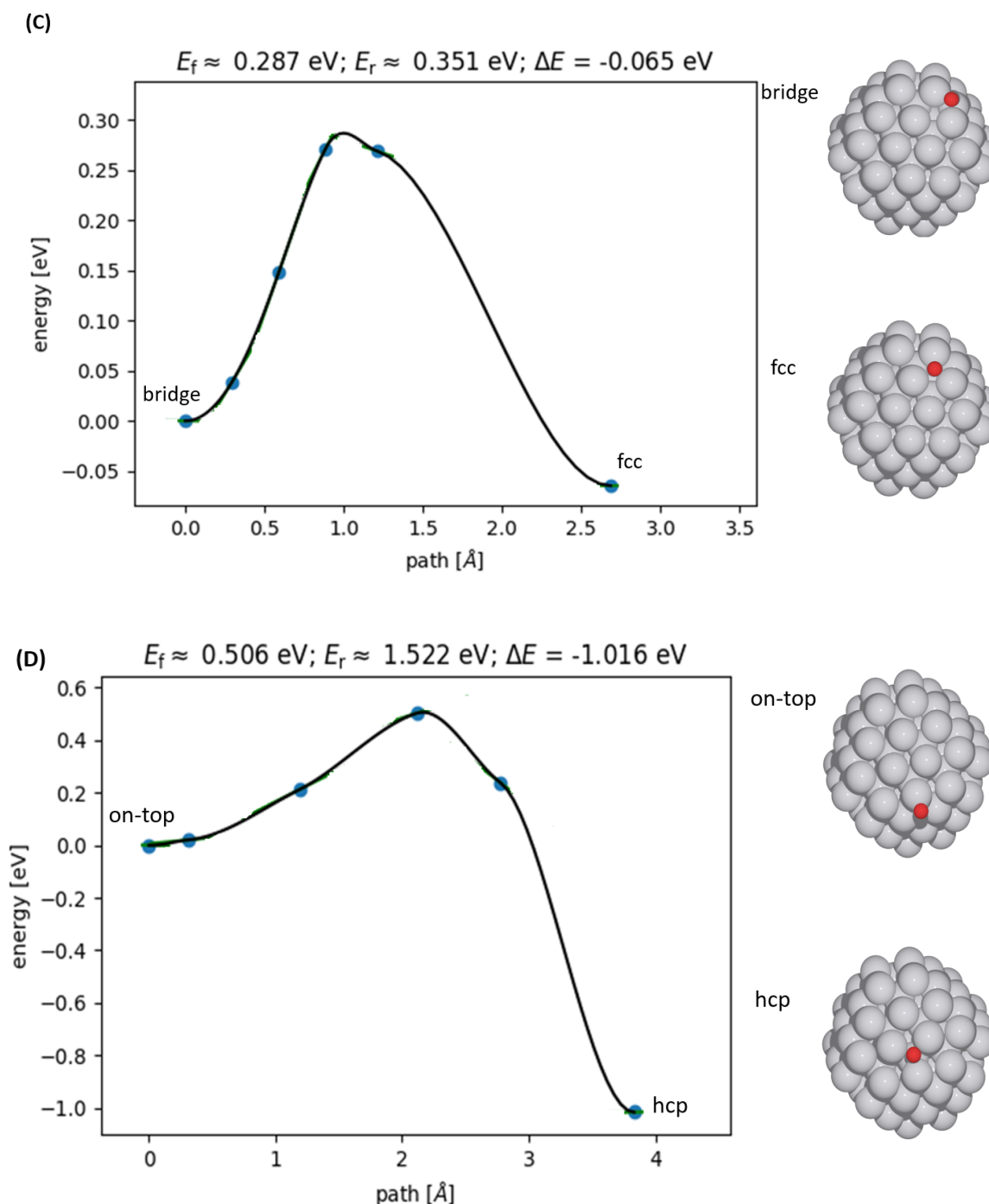
Figure 8.29: Atomic oxygen diffusion barrier on the surface of Pt_{79} as a function of diffusion path (C) from edge-bridge site to fcc site and (D) from on-top to hcp site. The energy profiles are given at the very top in which E_f and E_r are the forward and reverse energy barriers, respectively and ΔE is the energy difference between initial and final point.

Figure 8.28 (A) shows diffusion energy profile of oxygen from corner on-top to the next neighbor edge-bridge site in which the energy barriers for forward and the reverse diffusion are 0.247 eV and 1.071 eV, respectively. The low forward diffusion barrier can be attributed to

the weak on-top adsorption energy. The adsorption energies for these sites are 0.92 eV for the on-top site and 1.46 eV for the bridge site. The diffusion from hcp to a next neighboring fcc site over the bridge site is shown Figure 8.28 (B). The forward energy barrier of diffusion (hcp → fcc) is 0.63 eV and the reverse (fcc → hcp) is 0.809 eV. The calculated adsorption energy of hcp site is 1.22 eV and for the fcc is 1.37 eV. The hcp → fcc energy barrier 0.63 eV is in good agreement with the previous reported value of 0.58 eV even though it was calculated for Pt(111) slab surface [186]. Figure 8.29 (C) illustrates the diffusion from edge-bridge site to the next fcc site with forward (bridge → fcc) and reverse (fcc → bridge) energy barriers of 0.287 and 0.351 eV, respectively. The adsorption energies for the corresponding bridge site is 1.46 eV and for fcc site is 1.41 eV. These adsorption energies are relatively higher than other sites calculated for Pt_{79}. Furthermore, the diffusion of oxygen from edge on-top site to hcp site is calculated and the energy profiles are given in Figure 8.29 (C). The forward barrier is 0.506 eV and the reverse is 1.522 eV. As seen on the plot, the diffusion path covered is long $\approx$ 3.8 Å. This is because the initial on-top adsorption is slightly inclined to the other terrace side. This results to high diffusion barrier (0.506 eV) for the weak on-top site adsorption. The oxygen adsorption for the on-top site is 0.52 eV and for hcp site is 1.22 eV. Overall, it was found that the diffusion barrier is correlated with the adsorption energy. Consequently, on-top and bridge site diffusion barrier is low while the 3-fold sites barrier is relatively high. I am not aware of other studies for diffusion of oxygen at nanoparticle surface to compare.

8.4.6 Ab initio molecular dynamics simulation on oxygen coverage

The CO oxidation catalysts are exposed to an oxidative environment at operating temperature of usually between 300 to 600 K. In order to evaluate the effects of temperature on the evolution of oxygen covered nanoparticles, ab initio molecular dynamics (AIMD) simulations was applied. AIMD simulations were performed by employing the NVT ensemble at 450 K using the Nosé–Hoover thermostat. The equation of motion is solved via velocity Verlet algorithm with a time step of 3 fs for a total simulation time of 12 ps, i.e., 4000 steps were performed. The degree of distortion of nanoparticles and formation of oxide layer is analyzed using pair correlation or radial distribution function g(r). Figure 8.30 shows the Pt-Pt radial distribution function (RDF) at various coverage on Pt_{79} nanoparticle simulated at 450 K. Evidently, it can be seen that the nanoparticle geometry depend on the oxygen coverage. The first peak at about 2.70 Å shows the average distance to the first nearest neighbors. Further, the pronounced peaks at distance 4.67 and 5.26 Å reflect the Pt atoms in the edges and corners of the nanoparticle. It should be noted that the peak at distance 5.26 Å is observed only for the bare Pt_{79}, while it disappears for oxygen covered Pt_{79} indicating that corners atoms are distorted as consequence of interaction with oxygen. The broadened blue line represents the highest coverage (Θ = 0.51 ML), whereas the black sharp peak shows the oxygen free bare Pt_{79} nanoparticle. Consequently, the results suggest that the nanoparticles geometry is more distorted for higher oxygen coverage than the lower coverage due to adsorbate Pt interaction. An example of AIMD simulation steps trajectory for coverage 0.22 ML is shown in Figure 8.31. Inspecting the structures at different
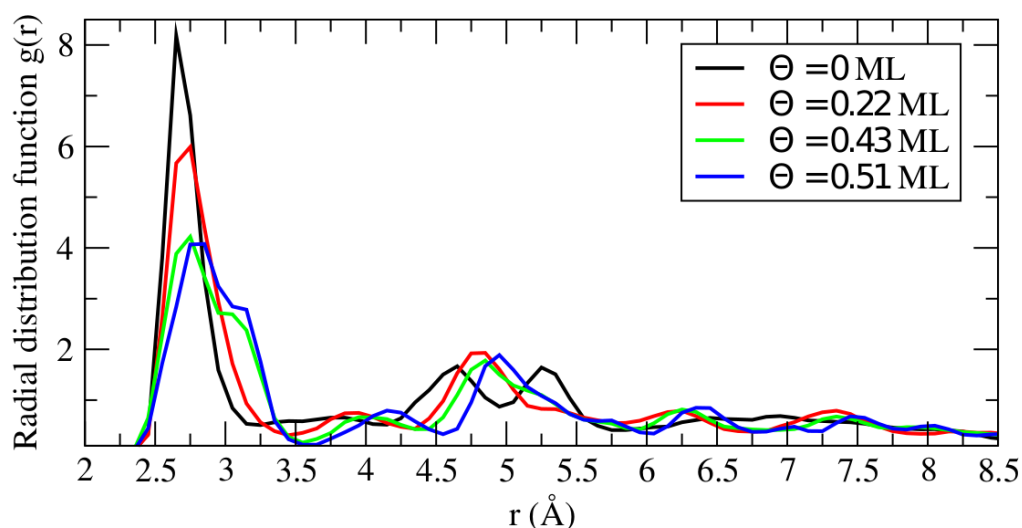
Figure 8.30: The Pt-Pt RDF for various oxygen coverage on Pt_{79}. These RDF is the average of the last 1000 steps. The black line represents the bare Pt_{79} and red, green and blue lines represent coverage of 0.22, 0.43 and 0.51 ML.

time steps, we can see structural deformation at 3 ps and then restoration at 12 ps. The (100) cut at the corner was observed to be the most susceptible to undergo deformation.
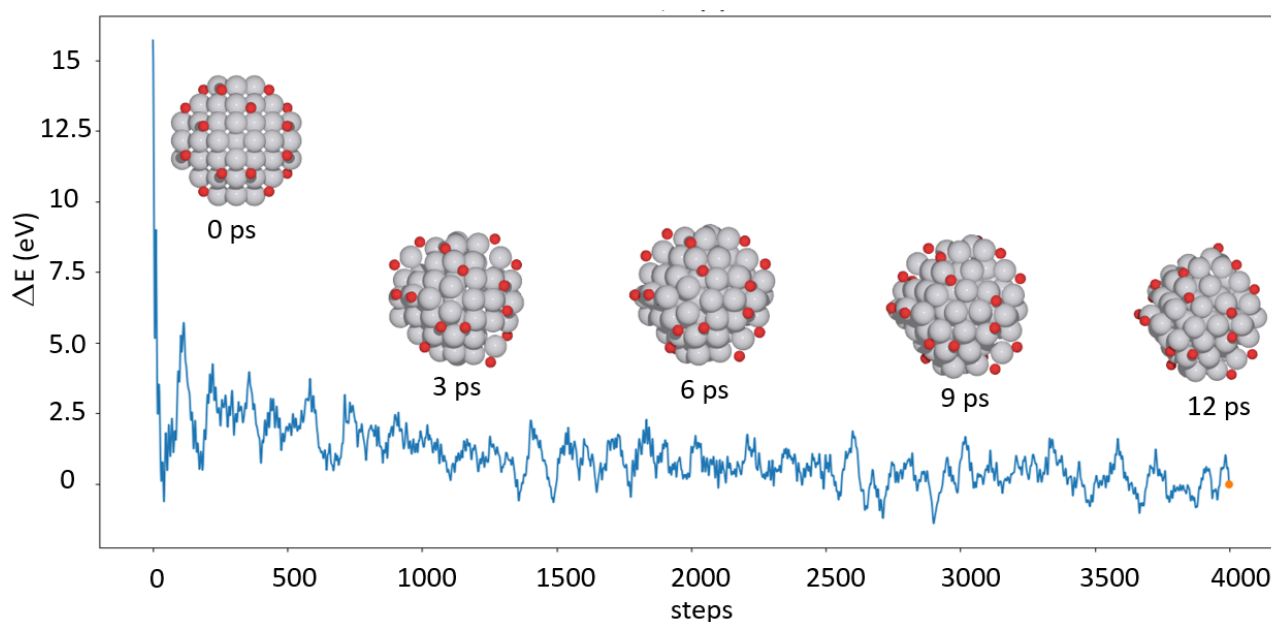
Figure 8.31: AIMD simulation trajectories for coverage of 0.22 ML on Pt_{79} at 450 K. The x-axis shows the ionic steps and y-axis shows energy difference between two consecutive steps $[\Delta E = E(i) - E(i-1)]$. The structural evolution with time at 0, 3, 6, 9 and 12 picoseconds (ps) are also shown.

In order to analyze the temperature effect on the geometry of oxygen covered nanoparticle, the locally relaxed structure RDF is plotted with the molecular dynamics simulated geometry as shown in Figure 8.32. The black and green lines show relaxed structures of coverage 0.22 and 0.51 ML, respectively. The red and blue lines represent AIMD simulated structures. As clearly seen, the AIMD simulated structures RDF are broadened indicating the structural deformation, whereas the locally optimized structures relatively remains to be less deformed. The locally
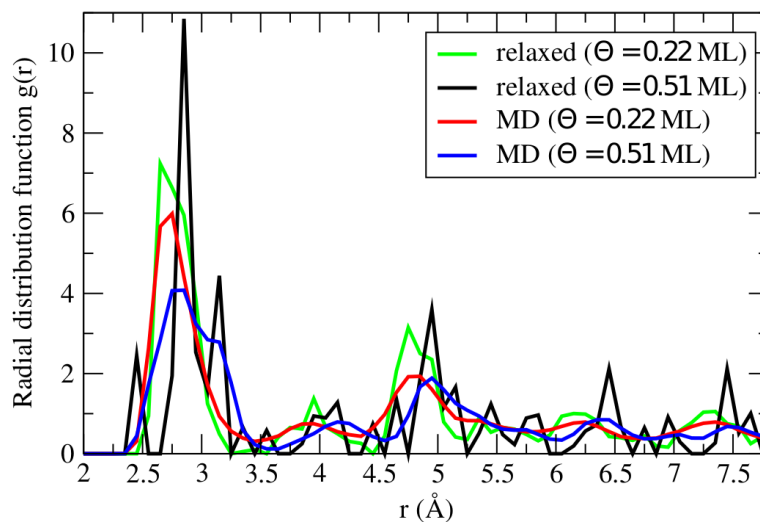
Figure 8.32: Comparison of locally relaxed and AIMD simulated Pt-Pt pair correlation function g(r) for oxygen covered Pt$_{79}$. The AIMD g(r) is the average of the last 1000 steps. The green and black lines represent the locally optimized structures, while red and blue represent AIMD simulated structures.

optimized structure for $\Theta = 0.51$ ML shows three peaks in the first neighbor coordination, below 3.2 Å distance. The first peak at distance of 2.49 Å is the Pt-Pt pair correlation of corner Pt atoms. The second peak which is most abundant at distance 2.86 Å correspond to pair correlation between core shell Pt atoms and core to surface atoms. The peak at radius 3.15 reflects pair correlation between edge atoms and edge to (111) terrace atoms. The reason for the existence of these three peaks is strain effect of oxygen segregation near to corners and edges of the nanoparticle in all sides equally, which results to bond elongation between edge atoms and shortening at corner atoms. On the other hand, the locally optimized structure of coverage 0.22 ML shows only one broad peak in the first nearest neighbor coordination, indicating that the strain due to oxygen adsorption is not large. Moreover, the other peaks for r > 3.5 Å represent second and third nearest neighbor atoms.

The finding from this study suggest that oxide formed due to coverage is only surface oxide overlayer. The next interesting question related to oxygen coverage might be how similar is the nanoparticle oxide overlayer with bulk oxide. Figure 8.33 illustrates the Pt-O pair correlation of three oxygen coverages and the two bulk oxides of platinum (PtO and PtO$_2$). The red and black shaded peaks designate the bulk PtO and PtO$_2$ structures, respectively. The dominant peak at distance 2.06 Å represents the first nearest neighbor coordination of Pt with O and all coverage structures overlie with the bulk oxides. The first coordination is only with surface Pt atoms. The second nearest neighbor coordination is also appeared with bulk PtO at distance 3.76 Å. To sum up, core shell oxide formation was not observed even with long time temperature treatment and only oxide overlayer is formed. The oxide overlayer at some sites has shown segregation to sub-surface. Neither PtO nor PtO$_2$ has similarity with oxide formed due oxygen coverage.
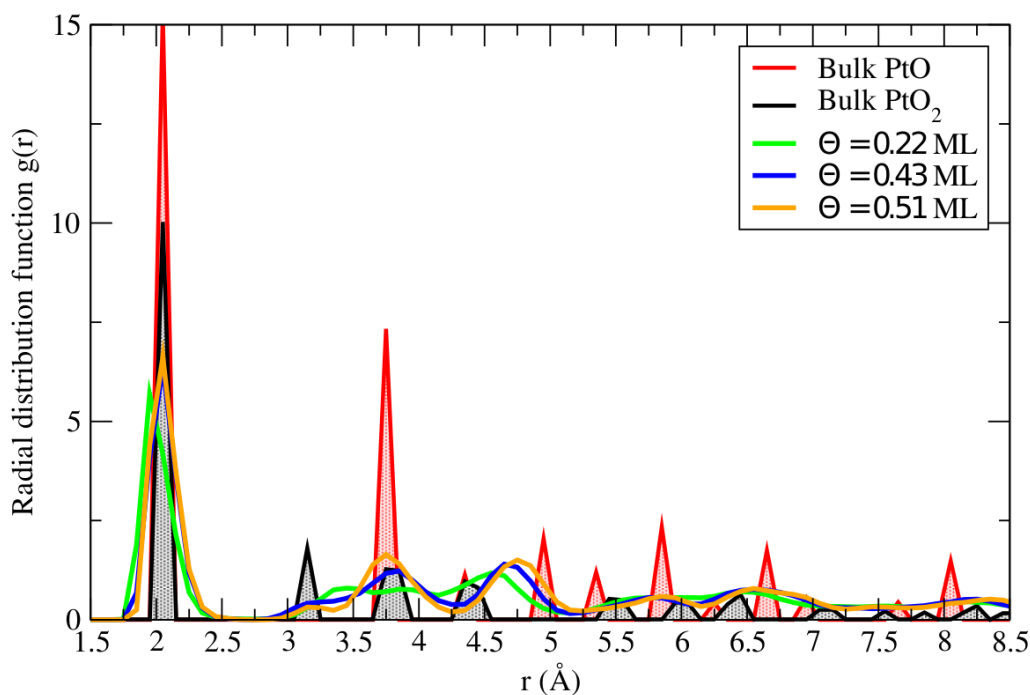
Figure 8.33: Comparison of Pt-O pair correlation g(r) for AIMD simulated oxygen covered Pt$_{79}$ nanoparticle with bulk Pt oxides. The AIMD g(r) is the average of the last 1000 steps. The shaded red and black peaks represent bulk PtO and PtO$_2$, respectively. The green, blue and orange lines oxide overlayer structure of coverage 0.22, 0.43 and 0.51 ML.

8.5 Conclusions

In this chapter, I have studied the adsorption properties of CO and O on nanoparticles of Pt and Pd. Various nanoparticle sizes, shapes and adsorption sites are investigated. The overall adsorption properties of Pd and Pt have similarities, however different CO and O adsorption strength is obtained. For the systems studied here the most influential factors on the adsorption energy are adsorption site and nanoparticle shape than nanoparticle size. The nanoparticles with mixture of (111) and (100) facets have shown higher adsorption energies than the nanoparticles with only (111) facets. Thus, for both CO and O cuboctahedron and truncated octahedron nanoparticles have shown higher adsorption energy than the regular octahedron nanoparticles. Generally, in comparison to terrace sites with higher $\overline{\text{CN}}$, the defect sites with lower $\overline{\text{CN}}$ have shown higher adsorption energy. For O, the most favored adsorption sites are the 3-fold sites for both Pt and Pd. The CO vibrational frequencies are calculated for various sites on Pt and Pd nanoparticles. The CO vibrational spectra at on-top, bridge, and 3-fold sites of Pt and Pd surfaces are found in the ranges $2050 - 2106$ cm^{-1}, $1890 - 1930$ cm^{-1} and $1750 - 1850$ cm^{-1}, respectively. Oxygen coverage at different Pt nanoparticles size is examined in order to understand the surface structure change under various coverage. The results suggested that the adsorption energy per atom decreases with coverage. Furthermore, the thermodynamic stability of oxygen covered nanoparticles are studied under experimental relevant conditions.

Chapter 9

Summary

In this thesis, Pt and Pd clusters have been studied with respect to their structural and catalytic properties since they are known to show high catalytic activity. In the first part of this thesis, structures of small platinum clusters Pt_n^- (n = 6–13) have been studied. The determination of the structures of small metal clusters is a challenge for theory as well as for experiment. However, a combination of quantum chemical calculations and trapped ion electron diffraction spectroscopy (TIED) has been successfully used on other metals in the past [13]. In cooperation with D. Bumüller and D. Schooss (Institute of Nanotechnology, KIT), structures were assigned based on the best structural agreement obtained by comparison of their measured scattering functions to those obtained from calculations. Different isomers for each cluster size were obtained by a DFT based genetic algorithm. For the low energy structures obtained in the genetic algorithm as well as for further promising motifs proposed by Bumüller and Schooss, structure optimizations were repeated with larger basis sets and the TPSS functional. Only for a few cluster sizes, structures with the lowest energy at DFT level match the experimental data. Often structures with slightly higher energies show better agreement with experiment. It should be pointed out that several isomers were obtained within a small energy range. In several cases, small changes in the setup of the calculation, e.g., usage of different DFT functionals, affects the order of the isomers. This makes the structural assignment based solely on calculations uncertain. The inclusion of spin-orbit coupling reduces the energy gaps between isomers. Among the investigated structures, Pt_6^- was the only planar structure. Thus, transition from 2D to 3D occurs between Pt_6^- and Pt_7^-. This is in between the behavior of Pd and Au clusters, where already Pd_4^- has a non-planar structure [45] while Au clusters have planar motifs up to $n = 12$ because of relativistic effects [188]. Compact hcp cut structures are assigned for Pt_{12}^- and Pt_{13}^- based on comparison of the theoretical and experimental data profile factor. For all calculated structures further properties such as cohesive energies, average bond lengths, density of states and HOMO-LUMO gaps were calculated. For all structures, small HOMO-LUMO gaps between 0.07 and 0.5 eV were obtained. Moreover, vibrational frequencies were evaluated, which in combination with measured spectra could provide an additional criterion for structure assignment in the future.

In part two of this thesis, adsorption properties of CO and oxygen on surfaces of Pd and Pt nanoparticles were studied. Various Pt and Pd clusters with different sizes (n = 38–201) and

morphologies were considered and the differences in adsorption properties were investigated. In agreement with former studies, it was observed that upon adsorption, the CO bond length $d_{\text{C-O}}$ is increased when going from one-fold to 3-fold coordinated adsorption sites. The changes in $d_{\text{C-O}}$ were similar for Pt and Pd clusters. For the on-top sites, the average value of $d_{\text{C-O}}$ is 1.161 Å. On the bridge (2-fold) site, $d_{\text{C-O}}$ is in the range 1.184 Å, which is ≈ 0.02 Å longer than for the on-top site. For 3-fold sites, the value of $d_{\text{C-O}}$ is in range 1.195 Å. Regardless of the structural details, i.e., clusters size and adsorption sites (corners, edges or terraces), $d_{\text{C-O}}$ is very similar for all on-top sites (1.161±0.002 Å), bridge sites (1.184±0.001 Å) and hollow sites (1.195±0.003 Å).

According to the calculations, the CO adsorption energy is highly influenced by the local surface geometry. For example, on Pt_{201} and Pd_{201} surfaces, the adsorption energies are calculated in the range $1.56 - 2.14$ eV and $1.35 - 2.07$ eV, respectively. The effect of the adsorption site is the more influential factor than shape and size. On nanoparticles that contain both (111) and (100) surfaces and defect sites (corners and edges) larger adsorption energies were obtained for the same type of adsorption sites. Cuboctahedron and truncated octahedron nanoparticles exhibit larger adsorption energies than regular octahedron nanoparticles with only (111) planes. Significant differences in the adsorption energies were obtained for positions close to the edge of the surface compared to higher coordinated sites. For example, up to 0.58 eV difference is obtained for the on-top CO adsorption on Pt_{201}, in which the larger was calculated at the corner sites and the smaller was on terrace sites. For the on-top sites, the adsorption energies on Pt nanoparticles is always higher than on Pd nanoparticles. For 3-fold hollow sites, it is the opposite, the adsorption energies are higher for Pd clusters. This is consistently observed regardless of size and shape for all nanoparticles studied in this work.

The CO vibrational frequencies were investigated for all possible unique adsorption sites on the nanoparticles. Generally, the on-top, bridge, and 3-fold sites of Pt and Pd surfaces are found in the ranges $2050 - 2106$ cm^{-1}, $1890 - 1930$ cm^{-1} and $1750 - 1850$ cm^{-1}, respectively. These results are in agreement with former studies [101–103]. Thus, from the calculated vibrational frequencies it is straightforward to identify the on-top, bridge and 3-fold hollow site CO adsorption. These results can be useful to interpret measurements of vibrational frequencies on the nanoparticle surfaces. Monotonic increase of vibrational frequencies with generalized coordination number, which can tell whether CO is adsorbed at the terrace or other defect sites were obtained for the on-top sites of Pt and Pd. However, the bridge and 3-fold sites did not show a similar monotonic trend. Moreover, no systematic variation of CO stretching frequencies with nanoparticle sizes were obtained. The calculated CO vibrational frequencies were higher in the presence of oxygen. The effect is increased for higher coverages.

Similar to CO, the adsorption properties of atomic oxygen on the various nanoparticles of Pt and Pd surfaces have been studied. It was found that O prefers the 3-fold hollow sites for both Pt and Pd particles which is in line with other theoretical [129] and experimental [165, 166] studies. The on-top site adsorption energy is the lowest compared to other sites. Oxygen is not stable at bridge sites (except edge-bridge) and it diffuses to the nearby three-fold sites of the nanoparticles which agree well with other reported works [137, 167]. Generally, comparing

to truncated octahedron and cuboctahedron nanoparticles, much smaller adsorption energies are obtained for regular octahedron nanoparticles. Furthermore, various oxygen coverages were investigated on Pt_{201} and Pt_{79} nanoparticles. As a result, it was observed that the maximum possible coverage for which the oxygen atoms remain at the hollow sites where they were placed initially is about 0.5 ML. In all cases, the average adsorption energy per atom decreases with increase of coverage. Finally, core shell oxide formation was not observed on Pt_{79} performing an ab initio molecular dynamics run using the Nosé–Hoover thermostat at 450 K for 12ps.

With the aim that the data generated in this work can be used for future purpose, I have designed a data model using the MongoDB database program and the relevant information of this work are stored there. The data stored includes the structures, technical details of the calculations such as DFT functionals, cutoff energy, convergence criteria, etc and properties (energies, adsorption energies, vibrational frequencies, etc). Such a database can be used as data source for secondary complex simulation such as micro-kinetic modeling and machine learning. The database repository is located at the HPC computers of the Steinbuch Centre for Computing (SCC).

Bibliography

[1] Z. Ma, F. Zaera, *Encyclopedia of Inorganic Chemistry* **2006**.

[2] I. Chorkendorff, J. W. Niemantsverdriet, *Concepts of modern catalysis and kinetics*, John Wiley & Sons, **2017**.

[3] A. Zecchina, S. Califano, *The Development of Catalysis: A History of Key Processes and Personas in Catalytic Science and Technology*, John Wiley & Sons, **2017**.

[4] A. Vojvodic, A. J. Medford, F. Studt, F. Abild-Pedersen, T. S. Khan, T Bligaard, J. Nørskov, *Chemical Physics Letters* **2014**, *598*, 108–112.

[5] B. Qiao, A. Wang, X. Yang, L. F. Allard, Z. Jiang, Y. Cui, J. Liu, J. Li, T. Zhang, *Nature chemistry* **2011**, *3*, 634.

[6] L. Nie, D. Mei, H. Xiong, B. Peng, Z. Ren, X. I. P. Hernandez, A. DeLaRiva, M. Wang, M. H. Engelhard, L. Kovarik, A. Datye, *Science* **2017**, *358*, 1419–1423.

[7] U Heiz, A Sanchez, S Abbet, W.-D. Schneider, *Journal of the American Chemical Society* **1999**, *121*, 3214–3217.

[8] A. D. Allian, K. Takanabe, K. L. Fujdala, X. Hao, T. J. Truex, J. Cai, C. Buda, M. Neurock, E. Iglesia, *Journal of the American Chemical Society* **2011**, *133*, 4498–4517.

[9] M. A. van Spronsen, J. W. Frenken, I. M. Groot, *Chemical Society Reviews* **2017**, *46*, 4347–4374.

[10] H. Liu, J. Guan, X. Mu, G. Xu, X. Wang, X. Chen, *Encyclopedia of Physical Organic Chemistry* **2016**, 1–75.

[11] Y. Xu, R. B. Getman, W. A. Shelton, W. F. Schneider, *Physical Chemistry Chemical Physics* **2008**, *10*, 6009–6018.

[12] S. N. Rashkeev, A. R. Lupini, S. H. Overbury, S. J. Pennycook, S. T. Pantelides, *Physical Review B* **2007**, *76*, 035438.

[13] E. Waldt, A.-S. Hehn, R. Ahlrichs, M. M. Kappes, D. Schooss, *The Journal of chemical physics* **2015**, *142*, 024319.

[14] P. Gruene, B. Butschke, J. T. Lyon, D. M. Rayner, A. Fielicke, *Zeitschrift für Physikalische Chemie* **2014**, *228*, 337–350.

[15] I. V. Yudanov, R. Sahnoun, K. M. Neyman, N. Rösch, J. Hoffmann, S. Schauermann, V. Johanek, H. Unterhalt, G. Rupprechter, J. Libuda, H. Freund, *The Journal of Physical Chemistry B* **2003**, *107*, 255–264.

[16] J. K. Nørskov, T. Bligaard, B. Hvolbæk, F. Abild-Pedersen, I. Chorkendorff, C. H. Christensen, *Chemical Society Reviews* **2008**, *37*, 2163–2171.

[17] G. Jones, J. G. Jakobsen, S. S. Shim, J. Kleis, M. P. Andersson, J. Rossmeisl, F. Abild-Pedersen, T. Bligaard, S. Helveg, B. Hinnemann, J. Rostrup-Nielsen, *Journal of Catalysis* **2008**, *259*, 147–160.

[18] J. Brönsted, K. Pedersen, *Zeitschrift für Physikalische Chemie* **1924**, *108*, 185–235.

[19] M. M. Montemore, J. W. Medlin, *Catalysis Science & Technology* **2014**, *4*, 3748–3761.

[20] C. Draxl, M. Scheffler, *arXiv preprint arXiv:1904.05859* **2019**.

[21] K. Alberi, M. B. Nardelli, A. Zakutayev, L. Mitas, S. Curtarolo, A. Jain, M. Fornari, N. Marzari, I. Takeuchi, M. L. Green, M Kanatzidis, *Journal of Physics D: Applied Physics* **2018**, *52*, 013001.

[22] L. De Jongh, *Physics and chemistry of metal cluster compounds: model systems for small metal particles*, *Vol. 18*, Springer Science & Business Media, **2013**.

[23] T. Tsukuda, H. Häkkinen, *Protected metal clusters: from fundamentals to applications*, *Vol. 9*, Elsevier, **2015**.

[24] S. Vajda, M. J. Pellin, J. P. Greeley, C. L. Marshall, L. A. Curtiss, G. A. Ballentine, J. W. Elam, S. Catillon-Mucherie, P. C. Redfern, F. Mehmood, P Zapol, *Nature materials* **2009**, *8*, 213.

[25] M. Haruta, *Catalysis today* **1997**, *36*, 153–166.

[26] A. Cox, J. Louderback, S. Apsel, L. Bloomfield, *Physical Review B* **1994**, *49*, 12295.

[27] D. Harding, M. S. Ford, T. R. Walsh, S. R. Mackenzie, *Physical Chemistry Chemical Physics* **2007**, *9*, 2130–2136.

[28] C. Adlhart, E. Uggerud, *The Journal of chemical physics* **2005**, *123*, 214709.

[29] C. Adlhart, E. Uggerud, *Chemical Communications* **2006**, 2581–2582.

[30] P. Weis, *International Journal of Mass Spectrometry* **2005**, *245*, 1–13.

[31] D. Schooss, P. Weis, O. Hampe, M. M. Kappes, *Philosophical Transactions of the Royal Society A: Mathematical Physical and Engineering Sciences* **2010**, *368*, 1211–1243.

[32] K. Yamamoto, T. Imaoka, W.-J. Chun, O. Enoki, H. Katoh, M. Takenaga, A. Sonoi, *Nature chemistry* **2009**, *1*, 397.

[33] S. Guo, S. Zhang, S. Sun, *Angewandte Chemie International Edition* **2013**, *52*, 8526–8544.

[34] F. F. Schweinberger, M. J. Berr, M. Doblinger, C. Wolff, K. E. Sanwald, A. S. Crampton, C. J. Ridge, F. Jackel, J. Feldmann, M. Tschurl, U Heiz, *Journal of the American Chemical Society* **2013**, *135*, 13262–13265.

[35] T. Imaoka, H. Kitazawa, W.-J. Chun, S. Omura, K. Albrecht, K. Yamamoto, *Journal of the American Chemical Society* **2013**, *135*, 13089–13095.

[36] T. Imaoka, H. Kitazawa, W.-J. Chun, K. Yamamoto, *Angewandte Chemie International Edition* **2015**, *54*, 9810–9815.

[37] E. C. Tyo, S. Vajda, *Nature nanotechnology* **2015**, *10*, 577.

[38] M. Nesselberger, M. Roefzaad, R. F. Hamou, P. U. Biedermann, F. F. Schweinberger, S. Kunz, K. Schloegl, G. K. Wiberg, S. Ashton, U. Heiz, K. Mayrhofer, *Nature materials* **2013**, *12*, 919.

[39] A. Nie, J. Wu, C. Zhou, S. Yao, C. Luo, R. C. Forrey, H. Cheng, *International Journal of Quantum Chemistry* **2007**, *107*, 219–224.

[40] V. Kumar, Y. Kawazoe, *Physical Review B* **2008**, *77*, 205418.

[41] L. Xiao, L. Wang, *The Journal of Physical Chemistry A* **2004**, *108*, 8605–8614.

[42] V. Fung, D.-e. Jiang, *The Journal of Physical Chemistry C* **2017**, *121*, 10796–10802.

[43] I. Demiroglu, K. Yao, H. A. Hussein, R. L. Johnston, *The Journal of Physical Chemistry C* **2017**, *121*, 10773–10780.

[44] A. S. Chaves, G. G. Rondina, M. J. Piotrowski, P. Tereshchuk, J. L. Da Silva, *The Journal of Physical Chemistry A* **2014**, *118*, 10813–10821.

[45] A. S. Chaves, M. J. Piotrowski, J. L. Da Silva, *Physical Chemistry Chemical Physics* **2017**, *19*, 15484–15502.

[46] X. Xing, A. Hermann, X. Kuang, M. Ju, C. Lu, Y. Jin, X. Xia, G. Maroulis, *Scientific reports* **2016**, *6*, 19656.

[47] B. Kalita, R. C. Deka, *The Journal of chemical physics* **2007**, *127*, 244306.

[48] M. P. Johansson, I. Warnke, A. Le, F. Furche, *The Journal of Physical Chemistry C* **2014**, *118*, 29370–29377.

[49] R. Li, M. Odunlami, P. Carbonnière, *Computational and Theoretical Chemistry* **2017**, *1107*, 136–141.

[50] D. J. Wales, M. A. Miller, T. R. Walsh, *Nature* **1998**, *394*, 758.

[51] Y Xiang, D. Sun, X. Gong, *The Journal of Physical Chemistry A* **2000**, *104*, 2746–2751.

[52] H. Do, N. A. Besley, *The Journal of chemical physics* **2012**, *137*, 134106.

[53] R. L. Johnston, T. V. Mortimer-Jones, C. Roberts, S. Darby, F. R. Manby in Workshops on Applications of Evolutionary Computation, Springer, **2002**, pp. 92–101.

[54] B. Hartke, *Wiley Interdisciplinary Reviews: Computational Molecular Science* **2011**, *1*, 879–887.

[55]   S. Heiles, R. L. Johnston, *International Journal of Quantum Chemistry* **2013**, *113*, 2091–2109.

[56]   R. Car, M. Parrinello, *Physical review letters* **1985**, *55*, 2471.

[57]   D. Wales, J. P. Doye, *The Journal of Physical Chemistry A* **1997**, *101*, 5111–5116.

[58]   B. Hartke, *The Journal of Physical Chemistry* **1993**, *97*, 9973–9976.

[59]   R. L. Johnston, *Dalton Transactions* **2003**, 4193–4207.

[60]   D. M. Deaven, K.-M. Ho, *Physical review letters* **1995**, *75*, 288.

[61]   M. Sierka, *Progress in Surface Science* **2010**, *85*, 398–434.

[62]   D. Schooss, M. N. Blom, J. H. Parks, B. v. Issendorff, H. Haberland, M. M. Kappes, *Nano letters* **2005**, *5*, 1972–1977.

[63]   M. N. Blom, D. Schooss, J. Stairs, M. M. Kappes, *The Journal of chemical physics* **2006**, *124*, 244308.

[64]   R. Ahlrichs, M. Bär, M. Häser, H. Horn, C. Kölmel, *Chemical Physics Letters* **1989**, *162*, 165–169.

[65]   F. Weigend, R. Ahlrichs, *Physical Chemistry Chemical Physics* **2005**, *7*, 3297–3305.

[66]   A. D. Becke, *Physical review A* **1988**, *38*, 3098.

[67]   J. P. Perdew, K. Burke, M. Ernzerhof, *Physical review letters* **1996**, *77*, 3865.

[68]   J. Tao, J. P. Perdew, V. N. Staroverov, G. E. Scuseria, *Physical Review Letters* **2003**, *91*, 146401.

[69]   V. N. Staroverov, G. E. Scuseria, J. Tao, J. P. Perdew, *The Journal of chemical physics* **2003**, *119*, 12129–12137.

[70]   D Andrae, U Häußermann, M Dolg, H Stoll, H Preuß, *Theoretica chimica acta* **1990**, *77*, 123–141.

[71]   K. Eichkorn, O. Treutler, H. Öhm, M. Häser, R. Ahlrichs, *Chemical physics letters* **1995**, *240*, 283–290.

[72]   K. Eichkorn, F. Weigend, O. Treutler, R. Ahlrichs, *Theoretical Chemistry Accounts* **1997**, *97*, 119–124.

[73]   B. Metz, H. Stoll, M. Dolg, *The Journal of Chemical Physics* **2000**, *113*, 2563–2569.

[74]   M. K. Armbruster, F. Weigend, C. van Wüllen, W. Klopper, *Physical Chemistry Chemical Physics* **2008**, *10*, 1748–1756.

[75]   F. Weigend, A. Baldes, *The Journal of chemical physics* **2010**, *133*, 174102.

[76]   D. Figgen, K. A. Peterson, M. Dolg, H. Stoll, *The Journal of chemical physics* **2009**, *130*, 164108.

[77]   H. Eshuis, J. E. Bates, F. Furche, *Theoretical Chemistry Accounts* **2012**, *131*, 1084.

[78] S. Grimme, S. Ehrlich, L. Goerigk, *Journal of computational chemistry* **2011**, *32*, 1456–1465.

[79] S. Grimme, J. Antony, S. Ehrlich, H. Krieg, *The Journal of chemical physics* **2010**, *132*, 154104.

[80] W. Kabsch, *Acta Crystallographica Section A: Crystal Physics Diffraction Theoretical and General Crystallography* **1976**, *32*, 922–923.

[81] A. H. Larsen, J. J. Mortensen, J. Blomqvist, I. E. Castelli, R. Christensen, M. Dułak, J. Friis, M. N. Groves, B. Hammer, C. Hargus, E. Hermes, *Journal of Physics: Condensed Matter* **2017**, *29*, 273002.

[82] J. Ho, M. L. Polak, K. M. Ervin, W. Lineberger, *The Journal of chemical physics* **1993**, *99*, 8542–8551.

[83] D.-K. Lee, G.-H. Jeung, Y. S. Lee, *International Journal of Quantum Chemistry* **2009**, *109*, 1975–1983.

[84] S. Yanagisawa, T. Tsuneda, K. Hirao, *Journal of Computational Chemistry* **2001**, *22*, 1995–2009.

[85] S. K. Gupta, B. M. Nappi, K. A. Gingerich, *Inorganic Chemistry* **1981**, *20*, 966–969.

[86] S. Taylor, G. W. Lemire, Y. M. Hamrick, Z. Fu, M. D. Morse, *The Journal of chemical physics* **1988**, *89*, 5517–5523.

[87] A Fortunelli, *Journal of Molecular Structure: THEOCHEM* **1999**, *493*, 233–240.

[88] H. J. Monkhorst, J. D. Pack, *Physical review B* **1976**, *13*, 5188.

[89] K. Hermann, *Crystallography and Surface Structure: An Introduction for Surface Scientists and Nanoscientists*, John Wiley & Sons, **2017**.

[90] N. Drebov, F. Weigend, R. Ahlrichs, *The Journal of chemical physics* **2011**, *135*, 044314.

[91] A. Sebetci, *Physical Chemistry Chemical Physics* **2009**, *11*, 921–925.

[92] M. J. Piotrowski, P. Piquini, J. L. Da Silva, *Physical Review B* **2010**, *81*, 155446.

[93] C. Kittel, *Introduction to solid state physics*, Wiley New York, **2004**.

[94] C. T. Campbell, *ACS Catalysis* **2017**, *7*, 2770–2779.

[95] A. J. Medford, A. Vojvodic, J. S. Hummelshøj, J. Voss, F. Abild-Pedersen, F. Studt, T. Bligaard, A. Nilsson, J. K. Nørskov, *Journal of catalysis* **2015**, *328*, 36–42.

[96] P. Sabatier, *La catalyse en chimie organique*, Nouveau Monde éditions, **2014**.

[97] M. Che, *Catalysis today* **2013**, *218*, 162–171.

[98] C.-J. Jia, F. Schüth, *Physical Chemistry Chemical Physics* **2011**, *13*, 2457–2487.

[99] M. Gajdoš, A. Eichler, J. Hafner, *Journal of Physics: Condensed Matter* **2004**, *16*, 1141.

[100] F. M. Hoffmann, *Surface Science Reports* **1983**, *3*, 107–192.

[101] S. K. Cheah, V. P. Bernardet, A. A. Franco, O. Lemaire, P. Gelin, *The Journal of Physical Chemistry C* **2013**, *117*, 22756–22767.

[102] S. G. Podkolzin, J. Shen, J. J. de Pablo, J. A. Dumesic, *The Journal of Physical Chemistry B* **2000**, *104*, 4169–4180.

[103] C. Lentz, S. P. Jand, J. Melke, C. Roth, P. Kaghazchi, *Journal of Molecular Catalysis A: Chemical* **2017**, *426*, 1–9.

[104] J. Szanyi, W. K. Kuhn, D. W. Goodman, *Journal of Vacuum Science & Technology A: Vacuum Surfaces and Films* **1993**, *11*, 1969–1974.

[105] M. Kappers, J. Van der Maas, *Catalysis letters* **1991**, *10*, 365–373.

[106] R. K. Brandt, M. Hughes, L. Bourget, K Truszkowska, R. G. Greenler, *Surface science* **1993**, *286*, 15–25.

[107] F. Maillard, E. R. Savinova, P. A. Simonov, V. I. Zaikovskii, U. Stimming, *The Journal of Physical Chemistry B* **2004**, *108*, 17893–17904.

[108] G. Blyholder, *The Journal of Physical Chemistry* **1964**, *68*, 2772–2777.

[109] P. S. Bagus, C. J. Nelin, C. W. Bauschlicher Jr, *Physical Review B* **1983**, *28*, 5423.

[110] B. Hammer, J. K. Nørskov in *Advances in catalysis, Vol. 45*, Elsevier, **2000**, pp. 71–129.

[111] P. J. Feibelman, B. Hammer, J. K. Nørskov, F Wagner, M. Scheffler, R. Stumpf, R Watwe, J Dumesic, *The Journal of Physical Chemistry B* **2001**, *105*, 4018–4025.

[112] A. Stroppa, G. Kresse, *New Journal of Physics* **2008**, *10*, 063020.

[113] F Abild-Pedersen, M. Andersson, *Surface Science* **2007**, *601*, 1747–1753.

[114] J. Zhao, M.-C. He, X.-X. Hu, W. Gao, *Chinese Physics B* **2017**, *26*, 079101.

[115] F Illas, S Zurita, A. Marquez, J Rubio, *Surface science* **1997**, *376*, 279–296.

[116] H. Aizawa, S. Tsuneyuki, *Surface science* **1998**, *399*, L364–L370.

[117] A Föhlisch, M Nyberg, J Hasselström, O Karis, L. Pettersson, A Nilsson, *Physical review letters* **2000**, *85*, 3309.

[118] A. Nilsson, L. G. M. Pettersson, *Surface Science Reports* **2004**, *55*, 49–167.

[119] A. Nilsson, M Weinelt, T. Wiell, P. Bennich, O Karis, N. Wassdahl, J Stöhr, M. G. Samant, *Physical review letters* **1997**, *78*, 2847.

[120] A. Nilsson, L. G. Pettersson, J. Norskov, *Chemical bonding at surfaces and interfaces*, Elsevier, **2011**.

[121] A Föhlisch, M Nyberg, P Bennich, L Triguero, J Hasselström, O Karis, L. Pettersson, A Nilsson, *The Journal of Chemical Physics* **2000**, *112*, 1946–1958.

[122] L Schimka, J Harl, A Stroppa, A Grüneis, M Marsman, F Mittendorfer, G Kresse, *Nature materials* **2010**, *9*, 741.

[123] S. E. Mason, I. Grinberg, A. M. Rappe, *Physical Review B* **2004**, *69*, 161401.

[124] G Kresse, A Gil, P. Sautet, *Physical Review B* **2003**, *68*, 073401.

[125] L. Verga, A. Russell, C.-K. Skylaris, *Physical Chemistry Chemical Physics* **2018**, *20*, 25918–25930.

[126] J. B. Davis, F. Baletto, R. L. Johnston, *The Journal of Physical Chemistry A* **2015**, *119*, 9703–9709.

[127] T Engel, G Ertl in *Advances in Catalysis*, *Vol. 28*, Elsevier, **1979**, pp. 1–78.

[128] H. Falsig, B. Hvolbæk, I. S. Kristensen, T. Jiang, T. Bligaard, C. H. Christensen, J. K. Nørskov, *Angewandte Chemie International Edition* **2008**, *47*, 4835–4839.

[129] M. M. Montemore, M. A. van Spronsen, R. J. Madix, C. M. Friend, *Chemical reviews* **2017**, *118*, 2816–2862.

[130] P. C. Jennings, H. A. Aleksandrov, K. M. Neyman, R. L. Johnston, *Nanoscale* **2014**, *6*, 1153–1165.

[131] Y. Okamoto, O. Sugino, *The Journal of Physical Chemistry C* **2010**, *114*, 4473–4478.

[132] H Steininger, S Lehwald, H Ibach, *Surface Science* **1982**, *123*, 1–17.

[133] C. Herring, *Physical review* **1951**, *82*, 87.

[134] T. Mori, T. Hegmann, *Journal of Nanoparticle Research* **2016**, *18*, 295.

[135] A. Ruditskiy, S.-I. Choi, H.-C. Peng, Y. Xia, *Mrs Bulletin* **2014**, *39*, 727–737.

[136] S. P. Ong, W. D. Richards, A. Jain, G. Hautier, M. Kocher, S. Cholia, D. Gunter, V. L. Chevrier, K. A. Persson, G. Ceder, *Computational Materials Science* **2013**, *68*, 314–319.

[137] L. G. Verga, J. Aarons, M Sarwar, D Thompsett, A. E. Russell, C.-K. Skylaris, *Faraday discussions* **2018**, *208*, 497–522.

[138] F. Calle-Vallejo, J. Tymoczko, V. Colic, Q. H. Vu, M. D. Pohl, K. Morgenstern, D. Loffreda, P. Sautet, W. Schuhmann, A. S. Bandarenka, *Science* **2015**, *350*, 185–189.

[139] J. K. Nørskov, T. Bligaard, J. Rossmeisl, C. H. Christensen, *Nature chemistry* **2009**, *1*, 37.

[140] Y. Jiao, Y. Zheng, M. Jaroniec, S. Z. Qiao, *Chemical Society Reviews* **2015**, *44*, 2060–2086.

[141] X. Wang, G. Zhang, L. Yang, E. Sharman, J. Jiang, *Wiley Interdisciplinary Reviews: Computational Molecular Science* **2018**, *8*, e1369.

[142] T. H. Yu, T. Hofmann, Y. Sha, B. V. Merinov, D. J. Myers, C. Heske, W. A. Goddard III, *The Journal of Physical Chemistry C* **2013**, *117*, 26598–26607.

[143] F. Abild-Pedersen, A. Nilsson, J. K. Nørskov, *The Journal of Physical Chemistry C* **2013**, *117*, 6914–6915.

[144] F. Calle-Vallejo, J. I. Martínez, J. M. García-Lastra, P. Sautet, D. Loffreda, *Angewandte Chemie International Edition* **2014**, *53*, 8316–8319.

[145] Z. Zhao, Z. Chen, X. Zhang, G. Lu, *The Journal of Physical Chemistry C* **2016**, *120*, 28125–28130.

[146] R. Jinnouchi, R. Asahi, *The journal of physical chemistry letters* **2017**, *8*, 4279–4283.

[147] G. Kresse, J. Furthmüller, *Physical review B* **1996**, *54*, 11169.

[148] G. Kresse, J. Furthmüller, *Computational materials science* **1996**, *6*, 15–50.

[149] G. Kresse, D Joubert, *Physical Review B* **1999**, *59*, 1758.

[150] M. Methfessel, A. Paxton, *Physical Review B* **1989**, *40*, 3616.

[151] M. O. Available: www.mongodb.com, [**accessed 10 September 2019**].

[152] J. Hill, G. Mulholland, K. Persson, R. Seshadri, C. Wolverton, B. Meredig, *Mrs Bulletin* **2016**, *41*, 399–409.

[153] M. official manual. Available: https://docs.mongodb.com/manual/. [**accessed 10 September 2019**].

[154] A. Jain, S. P. Ong, W. Chen, B. Medasani, X. Qu, M. Kocher, M. Brafman, G. Petretto, G.-M. Rignanese, G. Hautier, D Gunter, *Concurrency and Computation: Practice and Experience* **2015**, *27*, 5037–5059.

[155] A. Jain, S. P. Ong, G. Hautier, W. Chen, W. D. Richards, S. Dacek, S. Cholia, D. Gunter, D. Skinner, G. Ceder, K. Persson, *Apl Materials* **2013**, *1*, 011002.

[156] F. Available, *https://materialsproject.github.io/fireworks/* [**accessed 10 September 2019**].

[157] L. G. M. Pettersson, A. Nilsson, *Topics in catalysis* **2014**, *57*, 2–13.

[158] H. Over, *Progress in surface science* **1998**, *58*, 249–376.

[159] J. Wellendorff, T. L. Silbaugh, D. Garcia-Pintos, J. K. Nørskov, T. Bligaard, F. Studt, C. T. Campbell, *Surface Science* **2015**, *640*, 36–44.

[160] A. Bradshaw, F. Hoffmann, *Surface Science* **1978**, *72*, 513–535.

[161] N. Lopez, J. K. Nørskov, *Surface science* **2001**, *477*, 59–75.

[162] S. S. Laletina, M. Mamatkulov, E. A. Shor, V. V. Kaichev, A. Genest, I. V. Yudanov, N. Rosch, *The Journal of Physical Chemistry C* **2017**, *121*, 17371–17377.

[163] Y. Yeo, L Vattuone, D. King, *The Journal of chemical physics* **1997**, *106*, 392–401.

[164] R Imbihl, J. Demuth, *Surface science* **1986**, *173*, 395–410.

[165] U Starke, N Materer, A Barbieri, R Döll, K Heinz, M. Van Hove, G. A. Somorjai, *Surface science* **1993**, *287*, 432–437.

[166] M. Rose, A Borg, J. Dunphy, T Mitsui, D. Ogletree, M Salmeron, *Surface science* **2004**, *561*, 69–78.

[167] B. Han, C. Miranda, G Ceder, *Physical Review B* **2008**, *77*, 075410.

[168] P Gambardella, Ž Šljivančanin, B Hammer, M Blanc, K Kuhnke, K Kern, *Physical review letters* **2001**, *87*, 056103.

[169] Z. Gu, P. B. Balbuena, *The Journal of Physical Chemistry C* **2007**, *111*, 9877–9883.

[170] M. Todorova, K. Reuter, M. Scheffler, *The Journal of Physical Chemistry B* **2004**, *108*, 14477–14483.

[171] L. Li, A. H. Larsen, N. A. Romero, V. A. Morozov, C. Glinsvad, F. Abild-Pedersen, J. Greeley, K. W. Jacobsen, J. K. Nørskov, *The journal of physical chemistry letters* **2012**, *4*, 222–226.

[172] J. Kleis, J Greeley, N. Romero, V. Morozov, H. Falsig, A. H. Larsen, J. Lu, J. J. Mortensen, M Dułak, K. S. Thygesen, J. Nørskov, *Catalysis Letters* **2011**, *141*, 1067–1071.

[173] F. J. Vidal-Iglesias, R. M. Arán-Ais, J. Solla-Gullón, E. Herrero, J. M. Feliu, *ACS Catalysis* **2012**, *2*, 901–910.

[174] Y. Xiong, B. J. Wiley, Y. Xia, *Angewandte Chemie International Edition* **2007**, *46*, 7157–7159.

[175] G. A. Somorjai, D. Blakely, *Nature* **1975**, *258*, 580.

[176] G. Peng, M. Mavrikakis, *Nano letters* **2014**, *15*, 629–634.

[177] A. Boubnov, A. Gänzler, S. Conrad, M. Casapu, J.-D. Grunwaldt, *Topics in Catalysis* **2013**, *56*, 333–338.

[178] J. Singh, M. Nachtegaal, E. M. Alayon, J. Stötzel, J. A. van Bokhoven, *ChemCatChem* **2010**, *2*, 653–657.

[179] S. D. Miller, N. İnoğlu, J. R. Kitchin, *The Journal of chemical physics* **2011**, *134*, 104709.

[180] J. R. Kitchin, *Physical Review B* **2009**, *79*, 205412.

[181] A. Soon, M. Todorova, B. Delley, C. Stampfl, *Physical Review B* **2006**, *73*, 165424.

[182] J. Rogal, K. Reuter, Ab initio atomistic thermodynamics for surfaces: A primer, tech. rep., MAX-PLANCK-GESELLSCHAFT ZUR FOERDERUNG DER WISSENSCHAFTEN EV BERLIN (GERMANY , **2006**.

[183] A. Farkas, D. Fantauzzi, J. E. Mueller, T. Zhu, C. Papp, H.-P. Steinrück, T. Jacob, *Journal of Electron Spectroscopy and Related Phenomena* **2017**, *221*, 44–57.

[184] P. Linstrom, W. Mallard, NIST Chemistry WebBook, NIST Standard Reference Database Number 69, National Institute of Standards and Technology, Gaithersburg MD, 20899, https://doi.org/10.18434/T4D303, (retrieved August 11, 2019). **2019**.

[185] G. Rupprechter, T. Dellwig, H. Unterhalt, H.-J. Freund, *Topics in Catalysis* **2001**, *15*, 19–26.

[186] T. Ogawa, A. Kuwabara, C. A. Fisher, H. Moriwake, T. Miwa, *The Journal of Physical Chemistry C* **2013**, *117*, 9772–9778.

[187] A. Bogicevic, J. Strömquist, B. I. Lundqvist, *Physical Review B* **1998**, *57*, R4289.

[188] M. P. Johansson, A. Lechtken, D. Schooss, M. M. Kappes, F. Furche, *Physical Review A* **2008**, *77*, 053202.

Appendix A

Structure–Properties Database

This appendix correspond to the database description give in chapter 7, section 7.3.

The following script is based on MongoDb built-in features that can help to query a data from the "nanopads-spd-prod" database.

Step 1: Importing libraries and functions

```
import yaml, json
from pymongo import MongoClient
from bson.dbref import DBRef
import pprint
```

Step 2: Connect to "nanopads-spd-prod" database.

```
with open('nanopads_spd_prod.yaml', 'r') as params:
    mongoclient_params = yaml.load(params)


client = MongoClient(**mongoclient_params)
db = client['nanopads-spd-prod']
```

Step 3: Connect to collections that are in the "nanopads-spd-prod" database.

```
structs = db.structures
params = db.parameters
props = db.properties
```

Step 4: Query a particular document from properties collection using the metadata; size, site and GCN and print out it.

```
pprint.pprint(list(props.find({"Pt.size":38, "Pt.site":"ontop","Pt.GCN"
    :4.0})))
```

This gives the following output that includes post process results and reference links to the corresponding structures and parameters.

```
[{'Pt': {'GCN': 4.0, 'adsorbate': 'CO', 'site': 'ontop', 'size': 38},
  '_id': ObjectId('5d7032c5757ec1431873ce22'),
  'result_properties_complex': {'energy': -205.81105325,
                                'fermi': -4.8235,
                                'forces': [[-0.002977, -0.014293, 0.0],
```

```
                                      [0.000436, 0.004958, 0.014755],
                                      [0.000436, 0.004958, -0.014755],
                                      [0.006793, 0.005071, 0.0],
                                      [0.007503, 0.002588, 0.0],
                                      [0.013628, 0.008556, 0.013353],
                                      [0.013628, 0.008556, -0.013353],
                                      [0.013964, 0.008538, 0.009847],
                                      [-0.000487, -0.002751, 0.02333],
                                      [-0.000537, -0.01454, -0.00719],
                                      [0.025072, 0.034508, 0.0],
                                      [0.013705, -0.047297, 0.0],
                                      [7.8e-05, -0.00194, -0.013738],
                                      [-0.000537, -0.01454, 0.007196],
                                      [0.013964, 0.008538, -0.009847],
                                      [-0.00048, -0.00275, -0.02333],
                                      [7.8e-05, -0.00194, 0.013738],
                                      [-0.021019, -0.010826, 0.007521],
                                      [0.009397, 0.015729, 0.002225],
                                      [0.00777, 0.004797, 0.0],
                                      [-0.020939, -0.009111, 0.0],
                                      [-0.003464, -0.002381, 0.003339],
                                      [0.009397, 0.015729, -0.002225],
                                      [-0.021019, -0.010826, -0.00752],
                                      [-0.003464, -0.002381, -0.00333],
                                      [-0.01216, 0.021176, 0.0],
                                      [-0.011164, -0.01384, -0.00038],
                                      [-0.020313, -0.016304, -0.0123],
                                      [0.007339, -0.017225, 0.0],
                                      [-0.027265, 0.005285, 0.0],
                                      [-0.005067, 0.007308, 0.003141],
                                      [-0.020313, -0.016304, 0.012398],
                                      [-0.011164, -0.01384, 0.000388],
                                      [-0.005067, 0.007308, -0.003141],
                                      [-0.000653, 0.007105, -0.009654],
                                      [0.016061, 0.008004, 0.0],
                                      [-0.006933, -0.046417, 0.0],
                                      [-0.000653, 0.007105, 0.009654],
                                      [0.021868, 0.038113, 0.0],
                                      [0.014562, 0.035576, 0.0]],
                          'k-point weights': [1.0],
                          'number of bands': 280,
                          'spin polarized': True,
                          'vibrational_frequencies':[[258.165523,
                                                      59.947022,
                                                      50.344886,
                                                      47.685162,
                                                      7.80207,
                                                      2.58893]]},
    'parameters': DBRef('parameters', ObjectId('5d7032c5757ec1431873ce20')),
```

```
    'structures': DBRef('structures', ObjectId('5d7032c5757ec1431873ce21')),
    'post process results': {'adsorption energy (eV)': -2.2375210299999804,
                              'd-band center': -2.0407130242495928,
                              'vibrational frequencies(meV)': [[258.165523,
                                                                59.947022,
                                                                50.344886,
                                                                47.685162,
                                                                7.80207,
                                                                2.58893],
                                                              ]}}]
```

Listing A.1: An example of properties query result for CO adsorbed on Pt$_{38}$ at on-top site (GCN 4).

Step 5: Query a particular document from parameters collection using the metadata; size, site and GCN and print out it.

```
pprint.pprint(list(params.find({"Pt.size":38, "Pt.site":"ontop","Pt.GCN"
   :4.0})))
```

This gives the following parameters output for the geometry optimization and vibrational mode calculation.

```
[{'Pt': {'GCN': 4.0, 'adsorbate': 'CO', 'site': 'ontop', 'size': 38},
  '_id': ObjectId('5d7032c5757ec1431873ce20'),
'parameters_complex':
      {'calculator': {'name': 'vasp',
                      'parameters': {'algo': 'Fast',
                                     'ediff': 1e-05,
                                     'ediffg': -0.05,
                                     'encut': 450.0,
                                     'gga': 'PE',
                                     'ibrion': 2,
                                     'ispin': 2,
                                     'kpts': [1, 1, 1],
                                     'lcharg': False,
                                     'lreal': False,
                                     'lwave': False,
                                     'nbands': 280,
                                     'nsw': 100,
                                     'pp': 'PBE'}}},
'vibratinal_frequencies_parameters':
      {'calculator': {'name': 'vasp',
                      'parameters': {'algo': 'Fast',
                                     'ediff': 1e-07,
                                     'ediffg': -0.05,
                                     'encut': 450.0,
                                     'gamma': False,
                                     'gga': 'PE',
                                     'ibrion': 7,
```

```
                                        'kpts': [1, 1, 1],
                                        'lcharg': False,
                                        'lreal': False,
                                        'lwave': False,
                                        'nbands': 240,
                                        'nsw': 1,
                                        'pp': 'PBE'}}}}]
```

Listing A.2: An example of parameters query for CO adsorbed on Pt_{38} at on-top site (GCN 4).

Step 6: Query a particular document from structures collection using the metadata; size, site and GCN and print out it.

```
pprint.pprint(list(structs.find({"Pt.size":38, "Pt.site":"ontop","Pt.GCN"
    :4.0})))
```

This gives the following structures output for the geometry optimization.

```
[{'Pt': {'GCN': 4.0, 'adsorbate': 'CO', 'site': 'ontop', 'size': 38},
'_id': ObjectId('5d7032c5757ec1431873ce21'),
'optimized_structure_complex':
   {'cell': [[27.065523210000002,0.0,0.0],[0.0, 23.84, 0.0],[0.0, 0.0,
   23.84]],
    'numbers':
  [78,78,78,78,78,78,78,78,78,78,78,78,78,78,78,78,78,78,78,78,
                78,78,78,78,78,78,78,78,78,78,78,78,78,78,78,78,78,6,8],
    'pbc': [True, True, True],
    'positions': [[8.137227625116859,9.998603676139844,11.92],
                 [8.156922727702563,11.907376858769297,10.04625566735684],
                 [8.156922727702563,11.907376858769297,13.79374433264315],
                 [8.148440516944497,13.830619797578068,11.92],
                 [9.980003451001275,8.124119713902674,11.92],
                 [11.924574679299598,8.162488001399568,10.03212080883382],
                 [11.924574679299598,8.162488001399568,13.80787919116614],
                 [10.022328694830104,11.91816645390508,8.194697049085654],
                 [11.936776289054421,10.039712682418186,8.18827353902718],
                 [9.82003356658736,9.805916211179142,9.830688410892977],
                 [10.037475722991749,11.905675553362325,11.92],
                 [11.912350327052055,10.037228930981883,11.92],
                 [11.939358259329495,11.928718493405624,10.0714280744365],
                 [9.82003356658736,9.805916211179142,14.009311589107023],
                 [10.022328694830104,11.91816645390508,15.64530295091434],
                 [11.936776289054421,10.039712682418186,15.6517264609728],
                 [11.939358259329495,11.928718493405624,13.7685719255631],
                 [11.903000390259757,13.823042925074647,8.18472597285873],
                 [9.803665185152605,14.029015517403385,9.8313634767671],
                 [9.997693275308167,15.709247664788672,11.92],
                 [11.9181538798338,13.805564716291002,11.92],
                 [11.959179860516718,15.6634049904722,10.068832804721893],
                 [9.803665185152605,14.029015517403385,14.00863652323289],
```

```
                      [11.903000390259757 ,13.823042925074647 ,15.6552740271414] ,
                      [11.959179860516718 ,15.6634049904722 ,13.771167195278112] ,
                      [13.815496893114263 ,8.16108218825017 ,11.92] ,
                      [13.816669204376268 ,11.956388006785602 ,8.16150467897768] ,
                      [14.036432266963022 ,9.847278937096144 ,9.841396610124507] ,
                      [13.858752582027575 ,11.992768919967963 ,11.92] ,
                      [15.691090688840879 ,10.008796594020884 ,11.92] ,
                      [15.703678608093915 ,11.904650273023131 ,9.99206701978317] ,
                      [14.036432266963022 ,9.847278937096144 ,13.99860338987549] ,
                      [13.816669204376268 ,11.956388006785602 ,15.6784953210223] ,
                      [15.703678608093915 ,11.904650273023131 ,13.8479329802168] ,
                      [14.052309611152833 ,14.025033124594483 ,9.84203659656432] ,
                      [13.919389873188452 ,15.674664976087548 ,11.92] ,
                      [15.900275929001104 ,13.799916976707953 ,11.92] ,
                      [14.052309611152833 ,14.025033124594483 ,13.9979634034356] ,
                      [17.600558961503445 ,14.483028728358736 ,11.92] ,
                      [18.696121397438645 ,14.87392654250935 ,11.92]]}}]
```

Listing A.3: An example of structures query for CO adsorbed on Pt$_{38}$ at on-top site (GCN 4).

Step 7: Find the parameters document employed to produce a given properties using the linked parameters id.

```
calc = db.dereference(props.find_one({"Pt.size":38, ''adsorbate'': ''CO'', "
   Pt.site":"ontop","Pt.GCN":4.0})['parameters'])
for k in calc:
    if isinstance(calc[k], DBRef):
        calc[k] = db.dereference(calc[k])
pprint.pprint(calc)
```

This will print out the calculator parameters that have been used to produce the results for the specific calculation.

Step 8: Find a structure that have 38 platinum atoms and CO adsorbate at on-top site with GCN 4 that linked to properties collection.

```
calc = db.dereference(props.find_one({"Pt.size":38, ''adsorbate'': ''CO'', "
   Pt.site":"ontop","Pt.GCN":4.0})['structures'])
for k in calc:
    if isinstance(calc[k], DBRef):
        calc[k] = db.dereference(calc[k])
pprint.pprint(calc)
```

This will print out the calculated structure that have 38 platinum atoms and CO adsorbate at on-top site with GCN 4.

Acknowledgments